Modelling and Control of an Autonomous Underground Mine Vehicle

by

Bruce James Dragt

Submitted in partial fulfillment of the requirements for the degree

Master of Engineering (Electronic Engineering)

in the

Faculty of Engineering, the Built Environment and

Information Technology

UNIVERSITY OF PRETORIA

January 2006

Summary

Title:	Modelling and Control of an Autonomous Underground Mine Vehicle
By:	Bruce James Dragt
Supervisor:	Professor I.K. Craig
Co-supervisor:	Professor F.R. Camisani-Calzolari
Department:	Department of Electrical, Electronic and Computer Engineering
Degree:	Master of Engineering(Electronic Engineering)

The mining industry is constantly under pressure to improve productivity, efficiency and safety. Although an increased use of automation technology has the potential of contributing to improvements in all three factors mines have been relatively slow to make use of automation technology. Automation in the underground mining environment is a challenging prospect for a number of reasons not least of which being the difficulties and associated costs of installing infrastructure in this hazardous environment. The work described in this dissertation focuses on the modelling of a Load-Haul-Dump or LHD vehicle for the purpose of autonomous navigation and control.

Considerable progress has been made in automating underground mining vehicles in recent years, and successful test installations have been made. There are still however a number of shortcomings in the existing autonomous underground mine vehicle navigation systems. This dissertation attempts to address some of these problems through the development of a more accurate vehicle model for an LHD vehicle incorporating some vehicle and tyre dynamics thereby potentially reducing the number of sensors and the amount of installed infrastructure necessary to implement the vehicle navigation system. Simulation results are provided for different vehicle modelling techniques and the results are compared and discussed in terms of their suitability for physical implementation in an underground mine.

Keywords: Modelling, kinematics, dynamics,estimation, Kalman filter, navigation, teleoperation, underground mine vehicles, LHD.

Opsomming

Titel:	Modellering en Beheer van 'n Automatiese Ondergrondse Myn Voertuig
Deur:	Bruce James Dragt
Studieleier:	Professor I.K. Craig
Medestudieleier:	Professor F.R. Camisani-Calzolari
Departement:	Department Elektriese, Elektroniese en Rekenaar Ingenieurswese
Graad:	Magister in Ingenieurwese(Elektroniese Ingenieurwese)

Die mynbedryf is onder konstante druk om produktiwiteit, rendiment en veiligheid te verbeter. Alhoewel die groter gebruik van automatisasie tegnologie die potensiaal het om tot die drie faktore by te dra is myne relatief stadig om die tegnologie toegepas. Automatisasie in die ondergrondse myn omgewing is vir 'n aantal redes 'n uitdagende oefening waarvan nie minste die moeilikhede en meegaande kostes van infrastuktuur in die gevaarlike omgewing is. Die werk wat in hierdie verhandeling beskryf word, fokus op die modellering van 'n Laai-vervoer-dompel voertuig met die doel op automatiese navigasie en beheer.

Aansienlike vooruitgang is in die afgelope jare in die automatiesering van ondergrondse myn voertuie gemaak en suksesvolle installasies is gebou. Daar is nie teenstande nog 'n aantal tekortkominge in die bestaande automatiese ondergrondse myn voertuig stelsels. Hierdie verhandling poog om sommige van hierdie probleme aan te spreek deur 'n meer akkurate voertuig model te ontwikkel wat sommige voertuig en band dinamika insluit om moontlik daardeur die aantal sensors en die hoeveelheid geinstalleerde infrastruktuur nodig om die voertuig navigasie stelsel te implementeer te verminder. Simulasie resultate word voorsien vir verskillende voertuig modellering tegnieke en die resultate word vergelyk en bespreek in terme van hulle toepaslikheid vir fisiese implementeering in 'n ondergrondse myn.

Sleutelterme: Modellering, kinematika, dinamika,beraming, Kalman filter, navigasie, afstand beheer, ondergrondse myn voertuie, LHD.

Acknowledgments

I would like to express my sincere gratitude and thanks to my study leaders Professor I.K. Craig and Professor F.R. Camisani-Calzolari for their support and guidance with this study.
Special thanks are due to De Beers Consolidated Mines, and specifically Dr Gunter Metzner, for their contribution to this research project.
Finally I would also like to thank my friends and family for their sustained support and encouragement.

Contents

1 Introduction **1**
1.1 Motivation . . . 1
1.2 Background . . . 3
1.2.1 Safety . . . 3
1.3 Contribution . . . 5
1.4 Dissertation approach . . . 5
1.5 Organisation . . . 6

2 Process Overview **7**
2.1 Underground Trackless Mining Process . . . 7
2.2 Trackless Mining Vehicles . . . 10
2.2.1 LHD Vehicles . . . 11
2.2.2 Trucks . . . 13
2.3 Chapter Summary . . . 14

3 Navigation of a Mobile Robot **16**
3.1 Introduction . . . 16
3.2 Robotic Environment . . . 16
3.3 Navigation Techniques . . . 17
3.3.1 Dead Reckoning . . . 17
3.3.1.1 Odometry . . . 18
3.3.2 Inertial Navigation . . . 19
3.3.3 Data Fusion Methods . . . 19
3.3.3.1 Artificial Beacons . . . 20
3.3.3.2 Natural Beacons and Map Based Recognition . . . 21
3.4 Path Tracking Control . . . 22
3.5 Advanced Navigation Algorithms . . . 23
3.6 Navigation of LHD vehicles . . . 24
3.6.1 Absolute Navigation . . . 24
3.6.2 Reactive Navigation . . . 27
3.6.2.1 Potential Field Methods . . . 27
3.6.2.2 Neural Network Methods . . . 28
3.6.3 Path Planning and Decision Making . . . 28
3.7 Safety . . . 28
3.7.1 Obstacle Detection and Collision Avoidance . . . 29
3.7.1.1 Sensors . . . 29
3.7.1.2 Fail Safety . . . 30
3.8 Chapter Summary . . . 31

4 Vehicle Modelling Background **32**
4.1 Fundamentals of Vehicle Modelling . . . 32
4.1.1 Lumped Mass . . . 32
4.1.2 Vehicle Axis System . . . 33
4.1.3 Dynamic Axle Loads . . . 33
4.2 Kinematic Modelling . . . 34
4.2.1 Low Speed Steering Models . . . 34
4.2.2 Tyre Forces and Moments . . . 36
4.2.2.1 Slip Angles . . . 36
4.2.2.2 Friction Circle Concept . . . 39
4.2.2.3 Friction Ellipse Concept . . . 39
4.2.2.4 Comprehensive Tyre Modelling Techniques . . . 40
4.2.2.5 Longitudinal Force Modelling . . . 43
4.2.2.6 Rolling Resistance . . . 44
4.2.3 Dynamic Vehicle Models . . . 44
4.2.3.1 Cornering Equations for a single track model . . . 46
4.2.3.2 Steering Gradient . . . 48
4.3 Chapter Summary . . . 49

5 Application of Vehicle Modelling Techniques to LHD Vehicles **50**
5.1 Kinematic Model . . . 50
5.2 Extended Kalman Filter Model . . . 51
5.2.1 Important Effects of Accounting for Slip . . . 52
5.2.2 The Error Model . . . 52
5.3 Single-track Vehicle Model . . . 53
5.3.1 Centre of Gravity Calculations for an LHD . . . 55
5.3.1.1 Understeer Gradient . . . 56
5.4 Complex Vehicle Model Derivation . . . 57
5.4.1 The Coordinate System . . . 57
5.4.2 Model Derivation . . . 59
5.4.3 Vehicle Kinematics . . . 59
5.4.3.1 Front Unit Kinematics . . . 59
5.4.3.2 Translational Velocity of Front Unit . . . 60
5.4.3.3 Rear Unit Kinematics . . . 61
5.4.3.4 Translational Velocity of Rear Unit . . . 61
5.4.4 Kinetic Energy . . . 61
5.4.5 Potential Energy . . . 62
5.4.6 Equations of Motion . . . 62
5.4.7 Generalised Forces . . . 64
5.4.8 Subsystems: Tyre and Suspension Model . . . 67
5.4.8.1 Tyre Model . . . 67
5.4.8.2 Suspension Model . . . 70
5.5 Chapter Summary . . . 70

6 Model Validation **71**
6.1 Tyre Parameter Validation . . . 71
6.1.1 Equipment used . . . 71
6.2 Vehicle Model Validation . . . 71
6.2.1 Equipment used . . . 72
6.2.1.1 Differential GPS . . . 72
6.2.1.2 VBOX System Overview . . . 72
6.2.2 Experiment Design . . . 73
6.2.2.1 Constant Radius Method . . . 73

6.2.2.2 Constant Speed Method 74
6.2.3 Model Tuning Parameters 74
6.3 Chapter Summary 74

7 Vehicle Model Simulations **76**
7.1 Kinematic Model Simulation 76
7.2 EKF Model Simulation 78
7.3 Single-Track Model Simulation 81
7.3.1 Unloaded LHD Vehicle Single-track Model 82
7.3.2 Loaded LHD Vehicle Single-track Model 83
7.3.3 Single-Track Model Simulation Discussion 83
7.4 Complex Vehicle Model Simulations 84
7.4.1 Control Strategy 84
7.4.2 Simulation Results 88
7.4.3 Complex Vehicle Model Discussion 96
7.5 Chapter Summary 99

8 Conclusion **100**
8.1 Summary 100
8.2 Conclusions 100
8.3 Future Work 101

References **102**

List of Figures **108**

List of Tables **111**

Chapter 1

Introduction

This chapter gives an outline of the motivation for this dissertation, the objectives and contribution to the modelling and control of an underground mine vehicle. The objectives give a clear definition of the focus of the dissertation; an overview of the dissertation organisation is also provided.

1.1 Motivation

Mining is an important global industry; however in today's economy it is essential that the mines remain as productive as possible in order to remain economically viable. In spite of this the mining industry has been slow too make use of robotics and automation technology [1]. Most of the productivity increases have been achieved through mechanisation making use of electrical and diesel powered machinery.

While the increased levels of mechanisation have led to improved productivity it has also lead to safety concerns. There is an increased risk of serious injury to humans caused by having to work in confined spaces with heavy machinery as well as the less dramatic long term injuries caused by inhalation of dust and exhaust fumes in poorly ventilated underground work tunnels or skeletal and soft tissue damage from machine vibration [2]. Many underground mining tasks are also repetitive and tedious [3]. One such task is performed by an LHD (Load, Haul and Dump) vehicle that is used for the transportation of ore from the underground voids known as stopes, (where the ore is fragmented by blasting), to an ore pass from where ore is transported by gravity to another handling point. The LHD and its operator move back and forth along a mine tunnel, which is typically a few hundred metres long, hauling the ore. The more repetitions of this cycle are completed within a shift the higher the production.

The stopes from which the LHD is required to collect the ore are hazardous due to the high rock stresses and the likelihood of rock-falls, making access undesirable to humans. For

this reason the LHD is presently operated remotely within the stopes, requiring the driver to alight from the vehicle every cycle, which increases the cycle time and the possibility of injury to the driver. In order to prevent this, some mines are now teleremotely operating the LHD vehicles for the entire cycle from above ground [4]. Figure 1.1 shows a teleoperator station at LKAB in Kiruna, Sweden. The teleoperator is located on the seventh floor of the LKAB office building while the vehicle is operating 750 meters underground.

Figure 1.1: LHD Tele-operator station at LKAB in Kiruna, Sweden.

While this has lead to improved safety, these systems unfortunately lead to a decrease in productivity. The sensory perception of the drivers operating the vehicles from above ground is decreased causing running speeds to be lower, resulting in lower production levels and the additional economic overhead of the infrastructure required for teleoperation.

For the above mentioned reasons several autonomously guided vehicle (AGV) systems have been tested in underground mines. Most of these systems have been based on AGV systems used in industrial environments and are optically guided by means of cameras that follow an optical guide made of a retro-reflective stripe or a light emitting rope in the tunnel roof [5]. A commercial high speed underground navigation system called Q-Navigator [6] is also available which makes use of retro-reflective tape mounted on holders on the tunnel walls and a rotating laser scanner. The angle of the rotating head of the scanner is recorded when the beam is reflected back into the scanner. The measured angles together with a map of the reflector positions are used to determine the position

and heading of the vehicle in order to navigate.
This approach has proven very effective in industrial manufacturing environments and has proven to work in the underground mine environment. Unfortunately due to the ever changing and unstructured environment of the mine tunnel, this approach is not desirable as a large amount of extra infrastructure is required to be installed [7].
As described by [7] the navigation system should ideally be entirely self-contained onboard the vehicle and require no extra infrastructure in the tunnel, and allow the LHD to drive at full speed so as not to loose productivity. It should also be simple and take a short period of time to take a new route or change an existing route. [7] also suggests, that teleoperation should be an integrated and seamless part of the navigation system.
These requirements are very challenging to meet as mines place a high demand on reliability in a harsh physical environment that is often hot, occasionally dusty and wet.

1.2 Background

Automation of LHDs has been studied for more than fifteen years [7]. The study has concentrated on automatic navigation in a tunnel, which is often referred to as guidance, which requires positioning of the vehicle to keep it on a reference trajectory. Automatic loading of the bucket has also been studied but this has proven very challenging and is beyond the scope of this dissertation.
There have been two main approaches in research on a navigation system for an LHD, namely absolute navigation, in which the position of the vehicle is referenced to some fixed real world co-ordinate system, and reactive navigation in which the LHD reacts to objects in its environment in order to continue moving forward.
There are four main tasks that need to be completed by an autonomous vehicle in some form or another in order to achieve successful autonomous navigation, namely sensing the environment, building its own representation of the environment, locating itself within the environment and finally planning and executing efficient routes in this environment [8]. These tasks are more significant in an underground mine for reasons of safety and efficiency.

1.2.1 Safety

Safety is a critical issue for all autonomous vehicles. The most significant issues as outlined in [2] are:

1. Safety to personnel. In an underground mine environment this is straightforward as access to the work area can be restricted by means of electronically guarded

access points. Should it be necessary for a worker to enter the operating area of the autonomously guided vehicle they can be fitted with active or passive tags to notify vehicles of their presence.

2. Vehicle obstacle. Detection is necessary as a last-resort mechanism to protect the vehicle from collision with other vehicles or personnel. However, the vehicle dispatching system and the personnel access control systems should normally avoid these situations. Obstacle detection is also necessary for preventing collisions with rock falls, broken down vehicles, or dangling overhead pipes.

3. Breakdown detection. A fail-safe method of determining a vehicle breakdown is required. In the event that a serious failure prevents the vehicle from communicating with the supervisory system the location of the vehicle may need to be inferred from its last reported position. A repair or recovery crew would then need to be dispatched and the other autonomously guided vehicles whose path is blocked by the broken down vehicle need to be rescheduled or rerouted. A severe failure, such as fire, should activate an onboard fire suppression system and communicate with the mine ventilation system.

From these safety requirements it is clear that the navigation systems of the autonomously guided vehicles are required to integrate with the mine management and vehicle dispatching systems. In order to implement such a system automation is only one component of a much larger system with the following fundamental requirements [4]:

- Automation
- Control systems
- Telecommunications
- Positioning
- Software
- Electronics
- Mining Engineering
- Organisation

1.3 Contribution

In an autonomous vehicle navigation system, information from sensors installed both onboard the vehicle and external to the vehicle, is combined to estimate the motion of the vehicle. The issue of sensing and the effects of sensor accuracy have been widely studied, [9], [10], there are however few results or insights of the complementary role played by the vehicle model available in literature,[11].

In an autonomous vehicle navigation system, the vehicle model together with the sensor model play equivalent roles in generating information and reducing the uncertainty in the estimation of the autonomous vehicle's location and heading (pose). Theoretically perfect sensing of all the vehicle states would eliminate the need for any predictive vehicle model. Alternatively a perfect vehicle model has no uncertainty in the vehicle's motion following a control input and would eliminate the need for sensing the vehicles state. Obviously neither case is practically feasible and there is therefore an inherent tradeoff between sensor suites and vehicle models, [11]. As one becomes more accurate the other can become less accurate while allowing the same level of navigation system performance to be maintained.

The main contribution of the dissertation is the development of a model that is able to accurately depict the location and heading of a specific LHD vehicle incorporating dynamic effects of the motion as well as the effects of loading of the vehicle. By improving the accuracy of the vehicle model it is hoped that in future the amount of sensors and installed infrastructure in the underground mining environment can be reduced while maintaining an acceptable level of navigation accuracy.

The vehicle model will also be applicable to agricultural and construction vehicles using the same articulated steering geometry as an LHD vehicle. A comparison of the various different modelling techniques used to model articulated steered vehicles is also provided.

1.4 Dissertation approach

The engineering problem addressed in this dissertation is the navigation of an autonomous underground mine vehicle, specifically a Load-Haul-Dumper or LHD vehicle, with the aim of thoroughly investigating possible solutions to this problem. The different methods of modelling the LHD vehicle will be evaluated qualitatively in terms of their ability to address a real world problem of complexity and cost of implementation and efficiency/productivity. The different LHD vehicle models are simulated to allow the feasibility and performance of the methods to be compared.

1.5 Organisation

Chapter 2 of this dissertation presents an introduction into the modern underground trackless mining environment and introduces vehicles which are used in this mining method and are therefore desirable to automate.
Chapter 3 of this dissertation presents an overview of autonomous vehicle guidance specifically from the perspective of the underground mining environment as well as related issues such as path planning, obstacle detection, etc.
Chapter 4 provides an introduction to the fundamentals of vehicle modelling.
Chapter 5 elaborates on the application of these modelling techniques of chapter 4 in terms of their application to an LHD vehicle. A brief overview of existing models is given in this chapter as well as a derivation of the models used in this dissertation.
Chapter 6 gives a brief description of the experiment design and data collection process that is required to be carried out in order to validate the vehicle model used in this dissertation.
In chapter 7 simulation results of the various vehicle models are shown. The simulations are performed using Matlab. The performance of the resulting models is evaluated with discussions of the merits and demerits of each.
Chapter 8 concludes with recommendations for future work and conclusions drawn from the work completed.

Chapter 2

Process Overview

The purpose of this chapter is to give a brief introduction into the modern underground trackless mining environment. A brief description of two mining methods which make use of trackless mining equipment is given. Descriptions of the underground trackless mining vehicles are given specifically for LHD vehicles and the tasks performed by the vehicles are discussed.

2.1 Underground Trackless Mining Process

Two mining methods which make use of trackless mining equipment are block caving and large-scale sub-level caving. Figure 2.1 provides an illustration of the block cave mining method. In a block cave mine tunnels are developed underneath the ore body and the ore is allowed to collapse under its own weight into funnel shaped chutes called drawpoints, [12]. LHD vehicles are then used to transport the ore from these drawpoints to the transfer points.
In figure 2.1 the ore is transferred to the main haulage which is carried out by a train travelling on tracks. In a trackless mine this task would be carried out by trucks.

Figure 2.2 shows the layout of a typical block cave mine. On the left of the figure is the complex network of tunnels which are located beneath the drawpoints. These are the tunnels in which the LHD's drive to collect the ore, and transport it to the transfer points labelled one to four. Trucks then transport the ore from the four transfer points along the tunnel loop on the right of the figure to the crusher bin.
An alternate mining method which makes use of LHD vehicles is that of large-scale sub-level caving, [13]. Figure 2.3 illustrates the steps involved in this mining method.
In the first step drifts or dead-end tunnels are constructed into the ore body. Production drilling where holes are drilled for explosives is then carried out on these tunnels in step

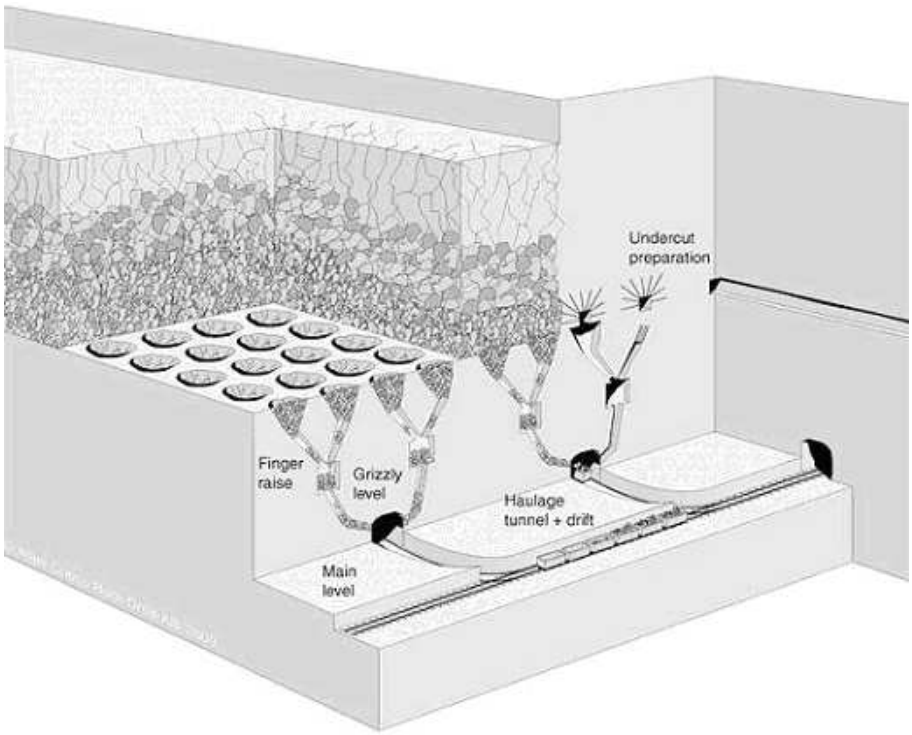

Figure 2.1: Illustration of the block cave mining method. The vehicles in this case move on tracks. However the principle is the same for trackless vehicles.[Figure Courtesy of De Beers Consolidated Mines]

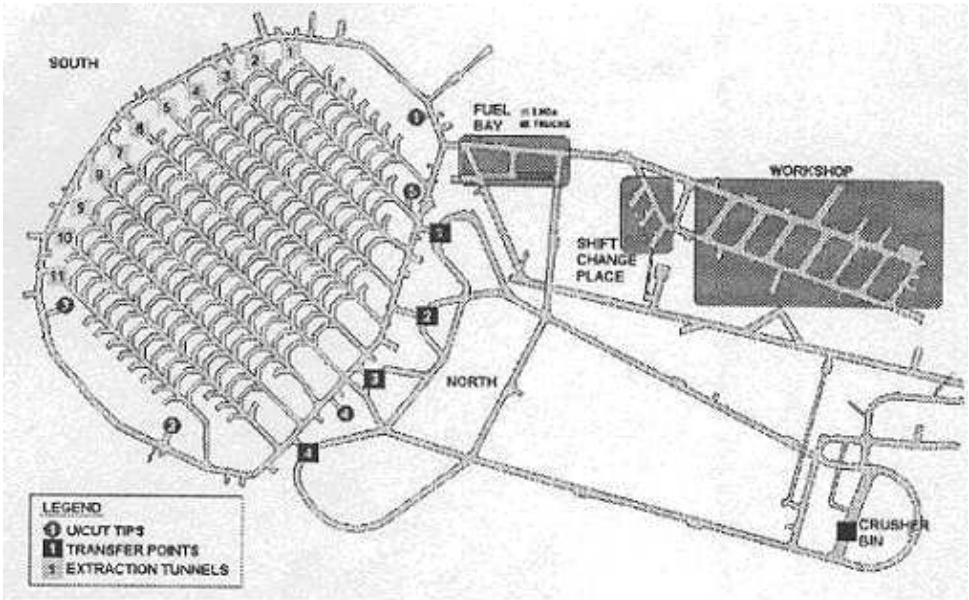

Figure 2.2: Layout of a typical trackless underground block cave mine, [Figure Courtesy of De Beers Consolidated Mines]

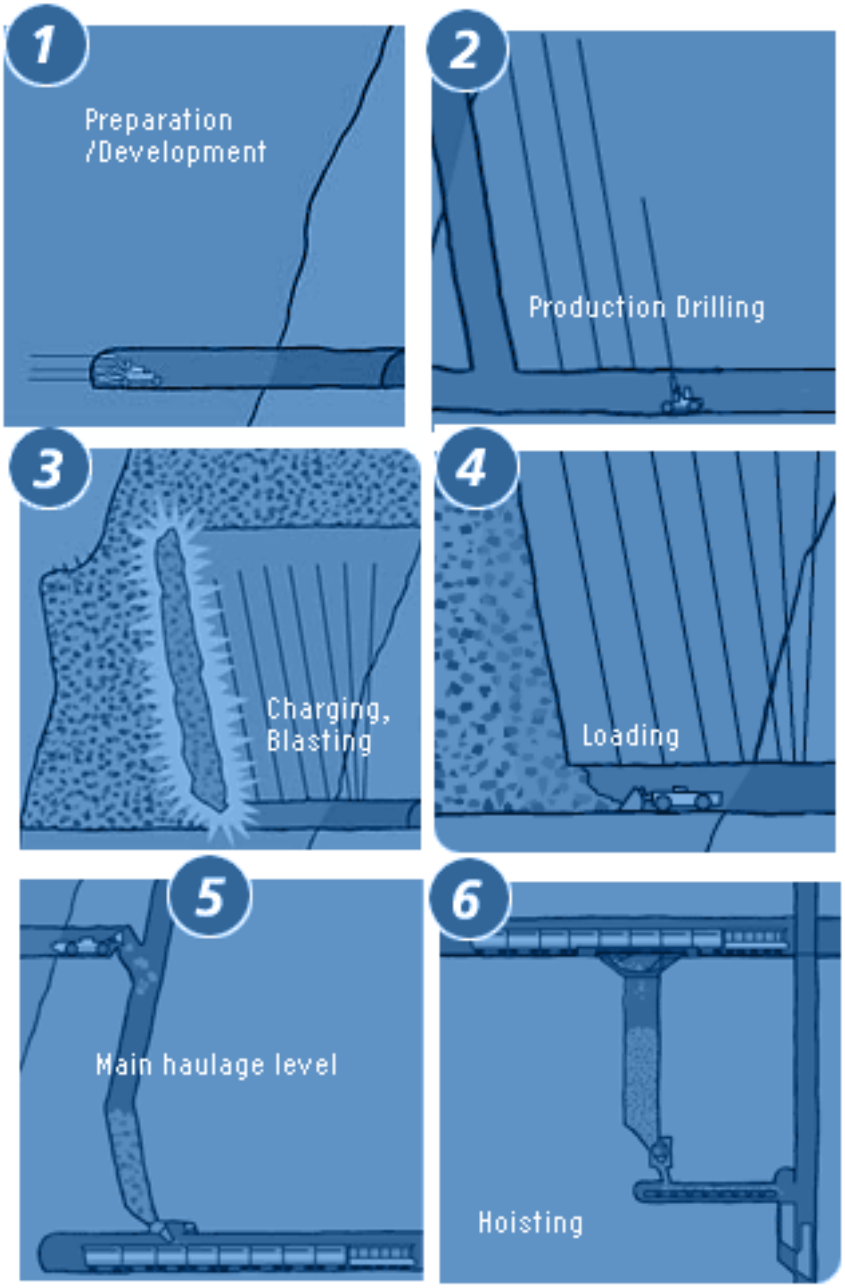

Figure 2.3: Overview of large scale sub-level caving mining method showing steps 1 to 6. Adapted from [14].

2. In step 3 the holes are charged with explosives and blasted to loosen and collapse the ore. After the fumes and dust from the explosion have been ventilated, the LHD vehicles can move in, in step 4 to load and transport (haul) the ore to the ore pass in step 5. From here the ore is loaded into trains which in turn transport the ore to the hoists for transport to the surface and further processing.

In a typical mechanised block caving mine the average haulage distance for the return trip carried out by an LHD is typically 220 meters. According to research carried out at Premier Diamond mine [15], in a shift lasting 9.2 hours, records show that the average utilisation of an LHD is just 4 to 5 hours per shift. [15] cites three main causes for this in order of importance, namely:

1. Tip availability.
2. Unscheduled delays.
3. Scheduled delays.

The first item namely, tip availability, refers to the availability of an ore pass or handling point for the LHD to dump its load and return to the drawpoint to collect more ore. This issue can be addressed by implementation of a vehicle dispatch system and is discussed in [16].
Unscheduled delays typically occur at the start and end of shifts and over tea breaks when the LHD drivers take longer than the allocated time to return to work, or stop work prior to the end of the shift. An additional unscheduled delay which introduces an average delay of approximately 0.22 hours per shift is that of dust,[15]. The dust is caused by drawpoints coming down and from the road surface during loading and hauling. Dust impares visibility and reduces air quality forcing the LHD operators to stop until the dust has cleared.
Scheduled delays consist of maintenance periods and scheduled rest periods for the LHD operators.
The focus of this dissertation is on the modelling of an LHD vehicle for the purposes of implementing autonomous navigation and guidance for transporting the ore along the underground haulage (after loading) to the next handling point i.e. between steps four and five of figure 2.3. By automating the LHD haulage cycle it should be possible to reduce most of the delays affecting the utilisation of the LHD vehicles as identified in [15] and summarised above.

2.2 Trackless Mining Vehicles

An articulated vehicle is preferable in the narrow environment of an underground mine tunnel because of its higher maneuverability, [17]. One indication of the maneuverability of a vehicle is the characteristic of multi-axle vehicles that during cornering the midpoints of their axles tend to follow different trajectories. The difference between these trajectories can be used as a measure of how cumbersome the vehicle is. Figure 2.4 shows a comparison

between the difference in trajectories of the midpoints of the axles (referred to as the off-tracking error) of a car-like vehicle and an articulated vehicle,[17].

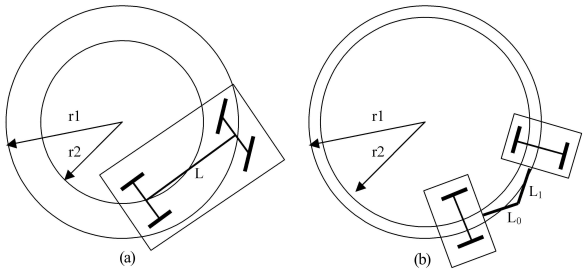

Figure 2.4: Comparison of off-tracking error of car-like vehicle and articulated vehicle.

For a car-like vehicle the off-tracking error is given by:

$$r_0 - r_1 = L\frac{1-\cos\beta}{\sin\beta} \tag{2.1}$$

where L is the length of the vehicle and β is the steering angle, while for an articulated vehicle the off-tracking error is given by:

$$r_0 - r_1 = L_1\frac{\cos(\frac{L_0}{L_0+L_1}\beta) - \cos(\frac{L_1}{L_0+L_1}\beta)}{\sin(\frac{L_1}{L_1+L_0}\beta)} \tag{2.2}$$

where L_1 and L_0 refer to the length of the two units of the vehicle, from the articulation joint to the centre of the axle. From equation 2.2 it is evident that when $L_1 = L_0$, the off-tracking error is zero and the two trajectories overlay one another, which is why most LHDs are built with the front and rear units of the vehicle being approximately the same size. This characteristic also simplifies the path-tracking problem.

2.2.1 LHD Vehicles

LHD vehicles as shown in figure 2.5 are produced by a number of manufacturers and are available in various different models using either diesel or electric power and in various sizes.

Typically the vehicles vary in length from 8 metres to 15 metres, and weigh between 20000 - 75000kg and have a transportation capacity of up to 25000kg.

The running costs of an LHD vehicle typically vary between ZAR 650000 and ZAR 1000000 per annum, [18], depending on the make and model of the LHD. The costs can be divided into operational and maintenance costs [18].

Operational costs consist of:

- Labour i.e. the driver.
- Fuel.
- Tyres.

Maintenance costs consist of:

- Labour
- Spares
- Oils

An LHD vehicle's body consists of two parts connected together by means of an articulation joint as shown in figure 2.5. The front and rear wheel sets are fixed to remain parallel with the vehicle's body and vehicle steering is achieved by means of a pair of hydraulic actuators altering the articulation angle of the vehicle. Figure 2.6 illustrates one of the pair of hydraulic actuators used to manipulate the articulation joint.

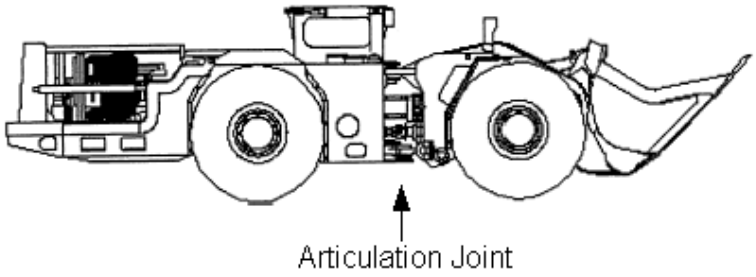

Figure 2.5: Side view of a typical LHD vehicle indicating the articulation joint.

An articulated truck can be modelled by a drift free nonlinear system, (detailed in chapter 4), with two inputs, namely speed and articulation angle, which are controllable [17].
Figure 2.7 illustrates the method of turning employed by an LHD vehicle.
Figure 2.8 shows the possible range of motion of the LHD vehicle's bucket with which the ore is scooped up from the muck pile. The scoop causes additional problems with respect to sensor positioning as no sensors can be attached to the bucket, and sensors also need to be positioned in such a manner that they are not obstructed by the contents of the bucket when loaded. The figure also illustrates the drivers positioning in a manually operated LHD vehicle. The driver is positioned facing perpendicular to the direction of travel of the vehicle. This is to allow the driver to have good visibility when driving the vehicle in forward or reverse gears just by turning his head.

Figure 2.6: Photograph of hydraulic actuator on LHD vehicle's articulation joint.

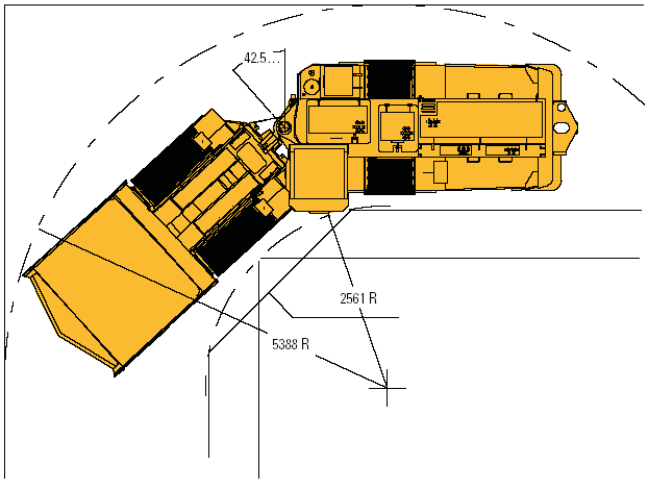

Figure 2.7: Schematic diagram of LHD vehicle showing the vehicle at maximum steering angle. Adapted from the Atlas Copco ST-3.5 6 Tonne Capacity Scooptram LHD technical specifications and performance data [19]

2.2.2 Trucks

The trucks used in trackless underground mines are produced by a number of manufacturers and are available in a number of sizes. Typically, as the tunnels in which they operate are not that confined, the trucks are larger than LHDs. Figure 2.9 and 2.10 show examples of an articulated mining truck.

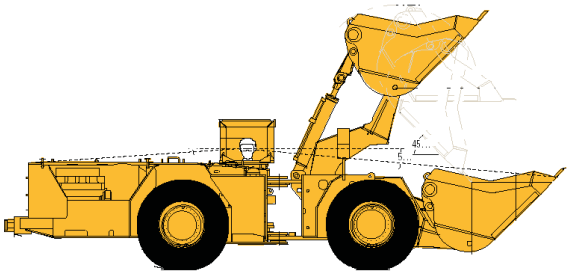

Figure 2.8: Illustration of possible range of motion of front bucket of LHD vehicle and drivers seating position. Adapted from the Atlas Copco ST-3.5 6 Tonne Capacity Scooptram LHD technical specifications and performance data [19]

Figure 2.9: This picture shows an example of two articulated mining trucks. Note that these trucks are articulated vehicles. Adapted from [20]

2.3 Chapter Summary

This chapter provides a brief introduction to the underground trackless mining environment. Two mining methods are introduced and the process of underground trackless mining is described and two types of vehicles which are typically used are discussed, namely Load-Haul-Dump vehicles and articulated mining trucks.

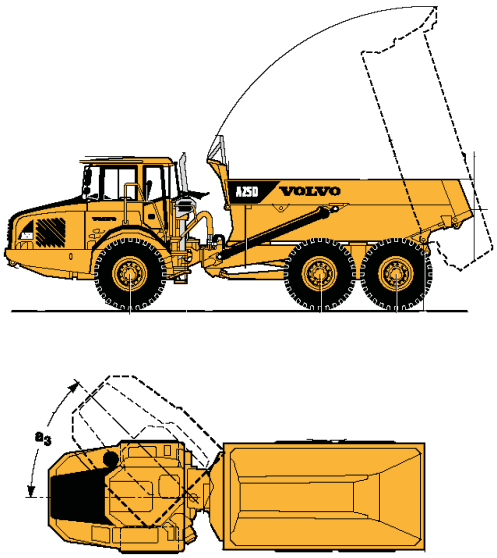

Figure 2.10: Schematic diagram of articulated mining truck. Adapted from [21]

Chapter 3

Navigation of a Mobile Robot

The aim of this chapter is to describe some of the background to autonomous vehicle guidance and navigation while also detailing certain problems unique to the underground mine environment and their solutions as described in the literature.

3.1 Introduction

In order for an autonomously guided vehicle (AGV) or mobile robot to be of any use it is necessary that the vehicle can navigate from one point to another within its environment without any human intervention. This implies that the control system of the vehicle either knows the environment(i.e. has a map stored) or is able to sense the environment. The robot or AGV also typically requires a path to follow and needs to be able to detect whether there is any danger of collisions with stationary or moving objects. The control system also needs to know the pose (position and heading) of the vehicle with respect to this path in order to control the vehicle to follow the path with the required accuracy.
There are however some autonomously guided vehicles which are not required to follow a specific path. An example of this is a vacuum cleaner mobile robot as described in [22] which can just wander around randomly. Eventually the vacuum cleaner robot would cover all of the area limited by the walls and the obstacles. This kind of navigation is called reactive navigation which will be discussed in greater detail later.

3.2 Robotic Environment

Mobile robotics research can be divided into indoor and outdoor environments and there is a large amount of research into both areas. It is therefore necessary to consider which category the underground mining environment resembles more closely so as to make use of the wealth of previous research in these fields.

The outdoor mobile robotic environment is typically characterised by rough terrain, where knowledge of the vertical elevation of the terrain is necessary to plan a path. Global positioning system data is also usually available for use in outdoor navigation, which is not the case for navigation of underground mine vehicles. In contrast the indoor environment consists of rooms, corridors and a planar floor, allowing navigation techniques to be developed which treat the world as a two dimensional environment. Typically sensors can be employed to follow walls and look for openings such as doorways to move through. As the walls are smooth, flat, and vertical it is possible to assume that the space the sensors detect at their height above the floor, also exists at the ground level. It is therefore safe for the robot to navigate through the area.
The underground mining environment in which the LHD vehicles have to operate, although physically harsh and time varying due to ongoing mining activities, resembles the indoor robotic environment more closely. This is due to the fact that they have a floor, ceiling and walls much like a corridor. The only small difference is that the floor of a tunnel is usually dirt that is not as smooth or entirely flat like that of a corridor.
In general each level of an underground mine can be considered as a horizontal plane, although in some places spiral ramp roads are used to link different levels. Maps of each level are readily available and due to the approximately rectangular cross section of most underground tunnels it is possible to use indoor mobile robot navigation techniques for the automatic navigation of underground mine vehicles [1].

3.3 Navigation Techniques

3.3.1 Dead Reckoning

Dead reckoning is the most widely used navigation technique for determining the pose of a mobile robot. It provides good accuracy in the short term, is inexpensive to implement and allows high sampling rates,[22]. An additional advantage of dead reckoning is that all navigation equipment can be contained onboard the vehicle.
Dead reckoning measures the two dimensional or three dimensional motion of the vehicle and determines the position by integrating the speed vector [22]. The length of the speed vector is the distance travelled and the direction is in the direction of the motion during that sampling interval.
There are several methods of determining the distance travelled by the mobile robot. The simplest method being to measure the rotation of the wheels of the robot. Alternatively ground speed radar can be used which is based on the doppler effect. Another alternative to determine the distance travelled is to double integrate the acceleration of the robot.

3.3.1.1 Odometry

The simplest form of dead reckoning is called odometry. As the name suggests the motion of the robot is measured by measuring the rotation of the wheels. Odometry requires instrumentation such as optical encoders directly coupled to the wheel axles or proximity sensors to detect cogs on the wheel. The heading can be calculated by measuring the distance travelled by the left and right hand side wheels which is called differential odometry, [22].
[23] lists the typical error sources related to odometry namely:
Systematic errors:

- unequal wheel diameters
- average wheel diameter differs from nominal wheel diameter
- misalignment of wheels
- finite encoder resolution
- actual wheelbase differs from nominal wheelbase

Non-Systematic errors:

- travelling over uneven surfaces
- travelling over unexpected objects in the ground
- finite encoder resolution
- wheel slippage due to:
  - slippery terrain
  - over acceleration (wheel spin)
  - fast cornering (skidding)
  - non-point contact with the ground
  - external forces (interaction with external bodies)

A distinction between systematic and non-systematic errors is of great importance for odometry error reduction. Systematic errors are serious because they accumulate constantly over time. Non-systematic errors occur unexpectedly and typically result in large position errors.
There are techniques which can be applied in order to reduce odometry errors as described in [23]. However in the best case the odometry error is in the region of 0.1%-0.5% of the distance travelled. There is unfortunately no upper limit to the error, [22].

3.3.2 Inertial Navigation

An Inertial Navigation System (INS) is an entirely self-contained navigation system. The system measures accelerations in each of the three directional axes, these accelerations are integrated over time to obtain the velocity, position and attitude of the vehicle. Inertial navigation makes use of gyroscopes and accelerometers to measure the change in state of motion of the robot. By noting changes in that state caused by the accelerations and combining these changes with the known starting point of the robot one can keep track of its current position, [22].

Although inertial navigation seems less prone to errors in comparison to odometry, as it is not dependant on ground conditions, inertial navigation systems are very prone to drift. This is because the position measurements are dependant on double integrations of the accelerations.

Regardless of the sensitivity of inertial navigation systems to drift it is possible to obtain sufficiently accurate systems. However the price is prohibitive to the practical implementation in the autonomously guided vehicle industry, [23]. According to [23] a high-end INS package for ground applications with an accuracy of 0.1% of the distance travelled would cost approximately $100 000 to $200 000.

The main challenge for inertial navigation in the future is to manufacture accurate gyros and accelerometers at a reasonable price.

3.3.3 Data Fusion Methods

Data fusion methods fuse information from a variety of sensors to provide and improved estimate of postion of the vehicle. Typically data fusion navigation techniques make use of an approximate estimate of the vehicle's position and heading, provided by means of dead reckoning, and a method to update the estimate periodically. The vehicle will make use of a map of the environment and a sufficient means of sensing natural or artificial beacons. Knowing the position of the beacons on the map and measuring the distance and heading to the beacons it is possible to reduce the dead reckoning error and improve the estimate of the vehicle's position and heading. Typically a Kalman filter would be used for this data fusion, [22].

Figure 3.1 shows the general structure of a Kalman filter used in data fusion navigation techniques. The dead reckoning sensors provide the next increment for the pose of the vehicle. This pose increment is added to the latest pose estimate to obtain the next pose prediction. Every time the vehicle sensors detect one ore more beacons an innovation is calculated from the difference between the observed pose and the predicted pose. The innovation is multiplied by the gain, K, to correct the predicted pose of the vehicle and

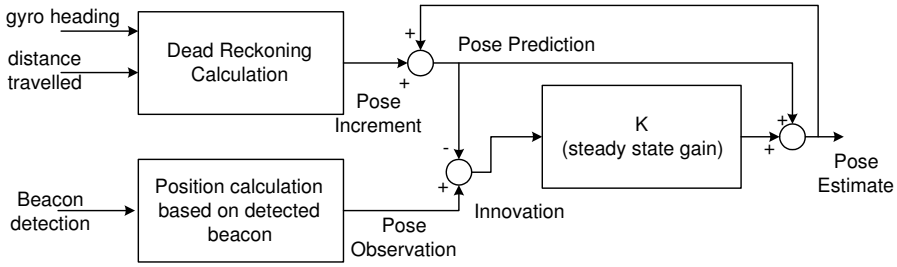

Figure 3.1: General structure of pose estimation using Kalman filter (adapted from [22]).

thus obtain the new pose estimate. The value of K is determined by the statistical parameters of the process model and the pose observation. More information on Kalman filtering can be found in [24].

3.3.3.1 Artificial Beacons

Artificial beacons are objects placed in known positions within the environment for the purposes of navigation. This however requires a large amount of building and maintenance work to install the beacons. Active beacons also have a further disadvantage in that they require a power source for each beacon. Artificial beacons do have the advantage that they can be designed in such a manner that they are easily and reliably detectable in the particular operational environment in comparison to natural beacons.
In order to calculate the pose of a vehicle in two dimensions either the distances or bearings to three beacons can be measured and used to calculate the position and heading of the vehicle by simple geometry. This process is referred to as trilateration if it is based on known distances or triangulation if it is based on known bearings,[22].
The distance measurement methods can be divided into the following groups, [22]:

- Triangulation
- Time-of-flight
- Phase shift measurement
- Frequency modulation
- Interferometry
- Swept focus
- Return signal intensity

Triangulation is in this case a range measurement method which obtains the range to a beacon based on angle measurement. An example of this is stereo vision systems in which two cameras in a known configuration pointed at the same scene and image analysis is used to find common objects in the image. The displacement between the objects common to both images is inversely proportional to the distance.
Systems that measure the bearing to several beacons can be divided into the following groups,

- Rotating laser,
- active beacons detected by camera with special optics,
- radio location.

Details of various artificial beacon navigation techniques are given in [22]. [22] includes Global positioning system (GPS) navigation techniques as an artificial beacon based method which has the advantage of not requiring beacons to be installed in the environment. GPS navigation is however only useful in outdoor navigation environments and therefore is not suitable for underground mine vehicles.

3.3.3.2 Natural Beacons and Map Based Recognition

Pose estimation and localisation based on artificial beacons is relatively simple and reliable. Unfortunately, in underground mining applications, the use of artificial beacons is undesirable for reasons of both safety and productivity. It is undesirable to have to send personnel into a potentially hazardous mining environment for long periods of time installing and mapping the locations of the artificial beacons. This process would also delay the ability of vehicles to take new routes into use which would reduce productivity in the ever changing environment of an underground mine.
For these reasons it is desirable to make use of natural beacons which consist of objects or features of the environment which the autonomous vehicle can use to determine its position within the environment. The term natural refers to all objects within the environment including man-made objects not built for the purpose of navigation, which can be used for position estimation. Examples of natural beacons could include walls, pillars, light posts or mine tunnel walls. In this way the autonomous vehicle can be used in a new environment with minimal setup and installation costs.
Map based recognition is an important part of navigation using natural beacons. A map is used to estimate the pose of the vehicle by comparing the features obtained from the sensor data to the features of the stored map of the environment and searching for the

best correspondence. The position of the vehicle can then be estimated by comparing the location of the common features. These feature are referred to as the natural beacons. In order to use natural beacons for navigation involves several phases and related problems as detailed in [22] are

1. selecting the natural beacons,
2. determining the position of the beacons,
3. storing beacon position in a database,
4. extract beacon position from sensor data,
5. match beacons to those stored in database,
6. estimate vehicle position.

Steps 1 to 3 above are the initialisation phase and only need to be performed when the vehicle is being used on a new route. Steps 4 to 6 are performed when the vehicle is driving in autonomous mode. Typically in the initialisation phase the vehicle would be taught a new route by having a driver drive the vehicle on the desired path. The sensors would then record all the necessary information during this teaching phase and build the map of the environment. When operating in autonomous mode the vehicle uses this map for position estimation.
The logical ideal for natural beacon based navigation is a concept known as Simultaneous Localisation And Mapping (SLAM). In this approach the autonomous vehicle is able to build a map of it's environment without prior knowledge of it's position and incrementally expand the map based on known beacons already learned. SLAM has been the topic of much research, see for example [25], [26] and [27] but as yet has not been implemented in the underground mining environment [1]. More detail on SLAM is given in section 3.5 of this chapter.
More detail on natural beacon based navigation can be found in [22].

3.4 Path Tracking Control

The objective of the navigation techniques is essentially to achieve path tracking control. The objective of path tracking control is simply to allow the vehicle to follow a specified path with the required accuracy for the particular application. Typically one point on the vehicle is selected as the navigation point. For a conventional car-like vehicle layout this point is usually chosen as the midpoint of the rear axle. In most LHD vehicles the

navigation point is also usually chosen as the midpoint of the rear axle as most navigation equipment is usually stored on the rear of the vehicle, [28]. However in terms of path tracking it is irrelevant whether the midpoint of the front or rear axle of an articulated vehicle with equal half lengths is chosen as the navigation point since the midpoints of both axles follow the same trajectories as illustrated in figure 2.4 of chapter 2 .
Path tracking control requires determining the error in the current pose of the vehicle from that of the desired reference path, calculating the amount of corrective action and adjusting the steering to decrease the error. The error in the vehicle's orientation consists of a heading error and a lateral displacement perpendicular to the reference path.
Path tracking controllers are divided into two main categories:

1. Vehicle orientation control is based on direct measurement of the deviation from the path. The vehicles orientation is not known in any coordinate system.

2. The vehicle has a predetermined path stored in it's memory and it continuously tries to measure it's position and minimise the error between the measured vehicle orientation and the reference orientation.

Category 1 is typically used by autonomously guided vehicles (AGVs) that follow "rail-like" guides such as buried wires or painted lines on the floor. This approach is an example of a navigation technique called reactive navigation. This method of path tracking control suffers from the deficiency that it does not allow high speed and good accuracy. This is because the method does not allow for any look ahead and therefore it is not possible for the vehicle to adjust for changes in the path in advance.
Navigation techniques which fall into category 2 are called absolute navigation techniques. Typically these techniques offer better chances of high speed navigation and good tracking accuracy. This is because the path is known in advance and the vehicle can take upcoming changes in the path into account in advance and adjust the vehicle speed accordingly, [22]. More detail on absolute and reactive navigation techniques with respect to LHD vehicles are given in the next section.

3.5 Advanced Navigation Algorithms

Typical industrial autonomous vehicle applications make use of standard navigation loops which rely on special infrastructure installed in the area of operation. The installed infrastructure or beacons are used in order to achieve localisation (the ability to locate the vehicle in space) and relate this location to the environment in order to perform useful navigation. As mentioned previously, the installation of infrastructure into the underground mine environment is undesirable.

Most navigation systems make use of this installed infrastructure (or alternatively GPS data in outdoor environments) as a source of absolute position information. In cases where this information is not available the localisation problem can still be solved by building a relative map of the area and localising with respect to this map simultaneously [29].As mentioned earlier this is the concept referred to as Simultaneous Localisation and Mapping or SLAM and has not been implemented in the underground mine environment [1].

A probabilistic approach is presented [30] to solve the localisation or the map-building problem when either the map or the position of the vehicle is unknown. This approach is based on the approximation of the probability density function with samples, called particles and is commonly referred to as particle filtering. More information on particle filtering can be found in [31]. Particle filters have been applied very successfully in a number of indoor mobile robot navigation applications, [29]. While SLAM is the logical ideal for autonomous navigation there are a number of problems implementing the algorithms. The main problem with SLAM navigation algorithms is that they are computational intensive. It is known that the complexity of the SLAM algorithm can be minimised to the order N^2, where N is the number of landmarks on the map. Therefore for long duration navigation tasks the number of landmarks increases and eventually the onboard computing power is insufficient to update the map in real time, [29].

Another potential problem with SLAM algorithms is that consistent performance is dependant on the correct association of the sensed features to the mapped features. This can cause problems if the autonomous vehicle is operating in rough terrain as the vehicle orientation used to validate the associations may possess a large degree of uncertainty making correct association of sensed features to mapped features difficult. There are however techniques such as batch data acquisition, [29] which can be used to reduce this problem.

3.6 Navigation of LHD vehicles

3.6.1 Absolute Navigation

In this navigation scheme the absolute position of the autonomous vehicle is known at all times relative to some fixed real-world co-ordinate system. In this technique the path for the vehicle is defined in this same co-ordinate system and the vehicle attempts to remain on the designed path as accurately as possible. This path-tracking problem for an articulated vehicle is addressed by [5] and [32].

In order to implement an absolute navigation system it is necessary to estimate the

absolute position of the vehicle, which is referred to as localisation. This is usually achieved by means of fusing data from on-board sensors such as inertial measurement and heading angle measurement, and external measurements such as odometry. Such measurements are unfortunately prone to errors which accumulate over time and it is therefore necessary to periodically correct the position estimates by means of artificial beacons such as radio tags, or reflective markers. The position estimate together with a map of the tunnels is used to navigate the robot through its environment. Collisions are avoided by means of range sensors being laser, or ultrasonics, which need to be capable of detecting the tunnel walls and any obstacle that may occur in the tunnel.

Autonomous vehicles that navigate by means of the data fusion algorithm are more flexible in their use as they do not require expensive rail guides. Such vehicles are still limited by the coverage of the available maps and artificial beacons. However, maps are readily available in the underground mining environment and there are a number of navigation systems that operate using this type of architecture.

The first absolute navigation system discussed is that of Q-Navigator. This is an absolute navigation system that is commercially available and has been implemented on over 700 autonomously guided vehicles, [33].

Q-Navigator is a High Speed Underground Navigation System, (HUNS) which is based on the navigation system developed by the University of Luleå in Sweden from 1986 to 1989.

The HUNS consists of a rotating laser scanner and a navigation computer. The laser scanner rotates an infrared laser at 12 revolutions per second. The laser is reflected back to the laser scanner from retro-reflective targets mounted on holders on the tunnel walls. The angle of the rotating head is recorded when the beam is reflected back into the scanner. The measured angles together with a map of the target positions are used in the navigation algorithm to determine the position and heading of the vehicle. The high sampling frequency of the laser is said to make the system insensitive to model errors such as wheel slippage.

The system unfortunately requires a rather large overhead of installed infrastructure as the system needs at least four reflectors to be visible at any one time. The reflectors are also affected by dust as this decreases their visibility and can be a potential safety hazard.

[8] proposes a similar absolute localisation and navigation scheme, but which does not require artificial beacons. The system they propose uses a minimal-structure algorithm for computing accurate estimates of the vehicle's pose for the navigation of an LHD based on an existing map of the underground tunnel. The map used consists of a series of short line segments, referred to as poly-lines, which represent the approximate geometry of the mine tunnel walls. The map is constructed from data obtained by a scanning laser-range

finder using the time-of-flight principle. Range data obtained from the range finder is then matched to the segments of the existing map, based on the minimum distance principle. An Extended Kalman filter (EKF) is then used to account for uncertainty in the motion estimation. The EKF employs a nonlinear process model to account for effects of slipping as well as a nonlinear observation model for the range measurements provided by the laser scanner. This observation model is derived from the basic principles of analytic geometry and vector calculus. The Iterative Closest Point (ICP) algorithm is then used to solve the problem of obtaining correspondence to the pre-existing map. Details of the ICP algorithm can be found in [8].

Another LHD navigation technique which relies on absolute navigation, or an approximation there to, is that described by [7]. The emphasis in this approach has been to design navigation systems that require no extra infrastructure to be installed in the mine tunnel. The navigation system is based on teaching the route segments by having a human operator drive the vehicle through the route initially and recording the environmental model while the teaching is taking place. Laser scanners are then used to correct the drift of dead reckoning positioning while the vehicle drives in automatic mode. The navigation system is based on the fusion of dead reckoning (odometry) and position measurement using the natural features of the tunnel walls. All the navigation equipment, which consists of an articulation angle sensor, an odometer, a gyroscope and two laser scanners and a Pentium level computer running the QNX operating system are entirely mounted on the LHD. The computer runs the navigation program that consists of 16 tasks being executed in parallel. The odometer, articulation sensor and gyroscope are used in determining the pose of the vehicle by means of a discrete kinematic model that does not include slip. The odometer however is mounted on the cardan or driving axle of the vehicle allowing it to measure the mean of the distance travelled by the left and right hand side wheels, allowing a resolution of better than 5mm and a practical accuracy in the region of 0.5-2% depending on the terrain.

A new path is taught to the navigation system by having an experienced driver drive the route in both directions. This approach has the advantage that when the vehicle is driving in automatic mode it will take into account the local conditions of the path, as the experienced driver did. When the route is driven in automatic mode the vehicle follows the reference trajectory by correcting its heading when necessary. This is accomplished by the navigation system constantly measuring the position and heading of the vehicle using dead reckoning. Due to the drift of dead reckoning the position and heading estimates must be corrected frequently. This is done by using the environmental model obtained during teaching to estimate the drift in the dead reckoning accuracy, which is then corrected. This system also has the added advantage that it records the position of the bucket during

teaching and this can then be used during automatic driving as well.
The logical ideal for the absolute navigation paradigm is Simultaneous Localisation and Map Building (SLAM) or Concurrent Mapping and Localisation (CML) where no prior map is required and the map is generated as the autonomously guided vehicle moves around the world for the first time, without the need for prior training.

3.6.2 Reactive Navigation

Reactive navigation is a simple type of navigation which has been used since the 1960s, [1], in which the autonomous vehicle reacts to objects in its immediate environment in order to continue moving forward. Examples of reactive navigation systems used in the underground mining environment are those that follow painted lines, retro-reflective strips or light emitting ropes on the tunnel floor or roof (one such example is described by [5]). These navigation systems typically use CCD cameras to detect the relative position of the line being followed immediately above or below the vehicle. These systems offer very little look-ahead and thus heading changes that need to be made cannot be anticipated which makes them unsuitable for driving at high speeds.
For the case of an LHD vehicle operating underground the essence of the driving task is to stay in the middle of the mine tunnel and avoid hitting the tunnel walls. This can be achieved by application of wall following which is a technique that has been popular in indoor mobile robotics. Ultrasonic sensors and laser range finders have been used successfully for determining the distance of the vehicle from the mine tunnel wall, [1], [9], and [34], provided that it is possible to attain significant look-ahead to detect the walls ahead of the vehicle [1]. A reactive navigation system was also developed by [9] for the automation of an articulated underground mine truck which used ultrasonic range sensors to perform environment mapping and wall following.
The advantage of reactive navigation is that the robot does not need to "know" where it is within its environment with respect to a global co-ordinate frame of reference, it is only necessary to keep track of obstacles in its immediate vicinity. Two popular techniques used in wall following are potential field and neural network methods.

3.6.2.1 Potential Field Methods

Potential field methods have been used for navigation by robotics researchers since the 1980s, [1]. The principle is to treat the vehicle as a particle that is attracted by a potential field radiating from its intended destination and repulsed by potential fields radiating from obstacles. A local path plan is then constructed by applying a force based on the sum of the potential fields, to a general desired path whose end is fixed to the vehicle. This is

normally an iterative process and hence suffers from the limitation that the vehicle may become trapped in a local minimum and be unable to reach its goal, [1].

3.6.2.2 Neural Network Methods

Neural networks have the advantage that they are fast to execute and can therefore be applied to high-speed autonomous vehicles. A vehicle can be taught to steer using a neural network by making an association between the sensor data and steering angle allowing the vehicle to steer through previously unseen terrain, [1].

3.6.3 Path Planning and Decision Making

A reactive navigation system does not perform any path planning on a global scale. A pure wall following LHD vehicle will move along a tunnel until it encounters a dead end where it will stop. In order to complete a useful mission the vehicle needs to be able to plan a path to its destination. In the underground mine environment the decision process is quite limited as there is only a choice of going forward or backward along the mine tunnel, however it is necessary to choose the correct path to take at intersections. This leads to two problems, firstly identifying which intersection it is and secondly what action to take at the particular intersection.
In an absolute navigation environment the autonomously guided vehicle has a global map of its environment, and localization information is available and it is possible to make a decision. The localization accuracy does not need to be accurate; it is only necessary to determine which junction the vehicle is approaching and from which direction. Beacons, such as radio tags or bar codes, may also be placed at intersections to obtain absolute positional information [1].
A relative route can also be applied where the autonomously guided vehicle is given a sequence of instructions to follow in order to reach its goal. For example the vehicle may be told to drive 100m and turn left at the next T-junction, in a manner similar to the way in which humans verbally describe a route to another person. Such a technique has been implemented successfully in combination with reactive wall following [1].

3.7 Safety

This section elaborates further on some of the safety issues mentioned in Chapter 1 that need to be taken into account in the implementation of a physical autonomous underground mine vehicle system.

3.7.1 Obstacle Detection and Collision Avoidance

A reliable obstacle detection system for an autonomously guided mining vehicle is essential to enable the detection of obstacles that could potentially be dangerous to the safety of the vehicle itself, other vehicles or personnel while navigating through the mine. Obstacles could include people, other vehicles, or objects such as fallen rocks or pipes hanging from the tunnel roof with which the vehicle could collide.

The development of reliable autonomous vehicle navigation systems is difficult in the harsh environment of an underground mine. The operating environment could include dust, mud, high humidity, diesel fumes, extremes of temperature, severe vibration, and bright light sources.

There are two distinct approaches to obstacle detection namely direct obstacle detection and terrain-mapping and navigation, [35]. In direct obstacle detection the obstacles themselves are detected by actively illuminating a scene and waiting for reflections. This approach merely detects obstacles and passes the information to the actual navigation system.

In terrain mapping and navigation obstacles are not explicitly detected but rather the free-space or navigable area in front of the vehicle is sought and everything that is not navigable is considered an obstacle. The location of the free space is then sent to the navigation system.

Obstacle detection systems are also categorised by the type of sensors they use. The four most commonly used sensors being used are radio tags, radar, lasers, and cameras for computer vision.

3.7.1.1 Sensors

Laser based systems have proved to be effective in both direct obstacle detection and terrain-mapping navigation techniques. Laser based systems do however suffer significant limitations due to a lack of penetration through dust and fog. Dust and fog effects vary with the laser wavelength. Additional limitations are imposed by eye safety concerns in areas where humans are present, as well as the reliability of mechanical scanning systems. These consist of moving parts which need to be robust enough to survive extreme vibrations encountered in the mining environments [35].

Radio tags are probably the simplest and cheapest form of obstacle detection. All site personnel and vehicles carry a tag. The tag can be either active or passive. In the case of passive tags the autonomous vehicle carries both a radio transmitter and receiver; the vehicle transmits a signal to all tags in range and the tags reply. If active tags are used the vehicle is only fitted with a receiver and each tag transmits its own signal. These

systems suffer from three fundamental problems:

- The range of the radio signal varies depending on the terrain and is therefore unreliable;
- obstacles which do not have tags such as fallen rocks;
- non-functioning tags which are not possible for the autonomous vehicle to detect, could lead to accidents [36].

Radar based collision avoidance systems have been developed by a number of research groups as part of various Intelligent Vehicle Highway Systems (IVHSs). Most of these system are designed to work in an environment where the vehicle will not pitch and roll significantly, however this is not the case for mining vehicles and hence it is unlikely that any of the current automotive systems would be suitable for the mining environment. Systems have however been developed in which targets placed on obstacles are used to reflect the radar energy back to the receiver much like the radio tag system,[36].
A number of computer vision systems using cameras have been developed however they also suffer from poor performance due to fog and dust as with laser based systems. The computer vision systems also require good lighting, which can be a problem in the underground mining environment.

3.7.1.2 Fail Safety

An obstacle detection system should ideally be a fail-safe system in order for the autonomous vehicle navigation system to be accepted in the field. In the case of direct obstacle detection for an autonomous vehicle navigation system the decision to move forward is based on null information, in other words that no obstacles were found in the vehicle's path. There are two possible sources of null information. Firstly that there is indeed no obstacle present and secondly that the obstacle detection system failed to detect an obstacle for some reason. Hence trying to detect obstacles in the unstructured underground mining environment can never be made fail-safe,[36].
According to [36], it may be possible to create a fail- safe system using the terrain mapping and navigation technique in which the vehicle seeks free-space in front of the vehicle because this method is based on positive information confirming the presence of a navigable area rather than null information. Any failure in such a system will produce null information, which is invalid and hence the system will know when a failure has occurred.

3.8 Chapter Summary

This chapter provides an introduction to the navigation of an autonomously guided vehicle or AGV. Several navigation techniques developed in the field of mobile robotics are introduced and discussed. After providing an overview of navigation algorithms in general the application of these algorithms specifically to LHD vehicles is discussed. Finally the requirements for the autonomously guided LHD vehicle to navigate safely in an underground mine are discussed.

Chapter 4

Vehicle Modelling Background

In order to design a navigation system for an autonomous vehicle it is necessary to have a vehicle model that describes the vehicles position and other vehicle parameters through time. In this chapter some background and terminology to vehicle and tyre modelling is introduced and different modelling approaches discussed. Chapter 5 will describe how these techniques have been applied specifically to LHD vehicles.

4.1 Fundamentals of Vehicle Modelling

Vehicle modelling is concerned with the movements of vehicles on a particular road surface. Movements of interest include acceleration and braking and turning behaviour of the vehicle. The behaviour of the vehicle is determined by the forces imposed on the vehicle from the tyres and the vehicle geometry.

4.1.1 Lumped Mass

A vehicle is made up of a number of components distributed within the vehicle envelope. For the analysis of many vehicle characteristics it is often acceptable to view the vehicle as a lumped mass considering that all the components of the vehicle move together. The vehicle mass can then be represented as one lumped mass at the centre of gravity (CG). For acceleration/braking and elementary turning analysis one mass is sufficient. As discussed in detail in chapter 5 the location of the centre of gravity (CG) of an LHD can have a marked influence on the vehicle's turning characteristics, the CG also moves depending on the load of ore being carried by the vehicle which can have a marked influence on the vehicle's handling characteristics.

4.1.2 Vehicle Axis System

In models of conventional car-like vehicles the coordinate system used is defined by the Society of Automotive Engineers (SAE) in document number SAE J670e [37] as shown in figure 4.1.
The x-axis points in the forward or longitudinal direction, the y-axis or lateral direction is positive when it points to the right of the driver (in a conventional car), and the z-axis points to the ground following the convention of the right hand rule.

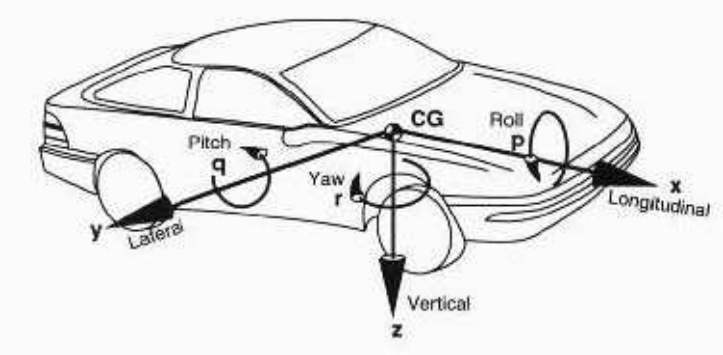

Figure 4.1: Vehicle axis system as defined by SAE [37].

This is also the convention followed in this dissertation unless stated otherwise. In the derivation of the complex vehicle model of chapter 5 it was necessary to attach a coordinate system to each half of the vehicle.
In studies of vehicle handling and directional control only the x-y plane of the vehicle is typically considered. The vertical axis is typically introduced into a model to study the effects of pitch and roll on the vehicle. More detail on the application of theses modelling techniques to LHD vehicles is given in the following chapter.

4.1.3 Dynamic Axle Loads

Determining the dynamic axle loads of a vehicle is an important step in the analysis of a vehicle as axle loads determine the tractive effort obtainable from each axle which affects acceleration, braking and the cornering characteristics of the vehicle's tyres,[38].
Figure 4.2 shows the forces acting on a vehicle on a plane inclined at an angle of Θ degrees. Considering figure 4.2 the most significant forces shown are:

W is the weight of the vehicle acting at its centre of gravity with a magnitude equal to its mass multiplied by the acceleration due to gravity (g). On an incline the weight has two components, a cosine component perpendicular to the road and a sine component parallel to the road.

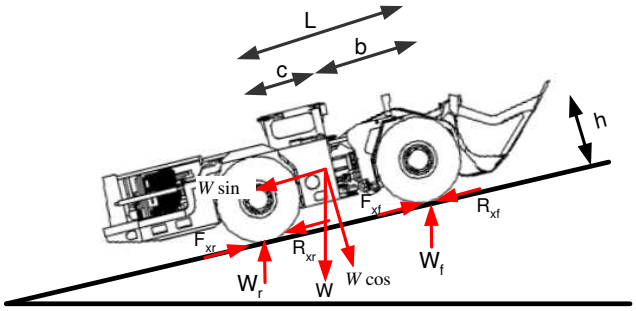

Figure 4.2: Diagrammatic representation of forces acting on a vehicle on an inclined plane..

The tyres experience a force normal to the road, denoted by W_f and W_r, representing the dynamic weights carried by the front and rear wheels respectively.

Tractive forces F_{xf} and F_{xr} act in the ground plane of the tyre contact patch.

Rolling resistance forces R_{xf} and R_{xr} act in the ground plane of the tyre contact patch

The loads carried by each axle consist of a static component and a component of load transferred from front to rear or vice versa. The load on the front axle can be computed by summing the torques about the rear tyre contact point. Similarly, the loads on the rear axle can be computed by summing the torques about the front tyre contact point. The expressions for the dynamic axle loads for the setup shown in figure 4.2 are given in equation (4.1) and (4.2).

$$W_f = \frac{(Wc\cos\theta - \frac{W}{g}a_x h - Wh\sin\theta)}{L} \tag{4.1}$$

$$W_r = \frac{(Wb\cos\theta - \frac{W}{g}a_x h + Wh\sin\theta)}{L} \tag{4.2}$$

4.2 Kinematic Modelling

4.2.1 Low Speed Steering Models

In kinematic or low speed steering models the motion of a wheeled vehicle is determined only by the pure rolling of the wheels,[39]. The velocities of the centres of all the wheels are assumed to be in the midplane of the wheel, that is there is no difference between the rotational plane of the tyre and the heading of the tyre. This means that the slip

angles α are infinitesimally small. In this condition the wheels can exert no cornering force to balance the centrifugal force caused by cornering and therefore these models are only valid at infinitesimally small velocities,[39]. Figure 4.4 illustrates the concept of a slip angle, a dynamic effect present in all pneumatic tyres. Details on slip angles can be found in the following section.

Due to the confined nature of the environment (see figure 4.3) LHD vehicles usually operate at relatively low speeds, typically below 28 km/h. For this reason the path-tracking problem can and has been based on the kinematic model only. This is due to the fact that the dynamics of the vehicle and tyre deformation are believed to have little effect and may be neglected at these speeds, [40], [41].

Figure 4.3: LHD vehicle in a typical mine tunnel, [Anon].

The main effects which need to be taken into consideration when developing a vehicle dynamic model consists of forces generated by the vehicle's tyres, and the energy absorption in the vehicle's suspension. As an LHD vehicle typically has a minimal amount of suspension travel, and is very stiffly sprung due to the heavy loads the vehicles normally carry, the dynamic effects caused by the suspension can typically be neglected. This is the approach followed in this dissertation. The dynamic effects of the tyres on the vehicle's performance is however vitally important as all external forces that act on the vehicle (when in normal operation and not loading) and determine its motion are applied through the tyres. The tyres are required to generate the necessary longitudinal and lateral forces to allow a vehicle to maintain its desired trajectory. The primary task of a tyre model is therefore to determine the lateral and longitudinal forces generated by the tyres as described in the next section.

4.2.2 Tyre Forces and Moments

Determining the longitudinal force generated by a tyre is a relatively simple task. The force can be determined based on the friction coefficient of the surface the tyre is being used on, the vertical load on the tyre and the acceleration of the vehicle. To determine the cornering (lateral) forces generated by the vehicle's tyres is probably the most difficult task in defining the forces acting on a vehicle, [42]. During cornering the tyres of the vehicle must generate lateral forces to turn(yaw) the vehicle and keep the vehicle on its desired curved trajectory. Obtaining an accurate model for these forces is a complex task.

4.2.2.1 Slip Angles

During high speed cornering a rolling pneumatic tyre is subjected to a lateral force causing the tyre to be deflected to the side. This phenomenon is referred to as slip. An angle is created between the direction of the tyre heading and the direction of travel which is referred to as the slip angle, [38].

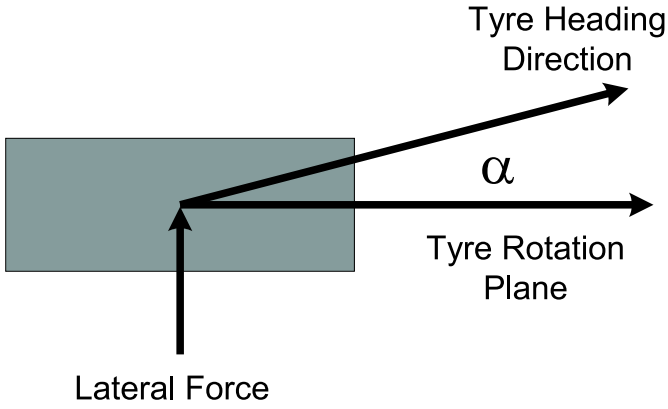

Figure 4.4: Illustration of tyre slip angle α.

The lateral force behaviour of rolling tyres is characterised only in steady state i.e. constant load and slip angle. This behaviour can be characterised by performing measurements on the tyre to determine its behaviour under different vertical loads and different lateral forces in order to characterise the tyre. An example of the results of such an experiment carried out for a bias-ply tyre are shown is figure 4.5 adapted from [42].
The property of primary importance to the turning and stability behaviour of a motor vehicle is the initial slope of the lateral force curve in figure 4.5. The slope of the curve evaluated at zero slip angle is known as the cornering stiffness denoted by C_α.

$$C_\alpha = -\frac{\partial F_y}{\partial \alpha}|_{\alpha=0} \tag{4.3}$$

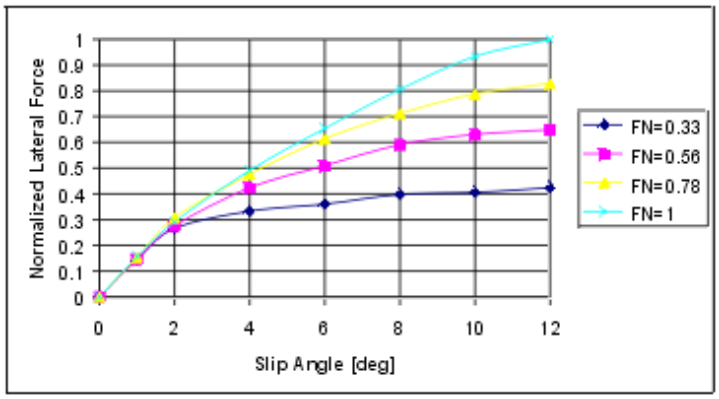

Figure 4.5: Normalised Lateral force versus slip angle for bias ply tyre.

Factors which influence cornering stiffness of a tyre:

- Tyre Type: In general radial tyres have a higher cornering stiffness than bias-ply tyres, [38]. Although the tyre construction has an important influence on the cornering stiffness one other important factor is that of the aspect ratio of the tyre. The term aspect ratio refers to the ratio between the tyre's width and the cross sectional height of the side wall. Tyres with lower aspect ratios, often referred to as low profile tyres have higher cornering stiffness coefficients.

- Load: The cornering force at a given slip angle rises with increased vertical load. This does not occur in a linear way. More details can be found in [38].

- Inflation pressure: Increasing the inflation pressure of a tyre intuitively results in an increase in cornering stiffness of the tyre as the tyre carcass stiffness increases. However, increased inflation pressure increases the tyre carcass stiffness but also reduces the length of the tyre contact patch with the road and it is therefore not possible to generalise the net influence of increased inflation pressure on all types of tyres.

- Size and width: For a given vertical load condition, larger or wider tyres have a greater cornering stiffness [38]

- Tread design: The lateral compliance of the tread rubber acts as a series spring in the generation of lateral force response to slip angle. Therefore tread design has a potential influence on cornering stiffness, [38]. In general a tread design with a more open pattern with deeper grooves and less support from one tread block to another will cause greater lateral compliance in the tread and therefore reduce the cornering stiffness, [38].

Cornering stiffness is one of the primary factors affecting the steady-state and transient properties of vehicles. The effect of cornering stiffness on understeer/oversteer gradient of a vehicle can be found in [39], [38].
By SAE convention, a positive slip angle produces a negative force on the tyre (to the left of figure 4.6), implying that C_α must be negative. Therefore in order to get around this problem the SAE defines the cornering stiffness as the negative of the slope so that C_α takes on a positive value.

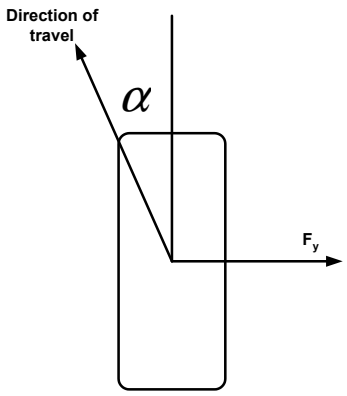

Figure 4.6: Diagram showing sign convention used in defining slip angles. The diagram shows a positive lateral force F_y and therefore the slip angle α is negative.

As can be seen from figure 4.5 at low slip angles the relationship between the lateral force and slip angle is almost linear where the cornering force is given by (4.4).

$$F_y = C_\alpha \alpha \tag{4.4}$$

This linear relation only holds for slip angles up to approximately five degrees which is generally sufficient except in extreme maneuvers. More details on comprehensive tyre

models are provided later in this chapter.

4.2.2.2 Friction Circle Concept

When a tyre is subjected to combined braking/accelerating and cornering the lateral and longitudinal forces depart from the values obtained under independent conditions. In general the application of a longitudinal force (accelerating/braking) generally tends to reduce the lateral force at a given slip angle condition and application of a slip angle reduces the longitudinal force developed under a given braking condition, [38].

$$\mu = \frac{F_{friction}}{F_{normal}} \tag{4.5}$$

The friction limit for a tyre, regardless of direction, is determined by the coefficient of friction multiplied by the vertical load, as can be seen from equation 4.5.
The friction force can be used for lateral force, brake force or a combination of the two in either the positive or negative directions. The limit of the available traction is therefore a circle in the plane of the lateral and longitudinal forces.

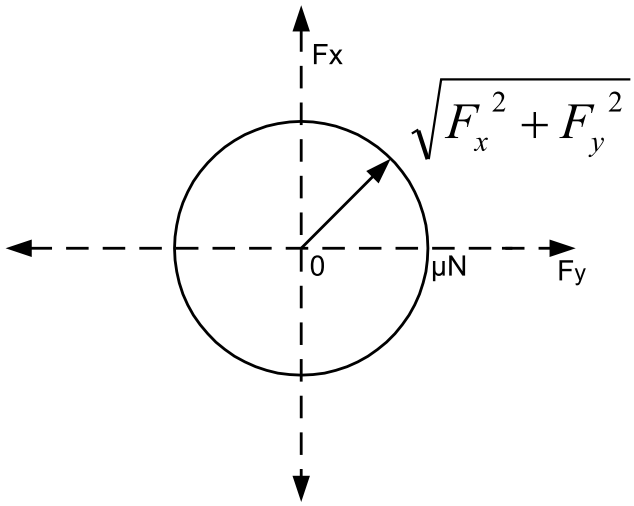

Figure 4.7: Diagrammatic illustration of friction circle concept

4.2.2.3 Friction Ellipse Concept

The concept of a friction ellipse is based on the concept of a friction circle. Certain specialised tyres are optimised for lateral or longitudinal traction which results in the limit of traction no longer being a circle but instead becoming an ellipse.

4.2.2.4 Comprehensive Tyre Modelling Techniques

Comprehensive tyre modelling is typically accomplished in two ways, the first being curve fitting of experimental data and the second is the analytical tyre model. Curve fitting of experimental tyre data can give more accurate predictions of force traction fields but the data is highly sensitive to the type of tyre being used (size, constructions, inflation pressure, tread pattern etc.) In an analytical tyre model the contact patch of the tyre is typically divided into two zones namely the sliding zone and the adhesion zone.
Shear stresses in the sliding zone are determined by the frictional properties of the tyre/road interface. Shear stresses in the adhesion zone are determined by the elastic properties of the tyre. Two of these properties are the cornering stiffness C_α and longitudinal stiffness C_s which are first order approximations of the tyre force elastic properties,[43].
In the complex vehicle model derived in chapter 5 an analytical tyre model is used. For the purposes of simulating a vehicle's dynamics given the road condition, vertical load on the tyre and the tyre operating condition such as lateral slip angle and longitudinal slip ratio; the tyre model is used to predict the longitudinal (tractive/braking) and lateral (cornering) forces as illustrated in 4.8.

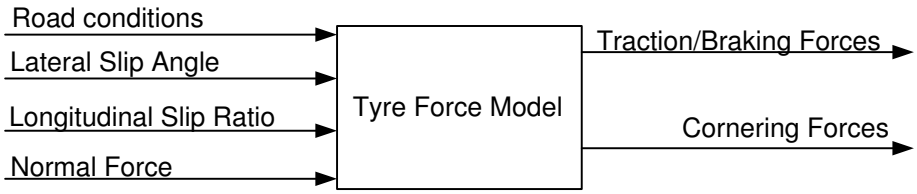

Figure 4.8: Tyre Force Model (Adapted from [43]).

One example of a lateral force model for tyres is the Segel Model [44] developed in the early 1970's. The model is simple to use and has the advantage of decreased computation time [44]. The lateral force predicted by the model is a function of the slip angle, cornering stiffness, tyre vertical load, friction coefficient and longitudinal force as described below in (4.6) -(4.11).

$$F_{\zeta i} = \mu F_{zi}(\tilde{\alpha}_i - \frac{\tilde{\alpha}_i \mid \tilde{\alpha}_i \mid}{3})\sqrt{(1 - \frac{{P_i}^2}{\mu^2 F_{zi}^2} + \frac{P_i^2}{c_i^2})} \qquad i = f, r \tag{4.6}$$

$$\tilde{\alpha}_i = \frac{c_i \alpha_i}{\mu F_{zi}} \qquad i = f, r \tag{4.7}$$

$$\alpha_f = \delta - \frac{a\dot{\Theta} + V_\zeta}{V_\eta} \tag{4.8}$$

$$\alpha_r = \frac{b\dot{\Theta} - V_\zeta}{V_\eta} \tag{4.9}$$

$$F_{zf} = \frac{mgb - (P_f + P_r)h}{a + b} \tag{4.10}$$

$$F_{zr} = \frac{mga + (P_f + P_r)h}{a + b} \tag{4.11}$$

where the model parameters are described in table 4.1.

Table 4.1: Parameters of Segel tyre model.

Parameter	Description
c_f, c_r	Cornering stiffness of front and rear tyres
F_{zf}, F_{zr}	Front and rear tyre vertical load
$F_{\zeta f}, F_{\zeta r}$	Lateral force on front and rear tyre
g	Gravitational acceleration
h	Height of centre of gravity
a	Front axle to centre of gravity distance
b	Rear axle to centre of gravity distance
m	Mass of Vehicle
μ	Friction coefficient
α_f, α_r	Slip angle of front and rear tyres
P_f, P_r	Longitudinal force on front and rear tyres
V_ζ, V_η	Longitudinal and lateral velocity in body reference frame
x, y	Longitudinal and lateral position in inertial reference frame
δ	Steering angle
Θ	Yaw angle
$\dot{\Theta}$	Yaw velocity

Unfortunately it is not possible to apply this model directly to an LHD vehicle due to its unique steering geometry and it is therefore necessary to use a different tyre model. The tyre model used in chapter 5 of this dissertation is however based loosely on the Segel Model and the comprehensive tyre model of [45] as all the tyre properties are not as yet available for LHD vehicle tyres and not all effects could be taken into account. However the effect of the cornering stiffness (C_α), which influences the path-tracking ability of the vehicle on a curved trajectory, is modelled. Figure 4.9 is a flowchart illustrating the operation of the comprehensive tyre model as described in [45].

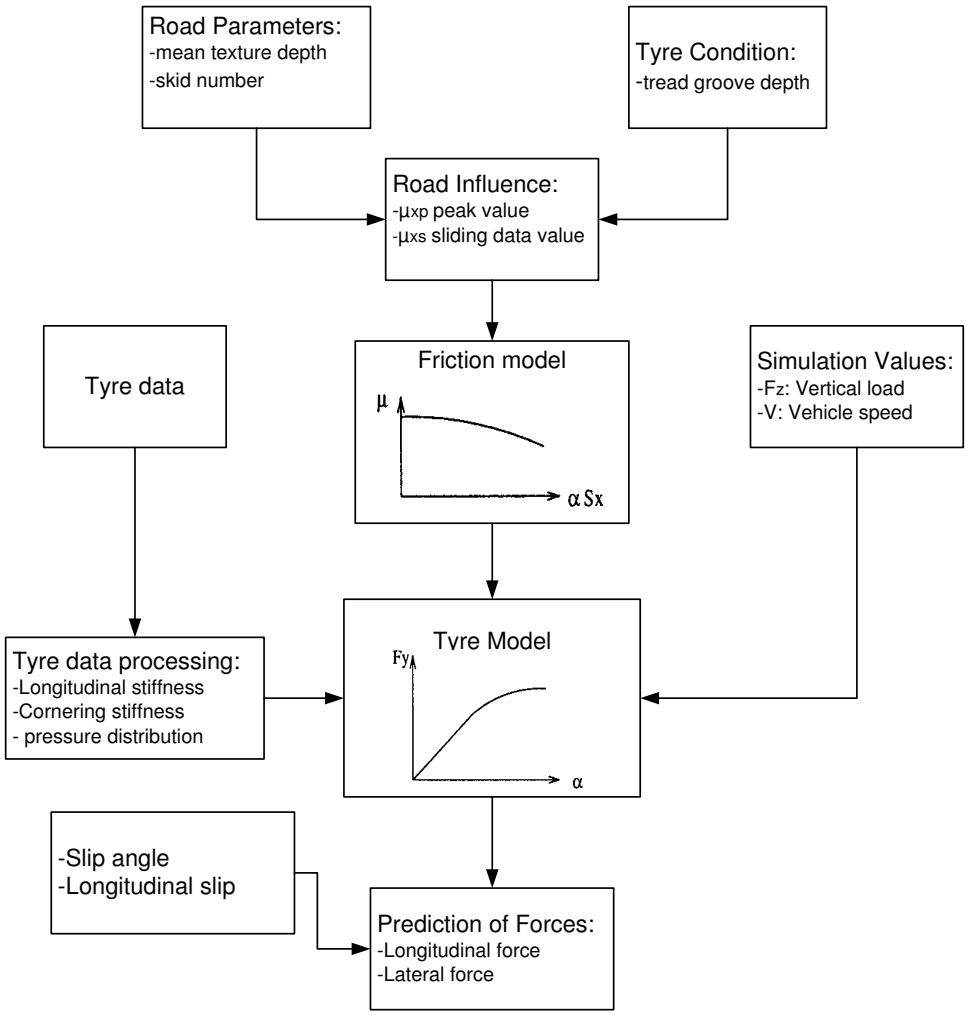

Figure 4.9: Flowchart of comprehensive tyre model (Adapted from [45]).

As indicated in figure 4.9 the comprehensive tyre model makes use of road parameters such as mean texture number and skid number together with the tread condition of the tyre to determine the peak and sliding friction coefficients of the tyre. This friction information is used for determining the longitudinal slip of the tyre. The tyre data consisting of the cornering and longitudinal stiffness together with the pressure distribution is used to obtain a model for the tyre relating lateral force to the slip angle of the tyre (α) for current vehicle speed and vertical load. It is then possible to use this model to predict the longitudinal and lateral forces generated by the tyre for that particular dynamic condition.

4.2.2.5 Longitudinal Force Modelling

The longitudinal forces on a vehicle's tyres can be determined from the acceleration of the vehicle by the following equation [42]:

$$(M + M_r)a_x = \frac{W + W_r}{g}a_x = \frac{\tau_e N_{tf}\ \ni_{tf}}{r} - R_x - D_A - W\sin(\theta) \tag{4.12}$$

where:

M = Mass of the vehicle = $\frac{W}{g}$

M_r = Equivalent mass of rotating components

a_x = Longitudinal acceleration

R_x = Rolling resistance force

D_A = Aerodynamic drag force

τ_e= Engine torque at given RPM

N_{tf} = combined ratio of the transmission and final drive

$\ni_{tf}$ = combined efficiency of the gearbox and final drive

r = radius of the tyre

θ = grade of road

Using equation (4.12) the longitudinal force for each tyre can be determined even if the vehicle drive train parameters are unknown based purely of the weight of the vehicle and the longitudinal acceleration as an approximation.

4.2.2.6 Rolling Resistance

The rolling resistance force in equation (4.12) is due to the fact that when a wheel rolls on a flat surface there is always deformation in both the road surface and the wheel. If the wheel and the road were both perfectly undeformable there would be no rolling resistance and therefore no need to exert a tractive force.
Perfectly rigid bodies do not exist and it is necessary that energy to be consumed in the deformation of the tyre/ road interface. This energy dissipation is the cause of rolling resistance, [39]. Rolling resistance increases with increasing deformation. A steel wheel on a steel rail has a lower rolling resistance than a pneumatic wheel on a compliant soil surface. For the case of a pneumatic tyre rolling on asphalt or concrete the deformations are contained almost entirely in the wheel and the energy dissipated in the tyre determines the rolling resistance. Other mechanisms such as small sliding between the road and the wheel, aerodynamic drag on the disc and friction in the hub of the wheel are responsible for a small contribution to the overall rolling resistance [38].
For practical purposes rolling resistance is usually expressed as

$$F_r = -fF_z \tag{4.13}$$

where F_z is the normal force and f is the rolling resistance coefficient which is usually determined experimentally. The coefficient f depends on a number of parameters such as the vehicle speed, the inflation pressure, the normal force (F_z), the tyre size, area of the contact patch, the tyre structure, the working temperature, the road conditions and the lateral and longitudinal forces (F_x and F_y) exerted by the tyre.
Due to the dependance on so many interrelated factors it is virtually impossible to develop a method of considering all these variables simultaneously. One simple estimate and the one used in this dissertation is based on a linear dependance on velocity as follows, [39]:

$$f = 0.01(1 + \frac{V}{100}) \tag{4.14}$$

There are several other more complex methods available to estimate the rolling resistance of a tyre, [39], [38], [46] but all require more detailed tyre information than is available for LHD vehicle tyres and therefore add little value to the estimate in terms of accuracy.

4.2.3 Dynamic Vehicle Models

The simplest vehicle dynamic model is the two-degree-of-freedom bicycle model representing the lateral and yaw motions. This modelling approach is also referred to as a single track model. The idea behind the modelling approach is that it is sometimes not

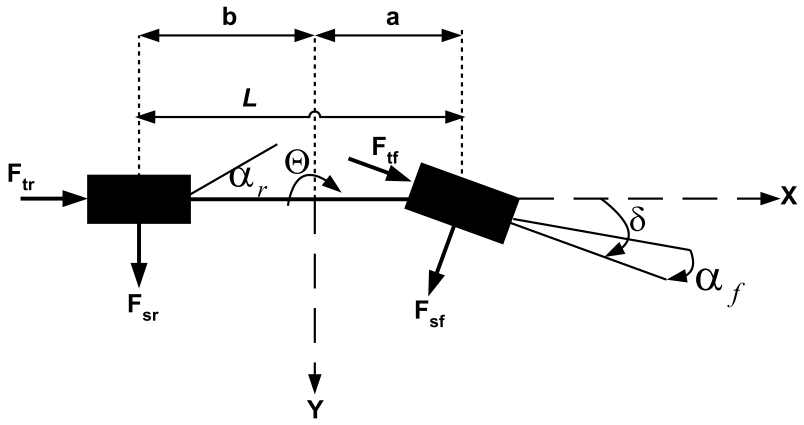

Figure 4.10: Schematic diagram illustrating the parameters of a two- and a three-degree-of-freedom bicycle model.

necessary to include the longitudinal direction as it does not affect the lateral or yaw stability of the vehicle [44].

A three-degree-of-freedom bicycle model adds longitudinal acceleration to the model. This allows the model to represent the vehicle motion in the entire X-Y plane. This model is simple to use and accounts for the tyre characteristics by lumping the two tyres on each axle together. This modelling technique has been used extensively to study the dynamics of motor vehicles (see for example [44]).

Figure 4.10 shows a schematic representation of the parameters represented in the two- and three-degree-of-freedom bicycle models. The descriptions of the various symbols used in the model are given in table 4.2.

In some cases the rotational degrees of freedom of the front and rear wheels are added to the model to allow for the inclusion of the effect of longitudinal slip of the tyres of the vehicle. This results in a five-degree-of-freedom model that enables the study of traction and braking forces on the handling of the vehicle including the effects of wheel spin, [44].

For the purposes of more detailed modelling for ride comfort analysis and suspension design, an eight-degree-of-freedom model, that no longer assumes dynamic symmetry between the left and right sides of the vehicle, can be developed. This is achieved by adding the rotational degrees of freedom for each of the four tyres instead of just two as in the five-degree-of-freedom model. An additional degree of freedom(ϕ) which considers the roll motion between the left and right sides of the vehicle makes up the remaining degree of freedom.

Table 4.2: Parameters of single-track dynamic vehicle models.

Symbol	Description
a	Distance between centre of mass and front axle
b	Distance between centre of mass and rear axle
l	wheelbase
δ	steering angle
α_f	slip angle of front tyre
α_r	slip angle of rear tyre
Θ	Yaw angle
ϕ	Roll angle
v	Component of velocity of C.G. in y direction
u	Component of velocity of C.G. in x direction
F_{tf}	Longitudinal force of front tyres
F_{sf}	Lateral force generated by front tyres
F_{tr}	Longitudinal force of rear tyres
F_{sr}	Lateral force generated by rear tyres

4.2.3.1 Cornering Equations for a single track model

Single-track or bicycle models are extremely useful for evaluating the cornering performance of a vehicle. The steady-state cornering equations for the model are derived by application of Newton's second law along with the turning geometry including the slip angles of the tyres,[38]. The cornering equations make use of simplifying assumptions such as small angle approximations which require that the turn radius be much larger than the wheelbase of the vehicle.

When a vehicle travelling at a forward speed V the sum of the forces in the lateral direction generated by the tyres of the vehicle must equal the mass of the vehicle times the centrifugal acceleration in order for the vehicle to maintain the desired trajectory.

$$\Sigma F_y = F_{sf} + F_{sr} = \frac{MV^2}{R} \tag{4.15}$$

where :

F_{sf} = Lateral force at the front axle

F_{sr} = Lateral force at the rear axle

M = Mass of the vehicle

V = Forward velocity of the vehicle

R = Radius of the turn

For the vehicle to be in moment equilibrium about the centre of gravity the sum of the moments caused by the front and rear lateral forces must be zero.

$$\begin{aligned} F_{sf}a - F_{sr}b &= 0 \\ F_{sf} &= F_{sr}\frac{b}{a} \end{aligned} \tag{4.16}$$

where a and b are as defined in figure 4.10.
Therefore substituting back into 4.16 results in:

$$\begin{aligned} \frac{MV^2}{R} = F_{sr}(\frac{b}{a}+1) &= \frac{F_{sr}(a+b)}{a} = \frac{F_{sr}L}{a}, \\ F_{sr} &= M\frac{a}{L}\frac{V^2}{R}. \end{aligned} \tag{4.17}$$

But $M\frac{a}{L}$ is simply the portion of the mass of the vehicle carried by the rear axle or $\frac{W_r}{g}$. The lateral force generated by the front axle can be solved for in the same manner.
After the lateral forces for the axles are known it is possible to calculate the slip angles at the front and rear wheels from $F_s = C_\alpha \alpha$ as follows:

$$\alpha_f = \frac{W_f V^2}{C_{\alpha f} g R} \tag{4.18}$$

$$\alpha_r = \frac{W_r V^2}{C_{\alpha r} g R} \tag{4.19}$$

Combining these equations yields the effective turning angle(δ) for the vehicle under the current cornering conditions as follows, [38]:

$$\delta = \frac{L}{R} + (\frac{W_f}{C_{\alpha f}} - \frac{W_r}{C_{\alpha r}})\frac{V^2}{gR} \tag{4.20}$$

where :

δ = Steering angle (rad)

L = wheelbase (meters)

M = Mass of the vehicle

V = Forward velocity of the vehicle

R = Radius of the turn

g = gravitational acceleration constant

W_f = Load on front axle (kg)

W_r = Load on rear axle (kg)

$C_{\alpha f}$ = Cornering stiffness of front tyres (N/rad)

$C_{\alpha r}$ = Cornering stiffness of rear tyres (N/rad)

4.2.3.2 Steering Gradient

The term $(\frac{W_f}{C_{\alpha f}} - \frac{W_r}{C_{\alpha r}})$ in equation 4.20 is referred to as the understeer gradient. The understeer gradient is an important parameter in the turning response properties of a vehicle. The parameter describes how the turning angle of the vehicle must be changed with the radius of the turn, R, or the lateral acceleration, $\frac{V^2}{gR}$ in order to remain on the desired curved trajectory. The understeer gradient consists of two terms each made up of the ratio of the axle load (front and rear) to the cornering stiffness of the tyres of each axle. This results in three possibilities:

Neutral Steer: $\frac{W_f}{C_{\alpha f}} = \frac{W_r}{C_{\alpha r}}$ and $\alpha_f = \alpha_r$.

In this case for a constant radius turn there is no change in steering input required as speed is varied to maintain the desired constant trajectory.

Understeer: $\frac{W_f}{C_{\alpha f}} > \frac{W_r}{C_{\alpha r}}$ and $\alpha_f > \alpha_r$.

In the case of understeer the steering angle will have to increase with changes in speed and lateral acceleration in order to maintain the same constant trajectory

Oversteer: $\frac{W_f}{C_{\alpha f}} < \frac{W_r}{C_{\alpha r}}$ and $\alpha_f < \alpha_r$.

In the case of oversteer the steering angle will have to decrease with increases in speed and lateral acceleration in order to maintain the same constant trajectory on a constant turn radius.

This characteristic of a vehicle will have an influence on the design of an autonomous vehicle controller as the understeer gradient will affect the vehicles path tracking capability at different speeds and loadings.

In the following chapter these and other modelling techniques are applied to the unique vehicle layout of the articulated steering LHD vehicle.

4.3 Chapter Summary

This chapter introduces the basic principles of vehicle modelling. Fundamental concepts such as the co-ordinate systems are defined as well as kinematic or low speed modelling is introduced. Tyre modelling concepts such as friction circles, rolling resistance and cornering stiffness are described and a basic single track model including dynamic tyre effects such as slip is shown for a car-like vehicle.

Chapter 5

Application of Vehicle Modelling Techniques to LHD Vehicles

There have been two main approaches in modelling the LHD vehicle. The first is derived from rigid body and rolling motion constraints. The second is based on the first but introduces the two slip variables which are chosen to represent the angle between the kinematically indicated velocity perpendicular to the vehicle axles and the true velocity of the vehicle. The former is commonly referred to as the no-slip model and the latter the slip model.
There has been some debate as to which model is required in order to implement an autonomous navigation system, [47], as the increased complexity of the slip model increases the computing power required on the actual vehicle in order to implement the navigation systems. The vehicle models presented here are those developed by [28]. There have however been other mathematical models developed [40] , that have however not been tested on the navigation of a physical mining vehicle as is the case with the work of [28].

5.1 Kinematic Model

Figure 5.1 shows the kinematic vehicle geometry used by [28] to derive their vehicle model. Equations (5.1) is the model derived by [28] from kinematics only.

$$\begin{aligned} \dot{x} &= V\cos\phi \\ \dot{y} &= V\sin\phi \\ \dot{\phi} &= \frac{V\tan(\frac{\gamma}{2})}{L} \end{aligned} \tag{5.1}$$

where x and y denote the position of the vehicle relative to some fixed global co-ordinate frame of reference, and L refers to the distance between the front and rear wheels of the vehicle and the articulation joint which is referred to as the half-length of the vehicle.

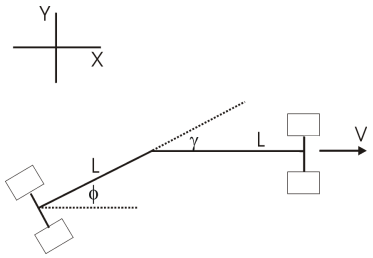

Figure 5.1: LHD kinematic geometry.

The angle ϕ is the orientation of the vehicle with respect to the x- axis also referred to as the heading and γ is defined as the articulation angle of the vehicle. These equations are based on the assumption that the front and rear wheel velocities of the LHD are identical and that the articulation angle remains constant.

5.2 Extended Kalman Filter Model

In order to take into account that the vehicle will slip during motion, [28] have introduced two slip variables, α and β as shown in figure 5.2. These variables represent the angle between the kinematically represented velocity, which is perpendicular to the axles and the true velocity and are therefore referred to as the slip angles. Any deviation between the true and kinematic velocities is by definition dependant on slip.
In deriving their model [28] reference all quantities to the rear of the vehicle; the position where the sensor array was located on their physical vehicle. As they consider the articulation angle to be an uncertain parameter in their model, this makes co-ordinate transforms from the front to rear of the vehicle a non-trivial task. In order to obtain the model they determine the velocity of P' in the direction perpendicular to V' and equate it to zero as shown in equation (5.2).

$$V\sin(\alpha-\beta-\gamma)+L\cos(\beta+\gamma)\phi+L\cos(\beta)(\phi+\gamma)=0 \tag{5.2}$$

And by solving for ϕ they obtain:

$$\dot{\phi}=\frac{V\sin(\alpha-\beta-\gamma)-\dot{\gamma}Lcos(\beta)}{L(\cos(\beta)+\cos(\beta+\gamma))} \tag{5.3}$$

By setting the velocity V of P equal to ωR, the wheels' angular velocity multiplied by the nominal wheel radius, and then resolved into its x and y components, the kinematic equations for point P are obtained as follows:

$$\begin{aligned}\dot{x}&=\omega R\cos(\alpha+\phi)\\ \dot{y}&=\omega R\sin(\alpha+\phi)\end{aligned} \tag{5.4}$$

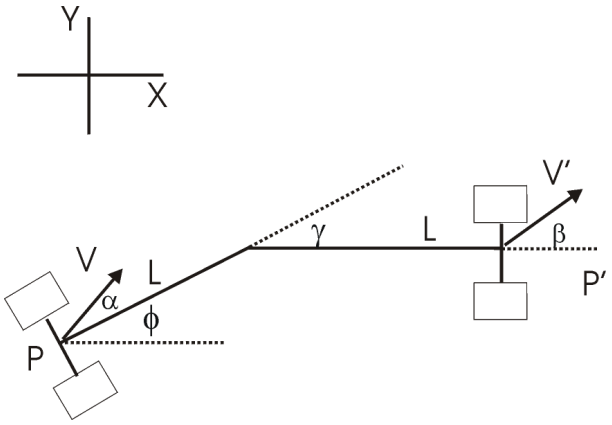

Figure 5.2: LHD kinematic geometry including slip angles.

From (5.4) it is evident that the vehicle moves in the direction given by the sum of the slip angles and the heading angle ϕ. The rate of change of the heading angle is dependant on the slip angles, as well as the articulation angle and the time derivative of the articulation angle.

5.2.1 Important Effects of Accounting for Slip

When comparing equations (5.1) and (5.4) it is evident that the two models are different. The simple model defined in equation (5.1) overestimates the turning rate of the vehicle. Equation (5.4) is far more accurate if the slip angles are known. However it is not possible to directly measure the slip angles and hence an Extended Kalman Filter (EKF) is used to estimate the unobservable states of the model. In order to use the EKF to estimate the states it is necessary to derive an error model for the system.

5.2.2 The Error Model

The main sources of error for the model given in equation (5.3) and equation (5.4) are due to the time varying parameters namely, ω, γ,$\dot{\gamma}$, α and β. Errors in these parameters propagate directly to the states, however the variables ω, γ and $\dot{\gamma}$ represent well known control inputs namely the angular velocity of the wheels, the articulation angle, and the rate of change of the articulation angle. It is therefore not required to estimate these parameters using the EKF.

It is necessary to estimate the slip parameters α and β as well as the effective wheel radius, R, of the vehicle, as, due to loading and wear, a typical LHD tyre may vary in radius by as much as 20cm, [28]. This can lead to excessive errors if a constant wheel radius is assumed for the entire life of the tyre.

Therefore the states that need to be estimated are the position, orientation, the slip angles as well as the wheel radius. The errors in the control inputs are modelled as additive noise $\delta\omega(t)$, $\delta\gamma(t)$ and $\delta\dot{\gamma}$ about the respective means.
The errors in R, α and β are however more difficult to model as they involve a combination of other parameters which are fundamentally dependant on vehicle dynamics, such as the slip angle changing with varying vehicle speed, mass as well as the tyre-terrain, in a non-linear manner. For this reason a compromise is used and the errors are modelled as random walks, or Brownian motion, in such a way that the errors are the integral of gaussian white noise.
The noise sources are assumed to be zero-mean, uncorrelated, gaussian sequences for the purposes of the design of the EKF. Although in practice these parameters may not evolve in a Brownian manner, the Brownian model reflects the growth in uncertainty in their true value and the rate at which their true value is expected to vary.
The continuous time vehicle model including the additional estimated states may now be written as follows:

$$\begin{aligned}
\dot{x}(t) &= \omega(t)R(t)\cos(\alpha(t)+\phi(t)) \\
\dot{y}(t) &= \omega(t)R(t)\sin(\alpha(t)+\phi(t)) \\
\dot{\phi}(t) &= \frac{\omega(t)R(t)\sin(\alpha(t)-\beta(t)-\gamma(t))-\dot{\gamma}(t)L\cos(\beta(t))}{L(\cos(\beta(t))+\cos(\beta(t)+\gamma(t)))} \\
\dot{R}(t) &= \delta R(t) \\
\dot{\alpha}(t) &= \delta\alpha(t) \\
\dot{\beta}(t) &= \delta\beta(t)
\end{aligned} \tag{5.5}$$

The particular observation model used, as well as the complete derivation of the EKF and the discrete time vehicle model, is available in [28].

5.3 Single-track Vehicle Model

This section describes the modelling of an LHD vehicle using a single-track or bicycle model approach. As described in the previous chapter this is an approach commonly used in modelling the cornering performance of a vehicle.
Figure 5.3 shows the schematic diagram of a single-track model applied to the steering geometry of an LHD vehicle in comparison to that of a car-like vehicle shown in figure 4.10. Table 5.1 provides the descriptions of the symbols used within the model.
The performance of the single-track vehicle model is governed by equation (4.20) as described in chapter 4. From equation (4.20) it is evident that the cornering performance is dependant on the weight on the front and rear axles of the vehicle. The weight carried by the front and rear axles in turn are dependant on the the parameters a and b which

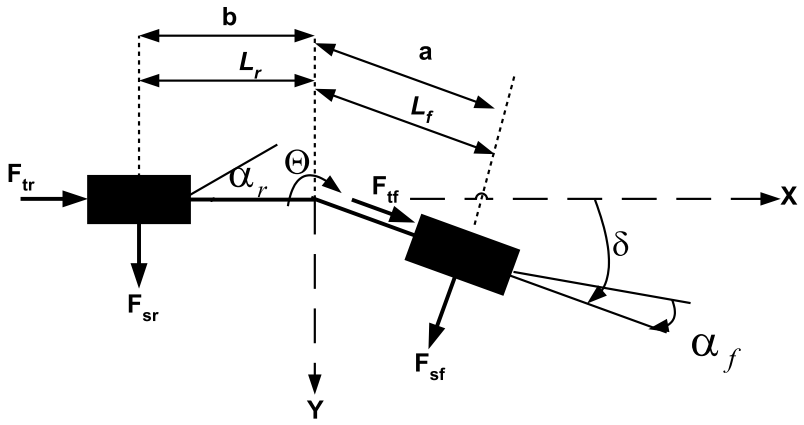

Figure 5.3: Schematic diagram of a single track or bicycle model for a vehicle with articulated steering such as an LHD.

Table 5.1: Parameters of single-track dynamic vehicle model for an articulated steering vehicle such as an LHD.

Symbol	Description
a	Distance between centre of mass and front axle
b	Distance between centre of mass and rear axle
l_f	distance between midpoint of front axle and articulation joint
l_r	distance between midpoint of rear axle and articulation joint
δ	articulation angle equivalent to the steering angle
α_f	slip angle of front tyre
α_r	slip angle of rear tyre
Θ	Yaw angle
ϕ	Roll angle
v	Component of velocity of C.G. in y direction
u	Component of velocity of C.G. in x direction
F_{tf}	Longitudinal force of front tyres
F_{sf}	Lateral force generated by front tyres
F_{tr}	Longitudinal force of rear tyres
F_{sr}	Lateral force generated by rear tyres

are the distances between the front and rear axle of the vehicle, respectively, and the centre of mass of the vehicle. This fact has an important effect on the performance of

an autonomous navigation and guidance controller for an LHD. The purpose of an LHD vehicle is to carry loads of ore in the underground mine tunnel. This in turn effects the weight distribution in the vehicle and has a marked influence of the vehicle's dynamic handling characteristics as will be shown in the simulations of chapter 7.

5.3.1 Centre of Gravity Calculations for an LHD

In this section the position of the centre of gravity for a Sandvik Tamrock EJC 245 LHD is calculated based on the vehicle axle loads as specified in [48] when the vehicle is loaded and unloaded. The calculations performed here will be used to perform the simulations of the single-track model in chapter 7.

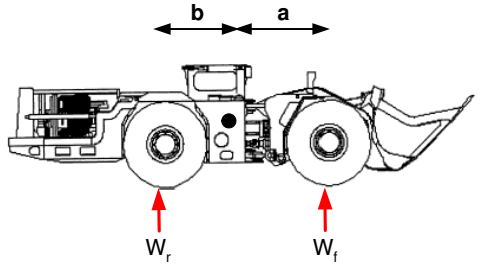

Figure 5.4: Illustration of parameters used to determine the location of the centre of gravity of the LHD.

In order to determine the location of the centre of gravity of the vehicle it is necessary to take moments about the articulation joint and sum them to zero. From there the values of a and b can be determined as shown below.

$$\begin{aligned} W_r b - W_f a &= 0 \\ \frac{b}{a} &= \frac{W_f}{W_r} \end{aligned} \tag{5.6}$$

In order for the vehicle to have a normal weight distribution it is assumed that the centre of gravity lies within the wheelbase (L) of the vehicle. Therefore a can be written as $L-b$ and by substituting this expression into (5.6) the value for a and b can be obtained from:

$$b = \frac{\frac{W_f}{W_r} L}{1 + \frac{W_f}{W_r}} \tag{5.7}$$

Using these equations and the vehicle loading parameters from [48] the following vehicle parameters can be obtained for the unloaded and fully loaded Sandvik Tamrock EJC 245 LHD.

Table 5.2: Unloaded LHD Vehicle Model Parameters.

Symbol	Value
W_f	10523 kg
W_r	15498 kg
a	2057 mm
b	1396 mm
l_f	1727 mm
l_r	1727 mm
l	3454 mm

Table 5.3: Loaded LHD Vehicle Model Parameters.

Symbol	Value
W_f	25859 kg
W_r	11204 kg
a	1044 mm
b	2409 mm
l_f	1727 mm
l_r	1727 mm
l	3454 mm

5.3.1.1 Understeer Gradient

Applying the equation for the understeer gradient (5.8) as described in chapter 4 to evaluate the vehicles cornering performance in terms of understeer gradient yields the following results for the unloaded and loaded LHD respectively. For the purposes of these calculations the cornering stiffness parameters of the tyres of a Ratel Military vehicle [49] were used as this is the vehicle with a tyre most like those used on an LHD vehicle for which the parameters are available.

$$\frac{W_f}{C_{\alpha f}} - \frac{W_r}{C_{\alpha r}} \tag{5.8}$$

Unloaded vehicle:

$C_{\alpha_f} = 4300$ N/deg

$C_{\alpha_r} = 5600$ N/deg

Understeer Gradient $= -0.160$

Therefore the vehicle will be prone to an oversteer characteristic when unloaded.

Note that the calculation of the understeer gradient is performed using twice the cornering stiffness parameter defined above as there are two tyres per axle.

Loaded vehicle:

$C_{\alpha_f} = 5600$ N/deg

$C_{\alpha_r} = 4300$ N/deg

Understeer Gradient = 0.925

Therefore the vehicle will be prone to an understeer characteristic when fully loaded.

For the purposes of these calculations the axle with the lightest load is assumed to have a lower cornering stiffness as cornering stiffness increases with vertical load on the axle. The calculations are of value only as an illustration as the values used are only a rough approximation to the cornering stiffness of the real LHD tyres. In order to have accurate results these characteristics would need to be measured for the actual LHD vehicle tyres. These calculations do however indicate the effect loading has on the handling characteristics of an LHD. Chapter 7 provides simulation results comparing the trajectories followed by the loaded and unloaded LHD vehicle single-track model to a pure kinematic model on a curvature of constant radius.

5.4 Complex Vehicle Model Derivation

This section details the derivation of a dynamic model for an LHD vehicle making use of Lagrangian dynamics. The same approach as described in [50] and [43] is followed .

5.4.1 The Coordinate System

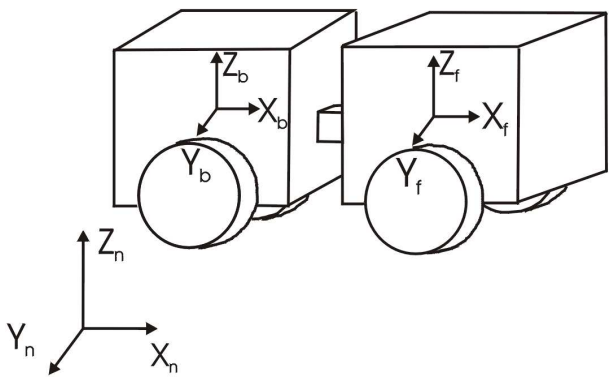

Figure 5.5: Coordinate system used in model derivation.

The coordinate system is defined to characterise the motion on an articulated LHD vehicle. As shown in figure 5.7, X_n, Y_n, Z_n is the fixed global coordinate system. In applying the

Lagrange method expressions for the kinetic and potential energies are obtained relative to this coordinate system. X_f, Y_f, Z_f are the coordinate system attached to the front unit of the LHD with Z_f positioned in such a way that it passes through the front unit's centre of gravity. Similarly X_r, Y_r, Z_r denote the position of the rear unit of the LHD vehicle. The motion of the front unit of the LHD can be described by the relative motion of the X_f, Y_f, Z_f coordinate system with respect to the X_n, Y_n, Z_n coordinate system. The motion of the rear unit of the vehicle can be characterised by describing the articulation angle between the front and rear units, or by describing the motion of the X_r, Y_r, Z_r coordinate system relative to the X_f, Y_f, Z_f coordinate system. Using this coordinate system a set of variables for the LHD vehicle can be introduced as follows:

x_n : position of the C.G. of the front unit in x-direction on inertial coordinates

$\dot{x_n}$: velocity of the C.G. of the front unit in x-direction on inertial coordinates

y_n : position of C.G. of the front unit in y-direction on inertial coordinates

$\dot{y_n}$: velocity of the C.G. of the front unit in y-direction on inertial coordinates

ϵ_1 : yaw angle of the front unit with respect to inertial coordinate system

$\dot{\epsilon_1}$: yaw rate of the front unit with respect to inertial coordinate system

ϵ_f : articulation angle between front and rear unit of vehicle

$\dot{\epsilon_f}$: rate of change of articulation angle between front and rear unit of vehicle

With the variables as defined above it is possible to determine the following transformation matrices between the different coordinate systems.
The transformation matrices between front unit coordinate system and inertial coordinate system are

$$\begin{pmatrix} \mathbf{i_n} \\ \mathbf{j_n} \\ \mathbf{k_n} \end{pmatrix} = \begin{pmatrix} \cos\epsilon_1 & -\sin\epsilon_1 & 0 \\ \sin\epsilon_1 & \cos\epsilon_1 & 0 \\ 0 & 0 & 1 \end{pmatrix} \begin{pmatrix} \mathbf{i_f} \\ \mathbf{j_f} \\ \mathbf{k_f} \end{pmatrix}, \tag{5.9}$$

and

$$\begin{pmatrix} \mathbf{i_f} \\ \mathbf{j_f} \\ \mathbf{k_f} \end{pmatrix} = \begin{pmatrix} \cos\epsilon_1 & \sin\epsilon_1 & 0 \\ -\sin\epsilon_1 & \cos\epsilon_1 & 0 \\ 0 & 0 & 1 \end{pmatrix} \begin{pmatrix} \mathbf{i_n} \\ \mathbf{j_n} \\ \mathbf{k_n} \end{pmatrix}, \tag{5.10}$$

The transformation matrices between front unit coordinate system and rear unit coordinate system:

$$\begin{pmatrix} \mathbf{i_r} \\ \mathbf{j_r} \\ \mathbf{k_r} \end{pmatrix} = \begin{pmatrix} \cos\epsilon_f & \sin\epsilon_f & 0 \\ -\sin\epsilon_f & \cos\epsilon_f & 0 \\ 0 & 0 & 1 \end{pmatrix} \begin{pmatrix} \mathbf{i_f} \\ \mathbf{j_f} \\ \mathbf{k_f} \end{pmatrix}, \tag{5.11}$$

and,

$$\begin{pmatrix} \mathbf{i_f} \\ \mathbf{j_f} \\ \mathbf{k_f} \end{pmatrix} = \begin{pmatrix} \cos\epsilon_f & -\sin\epsilon_f & 0 \\ \sin\epsilon_f & \cos\epsilon_f & 0 \\ 0 & 0 & 1 \end{pmatrix} \begin{pmatrix} \mathbf{i_r} \\ \mathbf{j_r} \\ \mathbf{k_r} \end{pmatrix}, \tag{5.12}$$

5.4.2 Model Derivation

In this section vehicle rotational and translational velocities will be determined for the front and rear units of the LHD vehicle. These will be used to derive the expressions for the kinetic and potential energies used to derive the model by applying Lagrange's equations.

Vehicle parameters as depicted in figure 5.6 and table 5.4

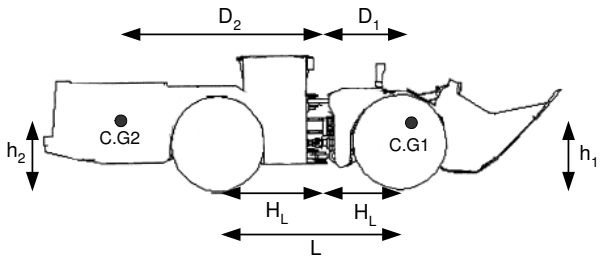

Figure 5.6: Schematic Diagram of vehicle parameters used in model derivation.

5.4.3 Vehicle Kinematics

5.4.3.1 Front Unit Kinematics

In order to calculate the translational velocity of the front unit of the LHD vehicle it is necessary to make use of several identities of time derivatives of unit vectors.

Firstly we note that the angular velocity of the front unit is

$$\omega_{f/n} = \dot{\epsilon_1}\mathbf{k_f} \tag{5.13}$$

therefore the derivatives of the unit vectors are:

Table 5.4: Parameters of vehicle model.

Parameter	Description
m_1	Mass of front unit
I_{x1}, I_{y1}, I_{z1}	Front unit's moments of inertia
m_2	Mass of rear unit
I_{x2}, I_{y2}, I_{z2}	Rear unit's moments of inertia
T_{w1}	Track width of front axle
T_{w2}	Track width of rear axle
$C_{\alpha f}$	Cornering stiffness of front tyre
$C_{\alpha r}$	Cornering stiffness of rear tyre
S_{xf}	Longitudinal stiffness of front tyre
S_{xr}	Longitudinal stiffness of rear tyre
H_L	Distance from midpoint of axle to articulation joint
L	Vehicle wheelbase
h_1, h_2	Height of centre of gravity (CG) of front and rear units
D_1, D_2	Distance from articulation joint to CG of front and rear units
d_1, d_2	Vertical distance from articulation joint to CG of front and rear units

$$\frac{d}{dt}\mathbf{i_f} = \omega_{f/n} \times \mathbf{i_f} = \dot{\epsilon_1}\mathbf{j_f} \tag{5.14}$$

$$\frac{d}{dt}\mathbf{j_f} = \omega_{f/n} \times \mathbf{j_f} = -\dot{\epsilon_1}\mathbf{i_f} \tag{5.15}$$

$$\frac{d}{dt}\mathbf{k_f} = \omega_{f/n} \times \mathbf{k_f} = 0 \tag{5.16}$$

5.4.3.2 Translational Velocity of Front Unit

Using these identities it is then possible to write the translational velocity of the centre of gravity of the front unit as follows by first expressing the position of the centre of gravity in the coordinate system.

$$r_{CG1/n} = r_{CG1/f} + rf/n = h_1\mathbf{k_f} + x_n\mathbf{i_n} + y_n\mathbf{j_n} \tag{5.17}$$

Differentiating (5.17) to obtain the velocity gives:

$$V_{CG1/n} = \dot{x_n}\mathbf{i_n} + \dot{y_n}\mathbf{j_n} + 0 = (\dot{x_n}\cos\epsilon_1 + \dot{y_n}\sin\epsilon_1)\mathbf{i_f} + (-\dot{x_n}\sin\epsilon_1 + \dot{y_n}\cos\epsilon_1)\mathbf{j_f} \tag{5.18}$$

5.4.3.3 Rear Unit Kinematics

The angular velocity of the rear unit coordinate system is:

$$\omega_{r/n} = \omega_{f/n} + \dot{\epsilon_f}\mathbf{k_r} \tag{5.19}$$
$$\omega_{r/n} = \dot{\epsilon_1}\mathbf{k_f} + \dot{\epsilon_f}\mathbf{k_r} \tag{5.20}$$
$$\omega_{r/n} = (\dot{\epsilon_1} + \dot{\epsilon_f})\mathbf{k_r} \tag{5.21}$$

therefore the derivatives of the unit vectors are:

$$\frac{d}{dt}\mathbf{i_r} = \omega_{r/n} \times \mathbf{i_r} = (\dot{\epsilon_1} + \dot{\epsilon_f})\mathbf{j_r} \tag{5.22}$$
$$\frac{d}{dt}\mathbf{j_r} = \omega_{r/n} \times \mathbf{j_r} = -(\dot{\epsilon_1} + \dot{\epsilon_f})\mathbf{i_r} \tag{5.23}$$
$$\frac{d}{dt}\mathbf{k_r} = \omega_{r/n} \times \mathbf{k_r} = 0 \tag{5.24}$$

5.4.3.4 Translational Velocity of Rear Unit

Using the same approach as for the front unit of the vehicle the translational velocity of the rear unit's centre of gravity can be found as:

$$r_{CG2/n} = r_{CG1/n} + r_{joint/CG1} + r_{CG2/joint}$$
$$r_{CG2/n} = r_{CG1/n} - D_1\mathbf{i_f} - d_1\mathbf{k_f} - D_2\mathbf{i_r} - d_2\mathbf{k_r} \tag{5.25}$$

Differentiating 5.25 to obtain the velocity gives:

$$V_{CG2/n} = V_{CG1/n} - D_1\frac{d}{dt}\mathbf{i_f} - d_1\frac{d}{dt}\mathbf{k_f} - D_2\frac{d}{dt}\mathbf{i_r} - d_2\frac{d}{dt}\mathbf{k_r}$$
$$V_{CG2/n} = V_{CG1/n} - D_1\epsilon_1\mathbf{j_f} - D_2(\dot{\epsilon_1} + \dot{\epsilon_f})\mathbf{j_r}$$
$$V_{CG2/n} = (\dot{x_n}\cos\epsilon_1 + \dot{y_n}\sin\epsilon_1)\mathbf{i_f} + (-\dot{x_n}\sin\epsilon_1 + \dot{y_n}\cos\epsilon_1 - D_1\epsilon_1)\mathbf{j_f} - D_2(\dot{\epsilon_1} + \dot{\epsilon_f})\mathbf{j_r} \tag{5.26}$$

5.4.4 Kinetic Energy

The kinetic energy of the LHD vehicle can be obtained by adding the kinetic energies of the front and rear components of the vehicle.
The kinetic energy of the front unit (T_1) of the vehicle can be calculated from it's translational and rotational velocity as show in 5.27.

$$T_1 = \frac{1}{2}m_1{V_{CG1}}^2 + \frac{1}{2}\omega_f I_1\omega_f$$
$$T_1 = \frac{1}{2}m_1(\dot{x_n}\cos\epsilon_1 + \dot{y_n}\sin\epsilon_1)^2 + \frac{1}{2}m_1(-\dot{x_n}\sin\epsilon_1 + \dot{y_n}\cos\epsilon_1)^2 + \frac{1}{2}I_{z1}{\dot{\epsilon_1}}^2 \tag{5.27}$$

similarly the kinetic energy of the rear unit (T_2) can be calculated as shown in 5.28.

$$\begin{aligned} T_2 &= \frac{1}{2}m_2{V_{CG2}}^2 + \frac{1}{2}\omega_r I_2 \omega_r \\ T_2 &= \frac{1}{2}m_2(\dot{x_n}\cos\epsilon_1 + \dot{y_n}\sin\epsilon_1)^2 + \frac{1}{2}m_2(-\dot{x_n}\sin\epsilon_1 + \dot{y_n}\cos\epsilon_1)^2 + \frac{1}{2}m_2(-D_1\dot{\epsilon_1} - D_2(\dot{\epsilon_1}+\dot{\epsilon_f}))^2 \\ &- m_2\sin\epsilon_f(\dot{x_n}\cos\epsilon_1 + \dot{y_n}\sin\epsilon_1).D_2(\dot{\epsilon_1}+\dot{\epsilon_f}) \\ &+ m_2\cos\epsilon_f(-\dot{x_n}\sin\epsilon_1 + \dot{y_n}\cos\epsilon_1 - D_1\dot{\epsilon_1}). - D_1(\dot{\epsilon_1}+\dot{\epsilon_f}) + \frac{1}{2}I_{z1}(\dot{\epsilon_1}+{\dot{\epsilon_f}}^2) \end{aligned} \tag{5.28}$$

5.4.5 Potential Energy

The change in potential energy of the vehicle would be caused mainly by roll motion in the vehicle suspension as detailed in [43]. However due to the limited amount of suspension travel and the heavy loads carried by an LHD vehicle it was decided to neglect the effects of roll motion for the purposes of this dissertation. Thus there is no change in potential energy.

$$V = 0. \tag{5.29}$$

5.4.6 Equations of Motion

In this section a set of four second order ordinary differential equations is derived which governs the motion of the vehicle in the inertial coordinate system, (X_n, Y_n, Z_n). The equations are derived by using Lagrange's equation.
After obtaining the kinetic and potential energy for the articulated LHD vehicle the Lagrangian for the system is defined as:

$$L = T_1 + T_2 - V. \tag{5.30}$$

By using Lagrange's Equation we obtain:

$$\frac{d}{dt}\frac{\partial L}{\partial \dot{x_n}} - \frac{\partial L}{\partial x_n} = F_{gx_n} \tag{5.31}$$

from which the first dynamic equation is obtained as follows:

$$\begin{aligned} &(m_1+m_2)\ddot{x_n} + m_2D_1\ddot{\epsilon_1}\sin\epsilon_1 - m_2D_1\dot{\epsilon_1}^2\cos\epsilon_1 \\ &-m_2D_2\ddot{\epsilon_1}\cos\epsilon_1\sin\epsilon_f + m_2D_2\dot{\epsilon_1}^2\sin\epsilon_1\sin\epsilon_f \\ &-m_2D_2\dot{\epsilon_1}\dot{\epsilon_f}\cos\epsilon_1\cos\epsilon_f - m_2D_2\ddot{\epsilon_f}\cos\epsilon_1\sin\epsilon_f \\ &+m_2D_2\dot{\epsilon_1}\dot{\epsilon_f}\sin\epsilon_1\sin\epsilon_f + m_2D_2\dot{\epsilon_f}^2\cos\epsilon_1\cos\epsilon_f \\ &+m_2D_1\ddot{\epsilon_1}1\cos\epsilon_f\sin\epsilon_1 - m_2D_2\dot{\epsilon_1}\dot{\epsilon_f}\sin\epsilon_f\sin\epsilon_1 \\ &+m_2D_1\dot{\epsilon_1}^2\cos\epsilon_1\cos\epsilon_f + m_2D_1\ddot{\epsilon_f}\sin\epsilon_f\cos\epsilon_f \\ &+m_2D_1\dot{\epsilon_f}^2\cos^2\epsilon_f - m_2D_1\dot{\epsilon_f}^2\sin^2\epsilon_f = F_{gx_n} \end{aligned} \tag{5.32}$$

where F_{gx_n} is the generalised force corresponding to the general coordinate X_n. By using Lagrange's Equation we obtain:

$$\frac{d}{dt}\frac{\partial L}{\partial \dot{y_n}} - \frac{\partial L}{\partial y_n} = F_{gy_n} \tag{5.33}$$

where F_{gy_n} is the generalised force corresponding to the general coordinate Y_n.
from which the second dynamic equation is obtained as follows:

$$\begin{gathered}(m_1+m_2)\ddot{y_n} - m_2 D_1 \ddot{\epsilon_1} cos\epsilon_1 + m_2 D_1 \dot{\epsilon_1^2} \sin\epsilon_1 \\ +m_2 D_2 \ddot{\epsilon_1} \cos\epsilon_1 \sin\epsilon_f - m_2 D_2 \dot{\epsilon_1^2} \sin\epsilon_1 \sin\epsilon_f \\ +m_2 D_2 \dot{\epsilon_1}\dot{\epsilon_f} \cos\epsilon_1 \cos\epsilon_f + m_2 D_2 \ddot{\epsilon_f} \cos\epsilon_1 \sin\epsilon_f \\ -m_2 D_2 \dot{\epsilon_1}\dot{\epsilon_f} \sin\epsilon_1 \sin\epsilon_f + m_2 D_2 \dot{\epsilon_f^2} \cos\epsilon_1 \cos\epsilon_f \\ -m_2 D_1 \ddot{\epsilon_1} 1 \cos\epsilon_f \cos\epsilon_1 + m_2 D_1 \dot{\epsilon_1^2} \sin\epsilon_1 cos\epsilon_f \\ +m_2 D_1 \dot{\epsilon_1}\dot{\epsilon_f} \cos\epsilon_1 \sin\epsilon_f = F_{gy_n}\end{gathered} \tag{5.34}$$

Continuing by using Lagrange's Equation we obtain:

$$\frac{d}{dt}\frac{\partial L}{\partial \dot{\epsilon_1}} - \frac{\partial L}{\partial \epsilon_1} = F_{g\epsilon_1} \tag{5.35}$$

where $F_{g\epsilon_1}$ is the generalised force corresponding to the general coordinate ϵ_1 from which the third dynamic equation is obtained as follows:

$$\begin{gathered}I_{z_1}\ddot{\epsilon_1} + m_2(D_1+D_2)\dot{\epsilon_1} + m_2 D_1 \ddot{x_n} \sin\epsilon_1 - 2m_2 D_1 \dot{\epsilon_1}\dot{x_n} \cos\epsilon_1 \\ -m_2 D_1 \ddot{y_n} \cos\epsilon_1 + m_2 D_2^2 \ddot{\epsilon_f} - m_2 D_2 \ddot{x_n} \cos\epsilon_1 \sin\epsilon_f - m_2 D_2 \dot{x_n}\dot{\epsilon_f} \cos\epsilon_1 \cos\epsilon_f \\ +m_2 D_2 \ddot{y_n} \sin\epsilon_f \sin\epsilon_1 + m_2 D_2 \dot{y_n}\dot{\epsilon_f} \cos\epsilon_f \sin\epsilon_1 - m_2 D_2 \ddot{y_n} \cos\epsilon_1 \cos\epsilon_f \\ +m_2 D_2 \dot{y_n}\dot{\epsilon_1} \sin\epsilon_1 \cos\epsilon_f - m_2 D_1 \ddot{y_n} \cos\epsilon_1 \cos\epsilon_f + m_2 D_1 \dot{y_n}\dot{\epsilon_f} \cos\epsilon_1 \sin\epsilon_f \\ +m_2 D_1 \ddot{x_n} \cos\epsilon_f \sin\epsilon_1 - m_2 D_1 \dot{x_n}\dot{\epsilon_f} \sin\epsilon_f \sin\epsilon_1 + 2m_2 D_1^2 \ddot{\epsilon_1} \cos\epsilon_f \\ -2m_2 D_1^2 \dot{\epsilon_1}\dot{\epsilon_f} \sin\epsilon_f + m_2 D_1^2 \ddot{\epsilon_f} \cos\epsilon_f - m_2 D_1^2 \dot{\epsilon_f^2} \sin\epsilon_f \\ +I_{z_2}\ddot{\epsilon_1} + \tfrac{1}{2} I_{z_2}\ddot{\epsilon_f} - m_2 D_2 \dot{x_n}\dot{\epsilon_f} \sin\epsilon_1 \sin\epsilon_f - m_2 D_1 \dot{y_n}\dot{\epsilon_f} \sin\epsilon_1 \cos\epsilon_f = F_{g\epsilon_1}\end{gathered} \tag{5.36}$$

Finally again using Lagrange's Equation gives:

$$\frac{d}{dt}\frac{\partial L}{\partial \dot{\epsilon_f}} - \frac{\partial L}{\partial \epsilon_f} = F_{g\epsilon_f} \tag{5.37}$$

where $F_{g\epsilon_f}$ is the generalised force corresponding to the general coordinate ϵ_f

resulting in the fourth and final dynamic equation:

$$\begin{aligned}
&m_2D_2^2(\ddot{\epsilon_1}+\ddot{\epsilon_f}) - m_2D_2\ddot{x_n}\cos\epsilon_1\sin\epsilon_f + m_2D_2\dot{x_n}\dot{\epsilon_1}\sin\epsilon_1\sin\epsilon_f \\
&+m_2D_2\ddot{y_n}\sin\epsilon_f\sin\epsilon_1 + m_2D_2\dot{y_n}\sin\epsilon_f\cos\epsilon_1 - m_2D_1\ddot{y_n}\cos\epsilon_1\cos\epsilon_f \\
&m_2D_1\dot{y_n}\dot{\epsilon_1}\sin\epsilon_1\cos\epsilon_f + m_2D_1\dot{y_n}\dot{\epsilon_f}\cos\epsilon_1\sin\epsilon_f + m_2D_1\ddot{x_n}\sin\epsilon_f\cos\epsilon_f \\
&+m_2D_1^2\ddot{\epsilon_1}\cos\epsilon_f + I_{z_2}\ddot{\epsilon_f} + \tfrac{1}{2}I_{z_2}\ddot{\epsilon_1} + m_2D_2\dot{x_n}\dot{\epsilon_1}\cos\epsilon_1\cos\epsilon_f \\
&-m_2D_2\dot{y_n}\dot{\epsilon_1}\cos\epsilon_f\sin\epsilon_1 - m_2D_1\dot{y_n}(\ddot{\epsilon_1}+\dot{\epsilon_f})\sin\epsilon_f\cos\epsilon_1 \\
&+m_2D_1\dot{\epsilon_1}\dot{x_n}\sin\epsilon_f\sin\epsilon_1 + m_2D_1^2\dot{\epsilon_1}^2\sin\epsilon_f = F_{g\epsilon_f}
\end{aligned} \tag{5.38}$$

The four dynamic equations form the first part of the complex vehicle model.

5.4.7 Generalised Forces

As can be seen from the right hand side of equations (5.32), (5.34),(5.36) and (5.38), the generalised forces are an important part of the model. In this section the generalised forces are derived. The external forces acting on the vehicle would consist of the tyre/road interface. In order to calculate the generalised forces, expressions for the generalised forces are derived in terms of longitudinal and lateral components of the tyre forces. The process for deriving the generalised forces is based on the principle of virtual work [43].
To derive the expressions for the generalised forces the following sign conventions are defined as shown in figure 5.7, where F_{ai} and F_{bi} refers to the longitudinal and lateral force of the tyre respectively.

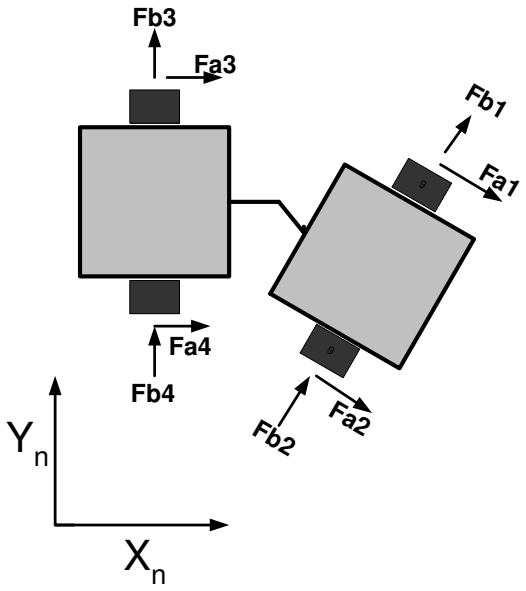

Figure 5.7: Definition of tyre forces in Cartesian Coordinates.

From figure 5.7 the component of the tyre force along the x-axis is:

$$F_{x_n i} = F_{ai}\cos\epsilon_1 - F_{bi}\sin\epsilon_1 \qquad for \quad i = 1,2 \tag{5.39}$$

$$F_{x_n i} = F_{ai}\cos(\epsilon_1 + \epsilon_f) - F_{bi}\sin(\epsilon_1 + \epsilon_f) \qquad for \quad i = 3,4 \tag{5.40}$$

From figure 5.7 the component of the tyre force along the y-axis is:

$$F_{y_n i} = F_{ai}\sin\epsilon_1 - F_{bi}\cos\epsilon_1 \qquad for \quad i = 1,2 \tag{5.41}$$

$$F_{y_n i} = F_{ai}\sin(\epsilon_1 + \epsilon_f) - F_{bi}\cos(\epsilon_1 + \epsilon_f) \qquad for \quad i = 3,4 \tag{5.42}$$

The position vectors where the external forces are acting on each tyre can be obtained as follows :

$$\begin{aligned} r_{t1} &= r_{CG} + L_1\mathbf{i_f} + \frac{T_{w1}}{2}\mathbf{j_f} - z_0\mathbf{k_f} \\ r_{t1} &= x_n\mathbf{i_n} + y_n\mathbf{j_n} + z_0\mathbf{k_n} + L_1\mathbf{i_f} + \frac{T_{w1}}{2}\mathbf{j_f} - z_0\mathbf{k_f} \end{aligned} \tag{5.43}$$

where, as described in table 5.4,

L_1 : distance from centre of wheel to CG

T_w1 : Front axle track width

Z_0 : height of the centre of gravity

By substituting the transformation matrices the following is obtained:

$$\begin{aligned} r_{t1} = \quad & (x_n + L_1\cos\epsilon_1 - \tfrac{T_{w1}}{2}\sin\epsilon_1)\mathbf{i_n} \\ & +(y_n + L_1\sin\epsilon_1 + \tfrac{T_{w1}}{2}\cos\epsilon_1)\mathbf{j_n} \\ & +0\mathbf{k_n} \\ r_{t1} = \quad & r_{xt1}\mathbf{i_n} + r_{yt1}\mathbf{y_n} + r_{zt1}\mathbf{k_n} \end{aligned} \tag{5.44}$$

Similarly

$$\begin{aligned} r_{t2} = \quad & r_{CG1} + L_1\mathbf{i_f} - \tfrac{T_{w1}}{2}\mathbf{j_f} - z_0\mathbf{k_f} \\ r_{t2} = \quad & (x_n + L_1\cos\epsilon_1 + \tfrac{T_{w1}}{2}\sin\epsilon_1)\mathbf{i_n} \\ & +(y_n + L_1\sin\epsilon_1 - \tfrac{T_{w1}}{2}\cos\epsilon_1)\mathbf{j_n} \\ & +0\mathbf{k_n} \\ r_{t2} = \quad & r_{xt2}\mathbf{i_n} + r_{yt2}\mathbf{y_n} + r_{zt2}\mathbf{k_n} \end{aligned} \tag{5.45}$$

$$
\begin{aligned}
r_{t3} = \quad & r_{CG1} - D_1\mathbf{i_f} - H_2\mathbf{i_r} + \tfrac{T_{w3}}{2}\mathbf{j_r} - z_0\mathbf{k_r} \\
r_{t3} = \quad & x_n\mathbf{i_n} + y_n\mathbf{j_n} + z_0\mathbf{k_n} - D_1\mathbf{i_f} - H_2\mathbf{i_r} + \tfrac{T_{w3}}{2}\mathbf{j_r} - z_0\mathbf{k_r} \\
r_{t3} = \quad & (x_n - (d_1 + H_L\cos\epsilon_f + \tfrac{T_{w3}}{2}\sin\epsilon_f)\cos\epsilon_1 - (-H_L\sin\epsilon_f + \tfrac{T_{w3}}{2}\cos\epsilon_f)\sin\epsilon_1)\mathbf{i_n} \\
& +(y_n - (d_1 + H_L\cos\epsilon_f + \tfrac{T_{w3}}{2}\sin\epsilon_f)\sin\epsilon_1 + (-H_L\sin\epsilon_f + \tfrac{T_{w3}}{2}\cos\epsilon_f)\cos\epsilon_1)\mathbf{j_n} \\
& +0\mathbf{k_n} \qquad (5.46) \\
r_{t3} = \quad & r_{xt3}\mathbf{i_n} + r_{yt3}\mathbf{y_n} + r_{zt3}\mathbf{k_n}
\end{aligned}
$$

$$
\begin{aligned}
r_{t4} = \quad & r_{CG1} - D_1\mathbf{i_f} - H_L\mathbf{i_r} + \tfrac{T_{w3}}{2}\mathbf{j_r} - z_0\mathbf{k_r} \\
r_{t4} = \quad & x_n\mathbf{i_n} + y_n\mathbf{j_n} + z_0\mathbf{k_n} - D_1\mathbf{i_f} - H_L\mathbf{i_r} - \tfrac{T_{w3}}{2}\mathbf{j_r} - z_0\mathbf{k_r} \\
r_{t4} = \quad & (x_n - (d_1 + H_L\cos\epsilon_f - \tfrac{T_{w3}}{2}\sin\epsilon_f)\cos\epsilon_1 - (-H_L\sin\epsilon_f - \tfrac{T_{w3}}{2}\cos\epsilon_f)\sin\epsilon_1)\mathbf{i_n} \\
& +(y_n - (d_1 + H_L\cos\epsilon_f - \tfrac{T_{w3}}{2}\sin\epsilon_f)\sin\epsilon_1 + (-H_L\sin\epsilon_f - \tfrac{T_{w3}}{2}\cos\epsilon_f)\cos\epsilon_1)\mathbf{j_n} \\
& +0\mathbf{k_n} \qquad (5.47) \\
r_{t4} = \quad & r_{xt4}\mathbf{i_n} + r_{yt4}\mathbf{y_n} + r_{zt4}\mathbf{k_n}
\end{aligned}
$$

Equations (5.44), (5.45), (5.46) and (5.47) are the position vectors of the external forces. The generalised force F_{gx_n} is:

$$F_{gx_n} = \sum_{i=1}^{4} F_{x_n i}\frac{\partial r_{xti}}{\partial x_n} + \sum_{i=1}^{4} F_{y_n i}\frac{\partial r_{yti}}{\partial x_n} \qquad (5.48)$$

Substituting (5.44), (5.45), (5.46) and (5.47) into (5.48) gives:

$$F_{gx_n} = F_{x_n 1} + F_{x_n 2} + F_{x_n 3} + F_{x_n 4} \qquad (5.49)$$

Similarly the generalised for associated with the y-coordinate is given by:

$$F_{gy_n} = F_{y_n 1} + F_{y_n 2} + F_{y_n 3} + F_{y_n 4} \qquad (5.50)$$

The generalised force associated with the ϵ_1 coordinate is:

$$F_{g\epsilon_1} = \sum_{i=1}^{4} F_{x_n i}\frac{\partial r_{xti}}{\partial \epsilon_1} + \sum_{i=1}^{4} F_{y_n i}\frac{\partial r_{yti}}{\partial \epsilon_1} \qquad (5.51)$$

which can be written as

$$\begin{aligned}
F_{g\epsilon_1} = \quad & -F_{a_1}L_1\sin\epsilon_1 - F_{a_1}\tfrac{T_{w1}}{2}\cos\epsilon_1 - F_{a_2}L_1\sin\epsilon_1 + F_{a_2}\tfrac{T_{w1}}{2}\cos\epsilon_1 \\
& + F_{a_3}(d_1 + H_L\cos\epsilon_f + \tfrac{T_{w3}}{2}\sin\epsilon_f)\sin\epsilon_1 - F_{a_3}(-H_L\sin\epsilon_f + \tfrac{T_{w3}}{2}\cos\epsilon_f)\cos\epsilon_1 \\
& + F_{a_4}(d_1 + H_L\cos\epsilon_f - \tfrac{T_{w3}}{2}\sin\epsilon_f)\sin\epsilon_1 - F_{a_4}(-H_L\sin\epsilon_f - \tfrac{T_{w3}}{2}\cos\epsilon_f)\cos\epsilon_1 \\
& + F_{b_1}L_1\cos\epsilon_1 - F_{b_1}\tfrac{T_{w1}}{2}\sin\epsilon_1 + F_{b_2}L_1\cos\epsilon_1 + F_{b_2}\tfrac{T_{w1}}{2}\sin\epsilon_1 \\
& - F_{b_3}(d_1 + H_L\cos\epsilon_f + \tfrac{T_{w3}}{2}\sin\epsilon_f)\cos\epsilon_1 - F_{b_3}(-H_L\sin\epsilon_f + \tfrac{T_{w3}}{2}\cos\epsilon_f)\sin\epsilon_1 \\
& - F_{b_4}(d_1 + H_L\cos\epsilon_f - \tfrac{T_{w3}}{2}\sin\epsilon_f)\cos\epsilon_1 - F_{b_4}(-H_L\sin\epsilon_f - \tfrac{T_{w3}}{2}\cos\epsilon_f)\sin\epsilon_1
\end{aligned} \tag{5.52}$$

The generalised force associated with the ϵ_f coordinate is:

$$F_{g\epsilon_f} = \sum_{i=1}^{4} F_{x_n i}\frac{\partial r_{xti}}{\partial \epsilon_f} + \sum_{i=1}^{4} F_{y_n i}\frac{\partial r_{yti}}{\partial \epsilon_f} \tag{5.53}$$

which can be written as

$$\begin{aligned}
F_{g\epsilon_f} = \quad & -F_{a_3}H_L\cos\epsilon_1\sin\epsilon_f + F_{a_3}\tfrac{T_{w3}}{2}\cos\epsilon_1\cos\epsilon_f + F_{a_3}H_L\cos\epsilon_f\sin\epsilon_1 - F_{a_3}\tfrac{T_{w3}}{2}\sin\epsilon_f\sin\epsilon_1 \\
& - F_{a_4}H_L\cos\epsilon_f\sin\epsilon_1 + + F_{a_4}\tfrac{T_{w3}}{2}\cos\epsilon_1\cos\epsilon_f + F_{a_4}H_L\sin\epsilon_1\cos\epsilon_f - F_{a_4}\tfrac{T_{w3}}{2}\sin\epsilon_f\sin\epsilon_1 \\
& + F_{b_3}H_L\cos\epsilon_f\cos\epsilon_1 - F_{b_3}\tfrac{T_{w3}}{2}\sin\epsilon_f\cos\epsilon_1 - F_{b_3}H_L\sin\epsilon_f\sin\epsilon_1 + F_{b_3}\tfrac{T_{w3}}{2}\cos\epsilon_f\sin\epsilon_1 \\
& - F_{b_4}H_L\sin\epsilon_f\sin\epsilon_1 + F_{b_4}H_L\tfrac{T_{w3}}{2}cos\epsilon_f sin\epsilon_1 \\
& - F_{b_4}H_L\cos\epsilon_f\cos\epsilon_1 + F_{b_4}\tfrac{T_{w3}}{2}\cos\epsilon_1\sin\epsilon_f
\end{aligned} \tag{5.54}$$

The generalised forces are the second component of the complex vehicle model.

5.4.8 Subsystems: Tyre and Suspension Model

5.4.8.1 Tyre Model

The tyre model used in the complex vehicle model simulation is a simplified adaptation of that developed in [45] and described in section 4.2.2.4.

The basic principles behind the tyre model are outlined in the flowchart of figure 5.8, also given in chapter 4, repeated here for convenience. The tyre model block on the flowchart represents the tyre lateral force generated as a function of slip angle α. As these characteristics were not available for an LHD tyre, the data for a Ratel Military vehicle [49] tyre was used as an approximation as this data were available.

The simplified tyre model used in the complex vehicle model makes use of the vehicle's current dynamic simulation values to ultimately determine the slip angles (α) of the tyres under a dynamic load condition. This is achieved by making use of the simulation values to determine the longitudinal force (F_x) and lateral force (F_y) on the vehicle. The model

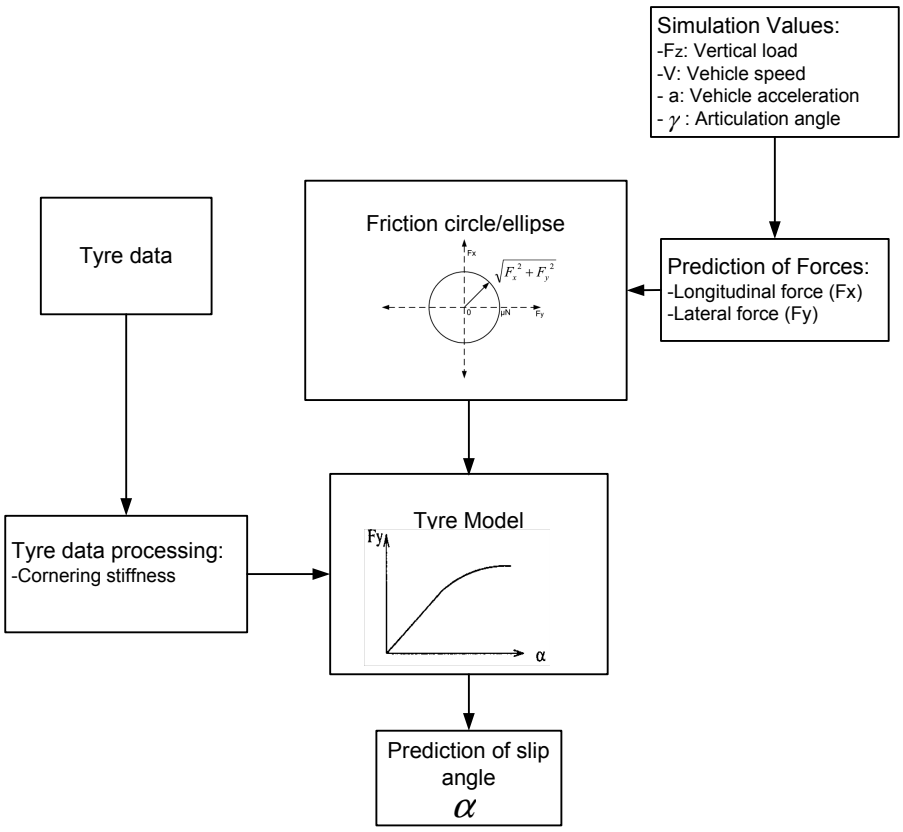

Figure 5.8: Flowchart of simplified comprehensive tyre model.

then verifies that the predicted longitudinal and lateral forces are within the traction limit of the tyres as defined by the friction circle/ellipse concept described in section 4.2.2.2 of chapter 4. In the event that the forces should exceed the maximum specified by the friction circle it would mean that the vehicle is skidding and not subject to normal rolling motion. The lateral force (F_y) together with the vehicle's tyre data, consisting of the side forces versus slip angle relationship, are then used to predict the slip angle of the tyre under this particular dynamic vehicle load condition. This predicted value of the slip angle of the tyres (α) is then used in the calculation of the vehicles trajectory to improve

the accuracy of the trajectory predicted by the vehicle model.
The side forces versus slip angle information used in the simplified tyre model is based on the tyre data and characteristics of a Ratel military vehicle. Figures 5.9 and 5.10 show the side force versus slip angle graph for a Ratel tyre and a vertical load of 2 tonnes and 4 tonnes respectively.

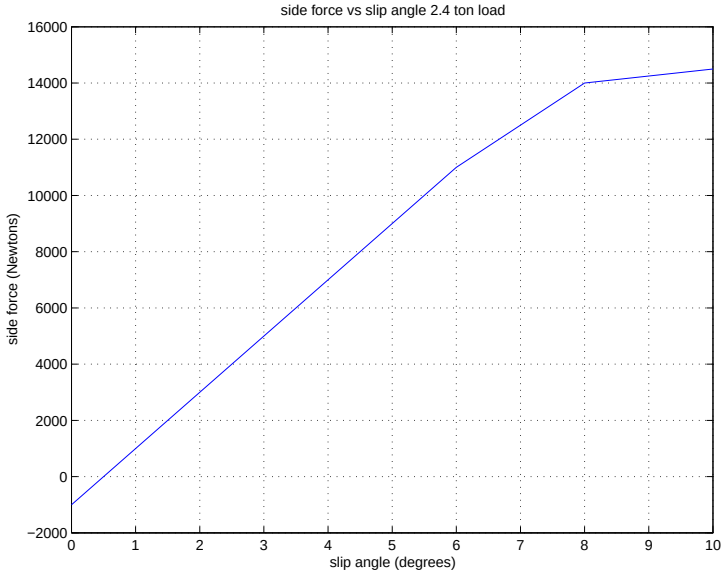

Figure 5.9: Plot of side force versus slip angle α for Ratel tyre with 2 tonnes of vertical loading.

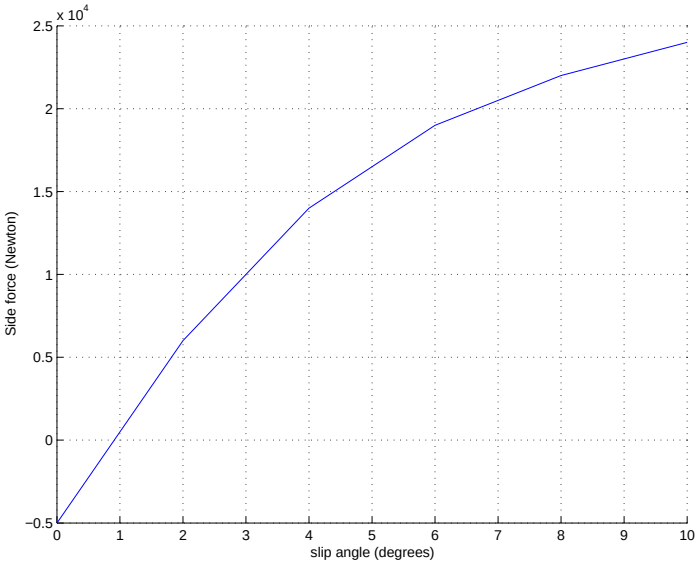

Figure 5.10: Plot of side force versus slip angle α for Ratel tyre with 4 tonnes of vertical loading.

As can be seen there is a marked difference between the tyre characteristics due to the different vertical load conditions. The accuracy of the simulation results are therefore highly dependant on the accuracy of the assumed tyre characteristics. The Ratel tyre data is only a rough approximation to that of an actual LHD vehicle as the Ratel vehicle is significantly lighter than an LHD. The vehicle's tyres are also slightly smaller than that of an LHD however the information is suitable to be used as a first approach in developing a model as there is no tyre data available on actual LHD vehicle tyres. A Ratel tyre is a 16×20 tyre, which means the tyre is 16 inches wide and fits onto a rim with a 20 inch diameter. This is slightly smaller than the tyre used in the EJC 245 LHD which is a 18×25 tyre, [48].

5.4.8.2 Suspension Model

The present complex vehicle model does not take into account the effects of the vehicles suspension. Due to the heavy loads an LHD vehicle normally carries the suspension is extremely stiffly sprung and therefore assumed to have minimal effect on the vehicle handling characteristics. There is also no detailed information available on the LHD vehicle suspension design and characteristics. It is therefore not useful to model the vehicle's suspension.
In order to include the effects that suspension would have on the vehicle model in possible future work, a further degree of freedom, namely that of roll motion, can be introduced into the Lagrangian derivation of the vehicle model. Alternatively the effects of suspension can be included in the vehicle by changing the positions of the centres of gravity of the two halves of the vehicle so as to represent compression and extension of the suspension.

5.5 Chapter Summary

In this chapter the vehicle modelling techniques discussed in chapter 4 are applied to the unique steering geometry of an LHD vehicle. Three LHD vehicle models are presented the first being an extended Kalman filter (EKF) model, the second a single-track vehicle model adapted to the LHD steering geometry and the final model being a model derived based on Lagrangian dynamics.

Chapter 6

Model Validation

This chapter describes how the tyre parameters used in the vehicle model of chapter 5 can be experimentally measured. The equipment needed to perform the experiments to validate the vehicle model is also described.
Only a theoretical description of the model validation process is provided as the costs of removing an expensive LHD vehicle from service to perform these experiments is prohibitive.

6.1 Tyre Parameter Validation

In order to determine the tyre parameters as used in the vehicle model of chapter 4 and 5, namely the lateral slip angle (α) which is dependant on the cornering stiffness (C_α) of the tyre, it is necessary to perform physical measurements on an LHD tyre. To determine C_α it is necessary to perform the side force versus slip angle measurement which is carried out on specialised equipment.

6.1.1 Equipment used

The equipment used to perform this experiment is available at the Gerotek vehicle testing centre west of Pretoria. Gerotek has the expertise and facilities available to accurately measure tyre contact area and forces on tyre diameters ranging from 1 m to 1.7 m under load conditions of up to 100 kN [51].

6.2 Vehicle Model Validation

In order to validate the vehicle model derived in this dissertation there are two approaches which can be followed. The first approach is to compare the simulation results to a known

source as done in [44]. This however is not possible as there is no other validated LHD vehicle model available at present. The second and more realistic approach is to perform physical experiments on a vehicle and track the vehicle's trajectory for known control inputs by means of global positioning system (GPS). The results can then be compared to the simulation output for the same control inputs. Any necessary model tuning can then be performed to improve the correlation between the predicted model output and the measured results. The equipment used to perform this method of validation and the experimental design are described in the next sections.

6.2.1 Equipment used

In order to perform the physical test on an LHD vehicle to validate the model, the VBOX II DGPS system would be used, [52]. The system makes use of differential global positioning system (DGPS) signals to perform detailed analysis of a vehicle's braking, accelerating and handling characteristics.

6.2.1.1 Differential GPS

Differential GPS or DGPS makes use of a third party source to correct for absolute positioning errors. The VBOX is designed to pick up differential corrections using the Wide Area Augmentation system (WAAS), which is a free satellite based system with a number of extra satellites specifically set up to improve the accuracy of GPS measurements, [52]. A number of land based stations constantly broadcast corrections to this range of satellites which in turn are re-transmitted by the satellites on the same frequency as GPS and picked up on the same GPS antenna of the VBOX system. DGPS is only capable of correcting the absolute position error and has no effect on the velocity or relative distance measurements.

6.2.1.2 VBOX System Overview

The VBOX system is capable of measuring the following parameters without additional instrumentation:

- Velocity
- Distance
- Time
- Position

- Heading
- Lateral acceleration
- Longitudinal acceleration
- Vertical velocity
- Radius of turn

The VBOX contains a high speed GPS engine which is capable of measuring the three dimensional position and speed of the receiver, attached to the vehicle, 20 times a second. In order for the VBOX system to provide the most accurate measurements of the vehicles position it should be operated in relative measurement mode [52]. In this mode the system measures distance relative to two measurement points. The VBOX then integrates the velocity signal to obtain the distance relative to the starting point. Distances measured in this manner are typically accurate to within a couple of centimetres as they are based on the doppler shift velocity values, [52].

6.2.2 Experiment Design

An important property of a vehicle's turning response characteristics is the understeer gradient (K). As detailed in chapter 4 this property determines how the steering angle of the vehicle must be changed with the radius of the turn (R) or the lateral acceleration, a_y, in order to remain on the same curved trajectory. There are four common test methods to measure this property, namely: constant radius, constant speed, constant steer angle and constant throttle methods. The first two methods are most commonly used and are described here as detailed by [38].

6.2.2.1 Constant Radius Method

The understeer gradient can be determined by driving the vehicle in a constant radius and observing the steering angle versus lateral acceleration. Instrumentation is only required to measure the steering angle and lateral acceleration. The procedure (as recommended by [38]) is to drive the vehicle around a circle of constant radius at very low speed at which the lateral acceleration is negligible, and note the steering angle required to maintain the turn. The speed of the vehicle is then increased and the steering angle noted at each speed. The steering angle is then plotted as a function of lateral acceleration. The understeer gradient K is then equal to the derivative of this function.

6.2.2.2 Constant Speed Method

The understeer gradient can also be measured at constant speed by varying the steering angle. In this method, the radius of turn will vary continuously, requiring more extensive data collection. It is necessary to measure the speed, steering angle, as well as determine the radius of the turn for each condition. The radius of the turn can be measured either by measuring the lateral acceleration of the vehicle(a_y) or the yaw rate(r). The radius of the turn can then be determined from the following relationships.

$$R = \frac{V^2}{a_y} = \frac{V}{r}$$

where

V is the vehicle's forward speed (m/sec)

a_y is the lateral acceleration (m/sec^2)

r is the yaw rate $(radians/sec)$

The understeer gradient is then determined from the derivative of the steering angle with respect to the lateral acceleration, [38].
By performing the tests described above with a fully instrumented LHD vehicle using the VBOX II system it will be possible to determine the characteristics of a physical vehicle that can be used to validate the theoretical vehicle model.

6.2.3 Model Tuning Parameters

There are a number of vehicle model parameters which may need to be tuned in order to obtain better correlation between the simulation results and the measured results. Most of these parameters are estimated values that are not possible to measure as listed in table 6.1.

6.3 Chapter Summary

This chapter provides an overview of how the dynamic vehicle model developed in chapter 5 together with the tyre model could be validated and tuned to provide better results should a LHD vehicle be available to perform these experiments above ground.

Table 6.1: Estimated Model Parameters.

Parameter	Description
$C_{\alpha_f}, C_{\alpha_f}$	Cornering stiffness of front and rear tyres
I_{z1}, I_{z2}	Moment of inertia about vertical axis for front and rear unit
h	Height of centre of gravity
$L1$	Front axle to centre of gravity distance
$L2$	Rear axle to centre of gravity distance
μ	Friction coefficient
P_f, P_r	Longitudinal force on front and rear tyres

Chapter 7

Vehicle Model Simulations

This chapter provides simulation results of the various LHD vehicle models discussed and developed previously in this dissertation. The simulations were performed using Matlab and the results of the various model simulations are discussed and analysed.

7.1 Kinematic Model Simulation

A purely reactive navigation scheme based on a wall following approach is illustrated in this section through simulation.

The simulations performed in this section are based on physical characteristics of the Atlas Copco Wagner ST-3.5 6 ton capacity Scooptram LHD. This particular vehicle has a half-length, L=1.449m and a maximum steering angle (ϕ) of 85° or 42.5° in each direction. The environment used in the simulation is a two dimensional area of 220 units by 220 units. The simulations have been created in such a manner that each unit is equivalent to one metre. Within the two dimensional environment boundaries have been defined in order to simulate underground tunnel walls. The tunnel layout consists of a straight line movement in the x direction (from left to right) for 100m, then a 90° left turn followed by a straight line movement in the y direction (upwards), this is followed by a curvature of constant radius forward from left to right.

Due to the nature of the simulation it was decided to implement a reactive navigation scheme in which the vehicle navigates through the environment by means of a wall following algorithm. A block diagram of the system is shown in figure 7.1. As noted by [3], the system is different to the typical closed loop control systems, since the loop is closed around the environment. In figure 7.1, y_d refers to the desired wall following distance while y_a is the actual wall following distance and γ is the steering angle of the vehicle used to control the wall following distance.

Although this model is in fact nonlinear, it was found in this simulation that it was

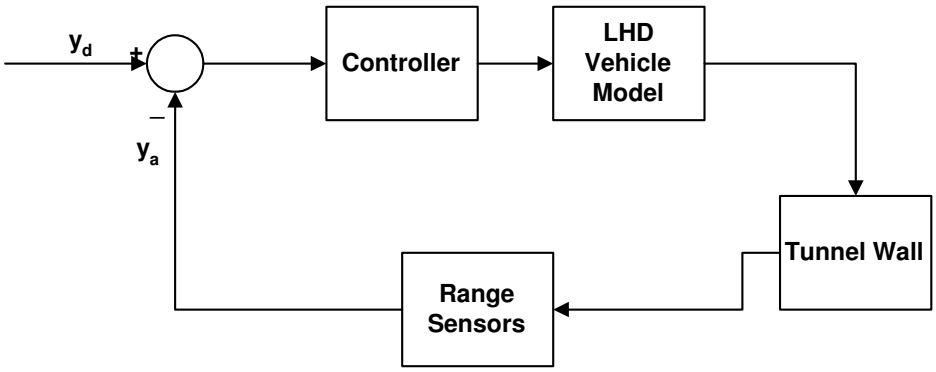

Figure 7.1: Loop diagram of sensor based control system.

possible to control the wall following distance, using a linear proportional, integral and derivative (PID) controller. The velocity form of the PID controller was used due to its ease of implementation and added advantage of not suffering from integral windup, [53].

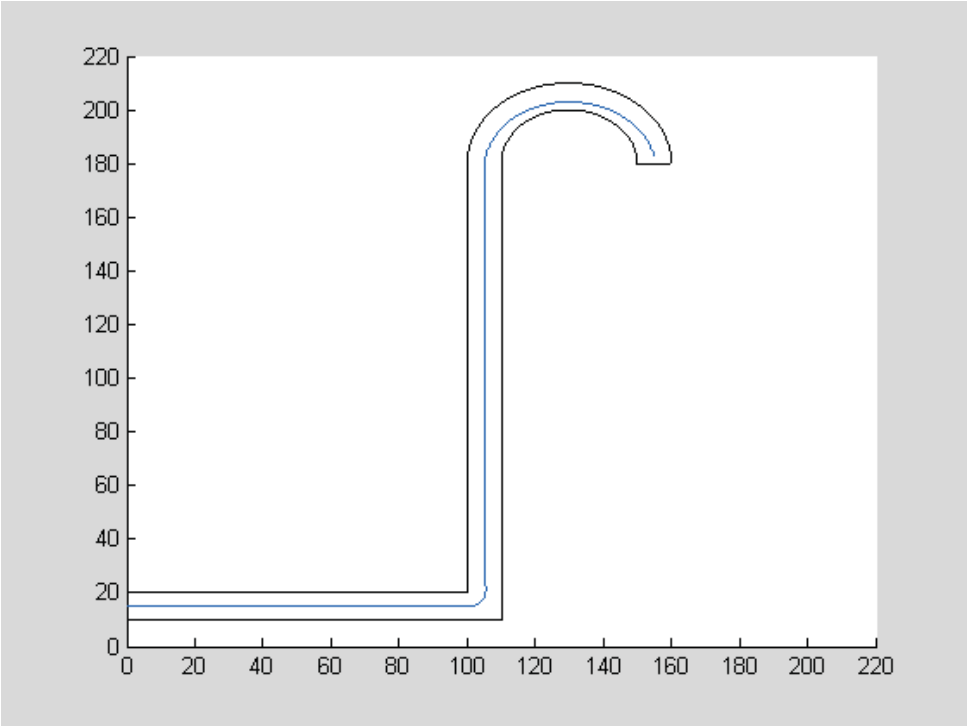

Figure 7.2: Plot of simulation results showing tunnel walls and the trajectory followed by the vehicle

The simulation results show that the vehicle is able to navigate a tunnel with both a 90° corner and a curvature of constant radius. The vehicle should therefore be able to cope with most cornering demands that would occur in a typical mine tunnel layout.
This control strategy has proven to work on a scale model implementation of an LHD

vehicle performed in an undergraduate project at the University of Pretoria, [54]. Figure 7.3 shows a photograph of the scale model of an Atlas Copco Wagner ST-3.5 6 ton capacity Scooptram LHD. The PID control strategy has been proven to work effectively and the results compare favourably with the software simulation under the same operating conditions.

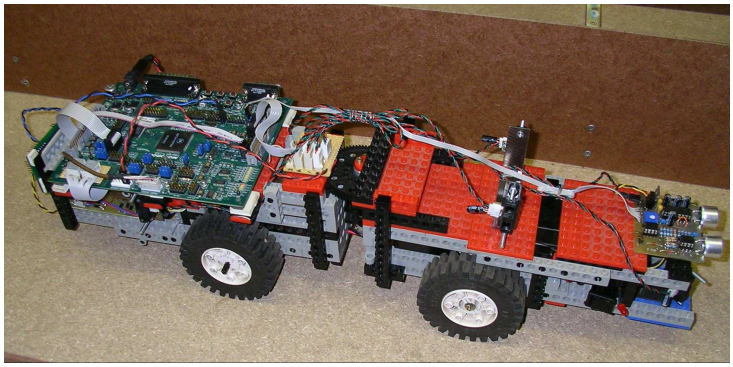

Figure 7.3: Photograph of scale model of LHD vehicle with ultrasonic and infrared range sensors.

The range sensors where implemented by means of ultrasonic and infrared sensors while processing was performed by means of and onboard Digital Signal Processor. More detail can be found in [54].

7.2 EKF Model Simulation

A second simulation was then performed using the extended kalman filter (EKF) model (5.5) in the same tunnel environment with the same control strategy as for the previous simulation. In this simulation a discretised version of (5.5) was used in order to estimate the position and orientation of the LHD vehicle under the same control strategy but including the effects of slip.
The EKF was provided with the approximate position, (position including additive noise), of the LHD vehicle at one second intervals to simulate the use of a rotating laser scanner which can provide localisation information from markers installed on the tunnel walls. This information was given directly to the filter as an observation model. An observation model including the necessary bearing calculations for a laser scanner or such device as used by [28] will be added in future work.
The simulation was performed by making use of the Matlab toolbox KALMTOOL created by [55] in order to implement the EKF.
Figure 7.4 shows the simulation results for the EKF model. The crosses ('+') indicate

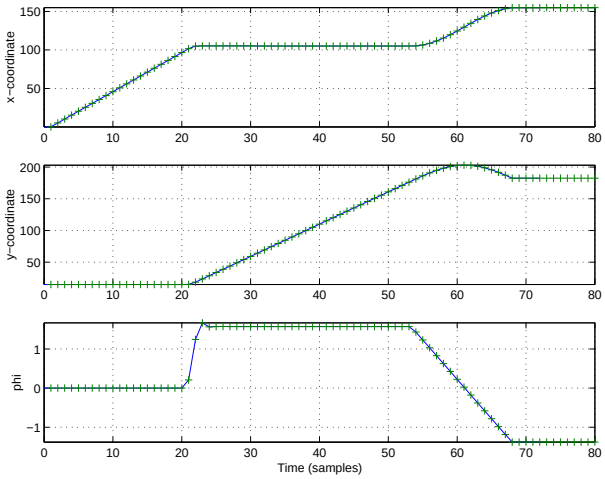

Figure 7.4: Plot of simulation results for EKF model

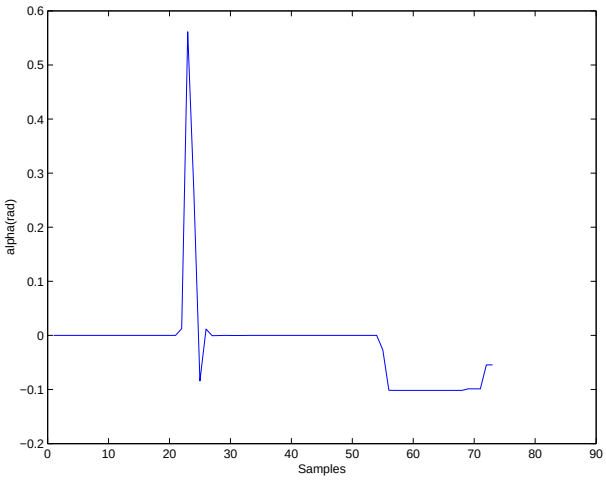

Figure 7.5: Plot of predicted slip angle α

samples provided by the observation model while the line indicates the predicted output of the model. From figure 7.4 it is clear that these two lines nearly coincide. Notice that the line created by plotting the combination of the x and y graphs in figure 7.4 follow the same trajectory as followed in figure 7.2.

Figures 7.5, 7.6 and 7.7 show the simulation results for the predicted slip angles α and β as well as the wheel radius R respectively. It should be noted that the noise strengths where chosen arbitrarily and should be determined experimentally depending on the physical equipment being used.

It should be noted that the model predicts a relatively large decrease in the effective wheel radius of the vehicle. This however is not due to the two typical main causes of a change in wheel radius, namely tyre wear which is a long term factor and vehicle loading which

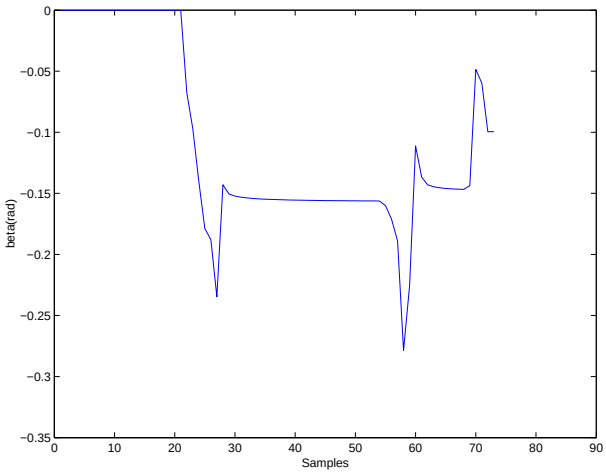

Figure 7.6: Plot of predicted slip angle β

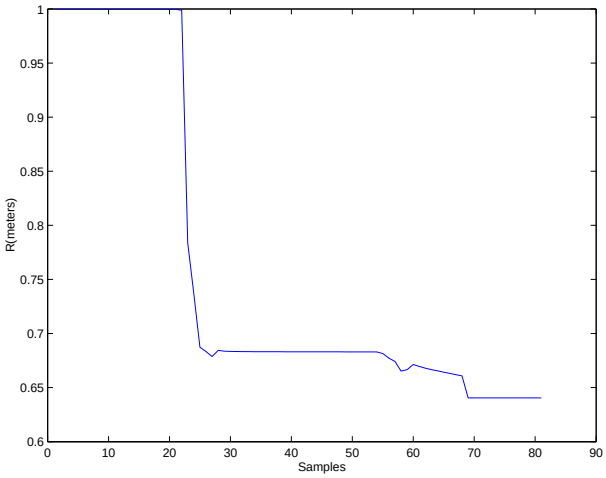

Figure 7.7: Plot of predicted wheel radius R

results in a step change in the vehicle's effective wheel radius. The reason that the vehicle model predicts a decrease in the effective wheel radius is due to the fact that increased side slip results in a decreased vehicle forward velocity. The model interprets this decrease in forward speed as being caused by a reduction in the effective wheel radius.
From the simulations performed it is evident that both the no-slip and slip models produce similar results for the tunnel layout, control strategy and noise strengths used in this simulation. The performance of the model incorporating the effects of slip is dependant on the sampling rate of the rotating laser scanner used to measure the position of the vehicle from the markers installed in the tunnel walls. At sampling rates lower than one second the performance will deteriorate.
The results appear to agree with the statement made by [41] that it is possible to neglect the dynamic forces which cause slip because of the LHD being a low speed vehicle. However due to the safety critical nature of autonomous navigation and the possibility of more demanding tunnel layouts that may occur it is best to use the most accurate model available. The EKF model is suitable to be used for this purpose, however the statistical parameters of the error model need to be determined experimentally so as to be certain of the accuracy.

7.3 Single-Track Model Simulation

This section provides the simulation results for the single-track LHD vehicle model described in chapter 5. Simulation results are shown for a loaded and unloaded Sandvik Tamrock EJC 245 LHD [48]. In both simulations the trajectory followed by the single-track LHD model is compared to that indicated by the pure kinematic model under the same conditions. The simulations are based on the calculations performed in section 5.3 of chapter 5.

7.3.1 Unloaded LHD Vehicle Single-track Model

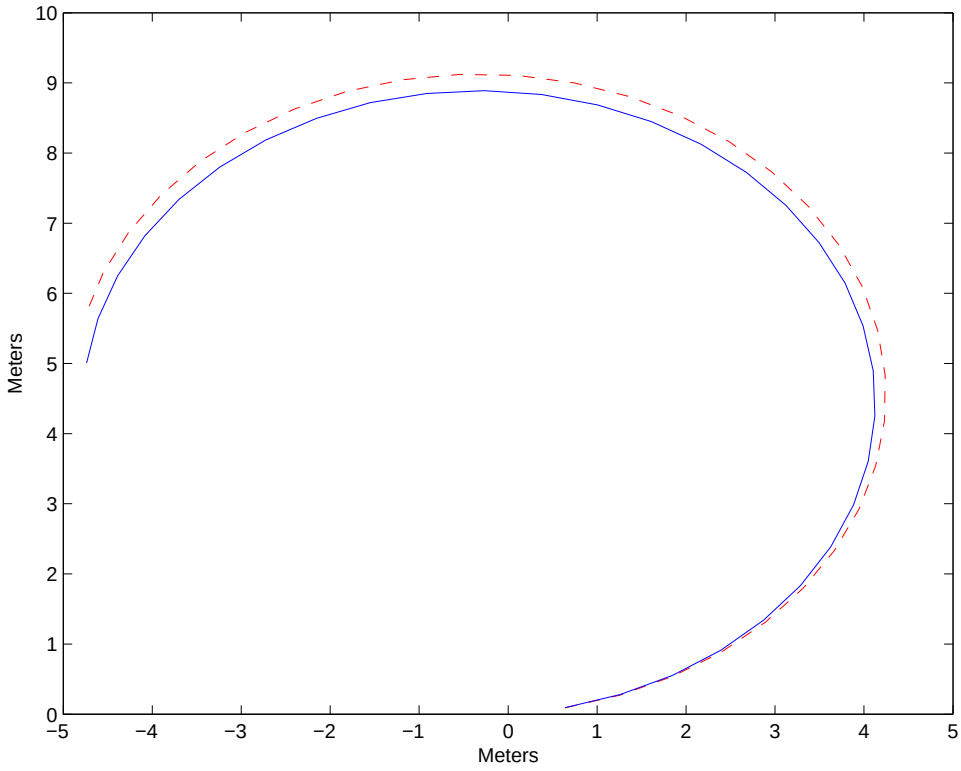

Figure 7.8: Plot of trajectory predicted by kinematic vehicle model (dashed line) and Unloaded single-track vehicle model (solid line) for a curvature of constant radius.

7.3.2 Loaded LHD Vehicle Single-track Model

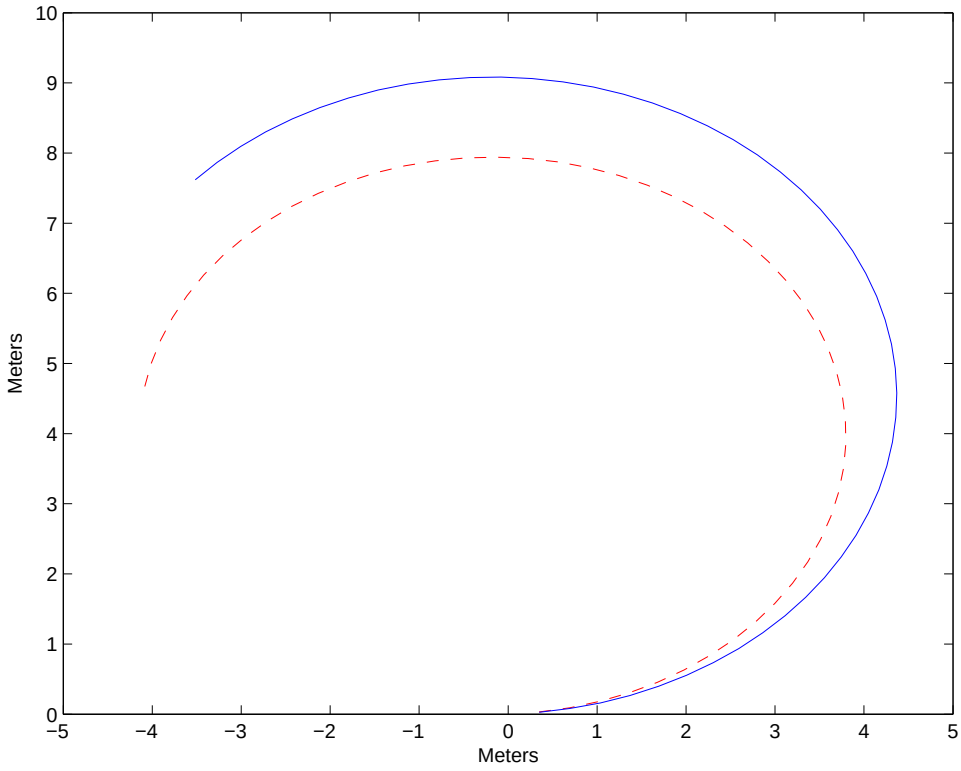

Figure 7.9: Plot of trajectory predicted by kinematic vehicle model (dashed line) and loaded single-track vehicle model (solid line) for a curvature of constant radius.

7.3.3 Single-Track Model Simulation Discussion

The results for the single-track vehicle dynamic model, although based on approximated tyre characteristics as described in chapter 5, provides two important results to consider for the practical implementation of an autonomous navigation and guidance system for an LHD vehicle.

Firstly the simulations show that including the dynamic effect of slip in the vehicle model provides a considerable difference in the vehicles performance in comparison to the kinematic vehicle model which ignores the effects of slip. Secondly the results show that the load carried by the LHD vehicle has a marked impact of the vehicles handling characteristics. It will therefore be necessary to have a controller that is capable of dealing with the change in the vehicles characteristics. This will necessitate that the load carried by the vehicle be measured to adjust the control system as required. At present the LHD vehicles do not measure the load carried in the scoop. Implementing some form of load measurement system on the vehicle will have the added advantage of allowing the pro-

duction of the vehicles to be measured more accurately, which will have added benefits in terms of analysing the mines productivity. This information can then also be used in scheduling and dispatch systems to optimise the vehicles productivity as discussed in [16].

7.4 Complex Vehicle Model Simulations

This section shows the simulation results of the complex vehicle model obtained using Matlab.

The simulation results where obtained by means of applying optimal control, through nonlinear programming to compute discrete time feasible open loop strategies for the vehicle speed and articulation angle to control the model to the desired position. The method used is based on that described in [56]. The vehicle parameters used in the model for the simulations are based, as far as possible, on the physical characteristics of a Sandvik Tamrock EJC245 LHD vehicle, [48].

7.4.1 Control Strategy

The control law makes use of the inverse dynamic model derived in section 5.4 of chapter 5 of this dissertation. The complex vehicle model can be written in the following inverse dynamics form as follows:

$$\begin{pmatrix} \ddot{\mathbf{x}} \\ \ddot{\mathbf{y}} \\ \ddot{\epsilon_1} \\ \ddot{\epsilon_f} \end{pmatrix} = - \begin{pmatrix} m11 & m12 & m13 & m14 \\ m12 & m11 & m23 & m24 \\ m13 & m23 & m33 & m34 \\ m14 & m24 & m34 & m44 \end{pmatrix}^{-1} \begin{pmatrix} \mathbf{h_1} \\ \mathbf{h_2} \\ \mathbf{h_3} \\ \mathbf{h_4} \end{pmatrix} + \begin{pmatrix} m11 & m12 & m13 & m14 \\ m12 & m11 & m23 & m24 \\ m13 & m23 & m33 & m34 \\ m14 & m24 & m34 & m44 \end{pmatrix}^{-1} \begin{pmatrix} \mathbf{F_{gx_n}} \\ \mathbf{F_{gy_n}} \\ \mathbf{F_{g\epsilon_1}} \\ \mathbf{F_{g\epsilon_f}} \end{pmatrix}$$

where $\mathbf{F_{gx_n}}, \mathbf{F_{gy_n}}, \mathbf{F_{g\epsilon_1}}, \mathbf{F_{g\epsilon_f}}$ are as defined in (5.49) to (5.53) of chapter 5.
and

$$\mathbf{h_1}=\tfrac{1}{2}m_2D_2\dot{\epsilon_1}\cos(\epsilon_f+\epsilon_1)(\dot{\epsilon_f}+\dot{\epsilon_1})+m_2D_1\dot{\epsilon_1}^2\cos(\epsilon_1)+\tfrac{1}{2}m_2D_2\dot{\epsilon_f}\cos(\epsilon_f+\epsilon_1)(\dot{\epsilon_f}+\dot{\epsilon_1}) \tag{7.1}$$

$$\mathbf{h_2}=m_2D_1\dot{\epsilon_1}^2\sin\epsilon_1+\tfrac{1}{2}m_2D_2\dot{\epsilon_1}\sin(\epsilon_f+\epsilon_1)(\dot{\epsilon_f}+\dot{\epsilon_1})+\tfrac{1}{2}m_2D_2\dot{\epsilon_f}\cos(\epsilon_f+\epsilon_1)(\dot{\epsilon_f}+\dot{\epsilon_1}) \tag{7.2}$$

$$\mathbf{h_3}=-m_2D_1D_2\dot{\epsilon_f}\dot{\epsilon_1}\sin\epsilon_f-\tfrac{1}{2}m_2D_2D_1\dot{\epsilon_f}^2\sin\epsilon_f+\tfrac{1}{2}m_2D_2\dot{x}\dot{\epsilon_1}\cos(\epsilon_f+\epsilon_1)+\tfrac{1}{2}m_2D_2\dot{\epsilon_f}\dot{x}\cos(\epsilon_f+\epsilon_1) \tag{7.3}$$

$$+m_2D_2\dot{x}\dot{\epsilon}1\cos(\epsilon_1)-m_2D_1\dot{x}\dot{\epsilon_f}\cos(\epsilon_1)-\tfrac{1}{2}m_2D_2\dot{x}\sin(\epsilon_f+\epsilon_1)-m_2D_1\dot{x}\sin(\epsilon_1) \tag{7.4}$$

$$\mathbf{h_4}=\tfrac{1}{2}m_2D_2\dot{x}\dot{\epsilon_1}\cos(\epsilon_f+\epsilon_1)-\tfrac{1}{2}m_2D_2\dot{x}\dot{\epsilon_f}\cos(\epsilon_f+\epsilon_1)+\tfrac{1}{2}m_2D_2D_1\dot{\epsilon_1}^2 sin\epsilon_f \tag{7.5}$$

The trajectory followed by the vehicle can then be found from the double integral of these dynamic equations. In order for the system to be simulated it is however necessary to write the inverse dynamic model as a state-space model.

Once the system has been written as a system of first order equations a multi-variable Runge-Kutta algorithm is applied to solve the first order differential equations.
Writing the system as a set of first order differential equations results in a model with eight states as each second order state results in two first order states. This results in a vehicle model with the following state vector, $\mathbf{q} = [x, \dot{x}, y, \dot{y}, \epsilon_1, \dot{\epsilon_1}, \epsilon_f, \dot{\epsilon_f}]^T$
where

x is the velocity in the x-direction.

$\dot{x}$ is the acceleration in the x-direction.

y is the velocity in the y-direction.

$\dot{y}$ is the acceleration in the y-direction.

ϵ_1 is the rate of change of heading (yaw rate).

$\dot{\epsilon_1}$ is the acceleration in the rate of change of heading (yaw acceleration).

ϵ_f is velocity at which the articulation angle is changing.

$\dot{\epsilon_f}$ is the acceleration in the change in articulation angle.

Using this system of first order differential equations it is then possible to search for an optimal control vector to drive the system of nonlinear differential equations to the desired setpoint within certain defined constraints. These constraints are formulated into a cost or penalty function ($J(\mathbf{c})$). The aim of the optimisation is to find a feasible command vector $\mathbf{c^o}$ which causes the system to remain within the constraints and find a optimal solution that renders $J(\mathbf{c^o}) = 0$ or close to zero.
In order to control the model the initial state of the model needs to be defined. The desired state or setpoint of the model needs to be decided upon as well as the desired time to reach the setpoint. The optimisation is then applied to reach this setpoint state within the allotted time and constraints if it is possible.The optimisation then works by dividing the known time period up into steps, $\Delta_c = \frac{1}{100}$. Once Δ_c is known the time span can be divided into splines, $A_i(t)$ (7.6) and $B_i(t)$ (7.7).

$$A_i(t) = \frac{\tau_{i+1} - t}{\Delta_c} \quad where \;\; i = 0, ..., N-2 \tag{7.6}$$

$$B_i(t) = \frac{t - \tau_i}{\Delta_c} \quad where \;\; i = 0, ..., N-2 \tag{7.7}$$

With the calculated values of A and B the auxiliary control functions $\mathbf{v} = [v_1, v_2]^T : [0, t_f]$ can be solved for once $\mathbf{c}$ is substituted into equations (7.8) and (7.9).

$$v_1(t) = A_i(t)c_i + B_i(t)c_(i+1) \quad t \in [\tau_i, \tau_{i+1}] \quad where \quad i = 0, ..., N-2 \tag{7.8}$$

$$v_2(t) = A_i(t)c_{N+i} + B_i(t)c_{(N+i+1)} \quad t \in [\tau_i, \tau_{i+1}] \quad where \quad i = 0, ..., N-2 \tag{7.9}$$

By substituting the auxiliary control vector $\mathbf{v}$ into the system of first order differential equations and applying the multivariable fourth order Runge-Kutta algorithm the solution to the differential equations can then be found. These solutions are then evaluated in the cost or penalty function (7.10). The auxiliary control vectors v_1 and v_2 are the two control inputs to the model. Effectively v_1 consists of an x and a y component which is added to the generalised forces in either the F_{gx_n} and F_{gy_n} depending on the heading of the vehicle. Thus v_1 can be viewed as the speed input of the vehicle. v_2 is the steering input of the vehicle which acts on the vehicle model by manipulating the generalised force $F_{g\epsilon_f}$.

$$J(\mathbf{c}) = G(\dot{x_D} - \dot{x}(t_f), \epsilon) + G(\ddot{x_D} - \ddot{x}(t_f), \epsilon) + G(\dot{y_D} - \dot{y}(t_f), \epsilon) + G(\ddot{y_D} - \ddot{y}(t_f), \epsilon) + G(\epsilon_f, -42.5°, 42.5°) + G(\dot{\epsilon_f}, -20, 20) \tag{7.10}$$

where $G(z, e)$ and $G(z, e_1, e_2)$ are defined as follows

$$G(z, e) = [max(z - e, 0) + min(z - e, 0)]^2 \quad e > 0 \tag{7.11}$$

$$G(z, e_1, e_2) = [min(z - e_1, 0) + max(z - e_2, 0)]^2 \quad 0 < e_1 < e_2 \tag{7.12}$$

where $e = 1 \times 10^{-6}$ is chosen as an error tolerance for the cost function.
An optimisation algorithm is then used to find a solution to the entire system by altering the command vector, $\mathbf{c}$. The algorithm continues to search for a new command vector, as long as the cost function is decreasing, or the cost comes within a certain tolerance of zero or alternatively a certain maximum number of iterations is exceeded. For the purposes of this dissertation Matlab's *fminunc* function was used to determine this minimum.
As an example a simulation result is shown in figure 7.12 and 7.11 for an optimisation where $[\dot{x_D}(t_f), \ddot{x}_D(t_f), \dot{y}_D(t_f), \ddot{y}_D(t_f), \dot{\epsilon}_{1D}(t_f), \ddot{\epsilon}_{1D}(t_f), \dot{\epsilon}_{fD}(t_f), \ddot{\epsilon}_{fD}(t_f)]^T$ was chosen as $[3,\ 0,\ 0,\ 0,\ 0,\ 0,\ 0,\ 0]^T$ and $t_f = 10s$.
The results show that the controller is able to drive the velocity in the x direction close to the setpoint of $3m/s$, (figure 7.12). Figure 7.11 shows the acceleration in the x direction versus time and it shows how the acceleration increases to the maximum value of $0.4m/s^2$ in order to achieve the desired x velocity within the specified time. The acceleration then

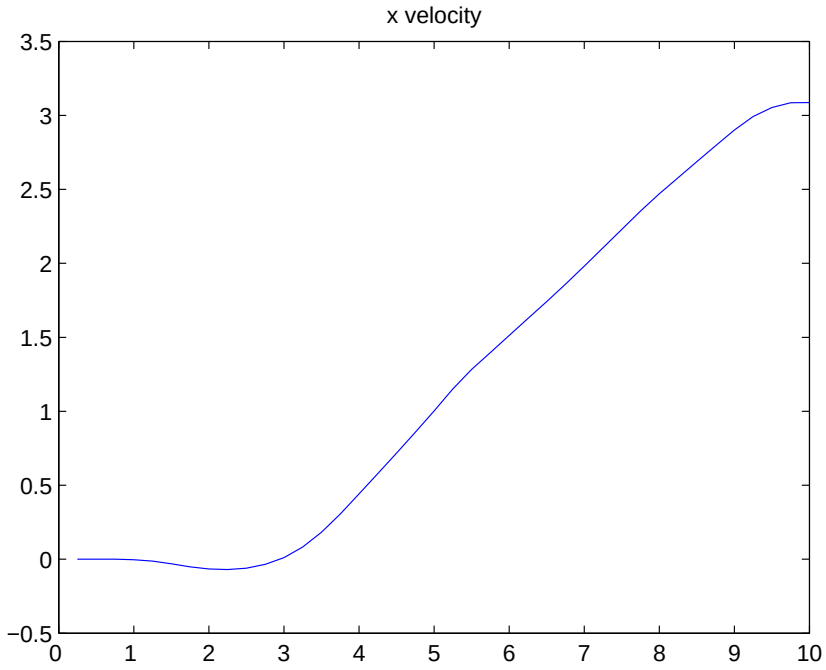

Figure 7.10: Plot of $\dot{x}$ versus time.

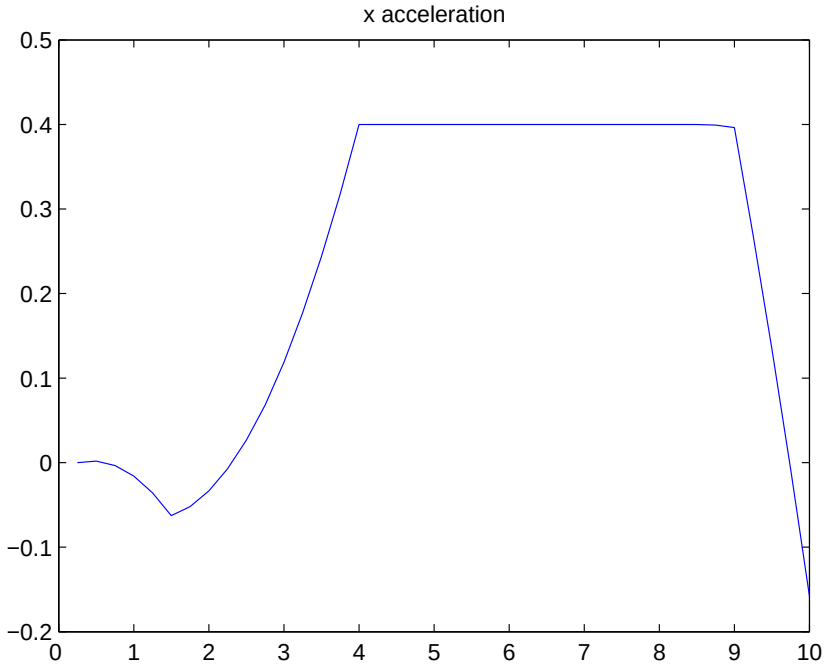

Figure 7.11: Plot of $\ddot{x}$ versus time.

decreases back to the setpoint of $0m/s^2$ by the end of the specified time. More detailed

simulation results are given in the next section.

7.4.2 Simulation Results

This section contains more detailed simulation results for the complex vehicle model. All simulations were performed using the control philosophy described previously. Table 7.1 contains a list of the vehicle parameters used within the model for the simulations. Values that were not available for the LHD vehicle were estimated are also indicated in the table.

Table 7.1: LHD vehicle parameters used for simulations Parameters.

Parameter	Description	Value
m_1	Mass of front unit	$10523kg$
m_2	Mass of rear unit	$15498kg$
$Tw1$	Track width of vehicle axle	$2.565m$
C_{α_f}	Cornering stiffness of front tyres	$5300N/m$
C_{α_r}	Cornering stiffness of rear tyres	$4600N/m$
I_{z1}	Moment of inertia about vertical axis of the front unit	$65734Kg - m^{2*}$
I_{z2}	Moment of inertia about vertical axis of the rear unit	$65734Kg - m^{2*}$
h	Vertical height of centre of gravity	$1m$
h_l	Vehicle Half length	$1.727m$
$L1$	Distance between front unit C.G and front axle	$0.7m^{**}$
$L2$	Distance between rear unit C.G and rear axle	$0.825m^{**}$
μ	Friction coefficient	0.7 (Dry concrete)***
	Maximum Acceleration (empty)	$0.4m/s^{2****}$
	Maximum Declaration	$1m/s^{2****}$
$\dot{\epsilon_{fmax}}$	Maximum rate of change of steering angle	$20degrees/s^{@}$
ϵ_{fmax}	Maximum steering angle	$+/-42.5degrees$

* Indicates an assumed value based on values used in [43].

** Indicates an estimated value based on LHD vehicle size assuming uniform mass.

*** Friction coefficient at which the tyre data was obtained.

**** Acceleration values obtained from [18].

@ Steering rate dependant on engine revolutions per minute a typical maximum is assumed here.

Figures 7.12 to 7.20 below show the simulation results for all the vehicle model states as well as the trajectory followed by the vehicle for accelerating from standstill to 3 meters per second within a simulation time of 10 seconds. In mathematical terms the setpoints for the system $[x_D(t_f), \ddot{x}_D(t_f), \dot{y}_D(t_f), \ddot{y}_D(t_f), \dot{\epsilon}_{1D}(t_f), \ddot{\epsilon}_{1D}(t_f), \dot{\epsilon}_{fD}(t_f), \ddot{\epsilon}_{fD}(t_f)]^T$ were chosen to be as follows $[3,\ 0,\ 0,\ 0,\ 0,\ 0,\ 0,\ 0]^T$.

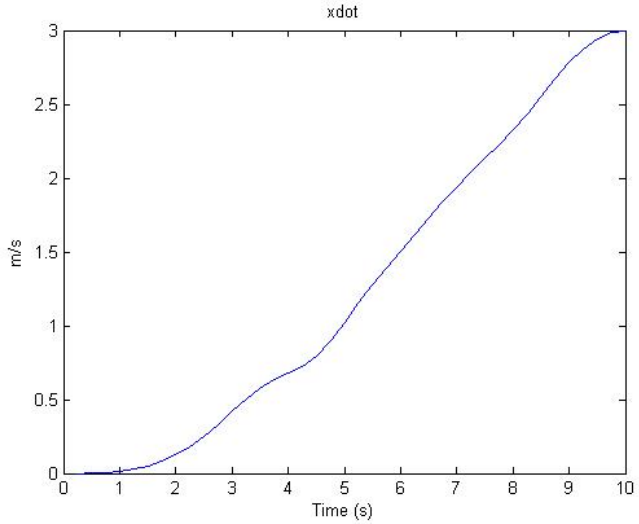

Figure 7.12: Plot of $\dot{x}$ versus time.

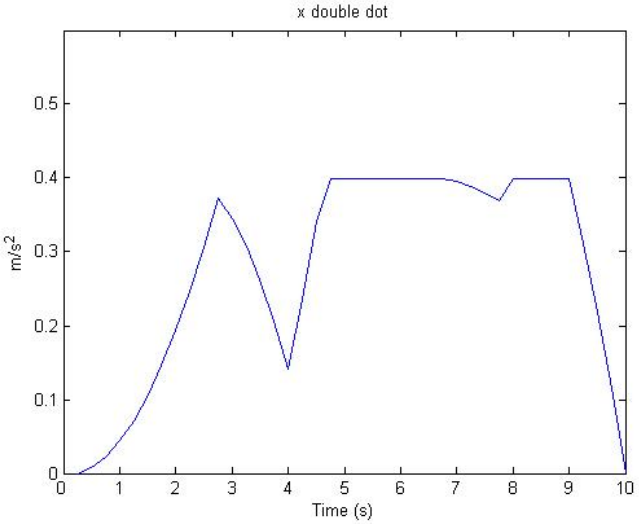

Figure 7.13: Plot of $\ddot{x}$ versus time.

Figure 7.12 shows how the x velocity reaches the setpoint within the 10 second simulation time while figure 7.13 shows how the acceleration of the vehicle increases with time until reaching the maximum acceleration possible for the vehicle of $0.4m/s^2$. The acceleration

then returns to zero once the velocity setpoint has been reached.

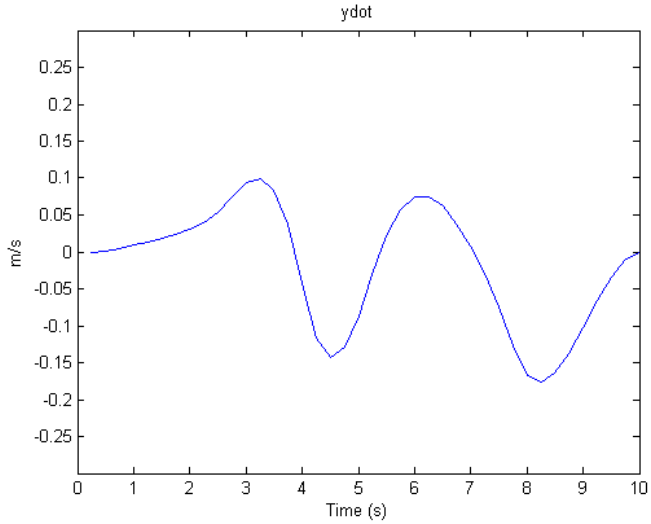

Figure 7.14: Plot of $\dot{y}$ versus time.

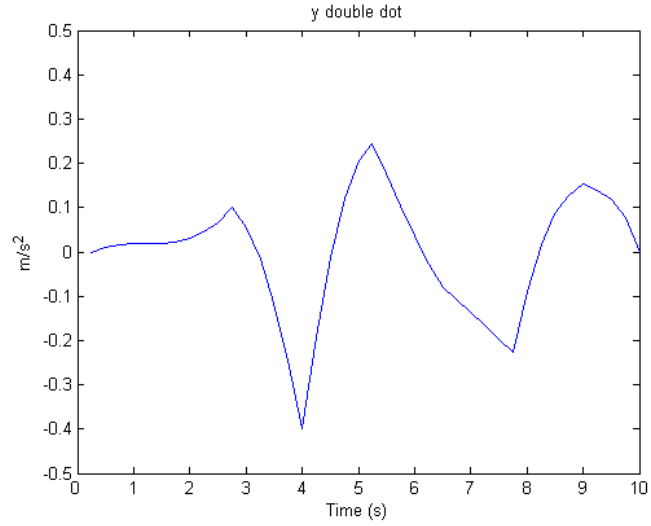

Figure 7.15: Plot of $\ddot{y}$ versus time.

Figures 7.14 and 7.15 show the variation of the velocity and acceleration of the vehicle in the y-direction. Although ideally for the setpoint chosen these states should remain zero this is not the case because as can be seen from figures 7.18 and 7.19 the articulation angle for the vehicle varies during the simulation period as the optimisation algorithm searches for a control vector to reach the desired setpoint within the desired time. Although there is a variation in the articulation angle and therefore the heading and velocity and acceleration in the y-direction. These variations are very small and the states do reach

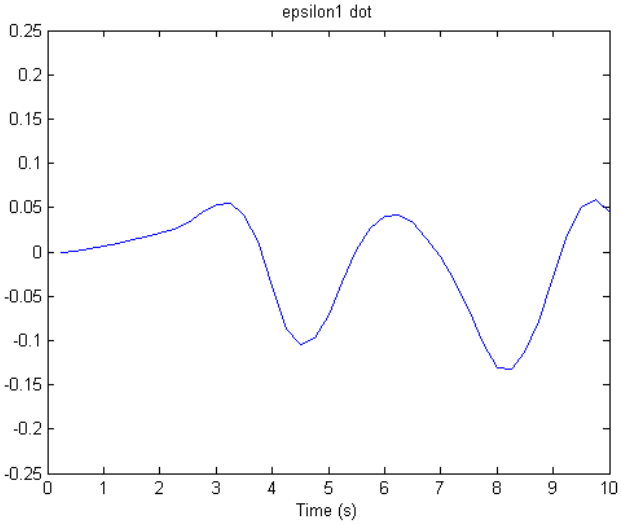

Figure 7.16: Plot of $\dot{\epsilon}$ versus time.

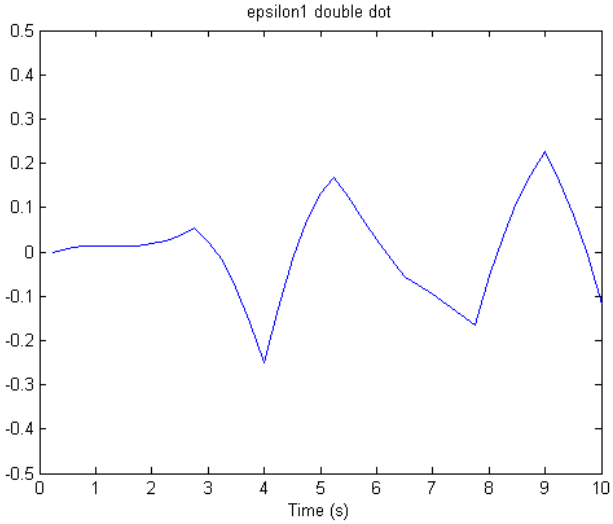

Figure 7.17: Plot of $\ddot{\epsilon}$ versus time.

the desired setpoint at time $t = 10s$. This is due to the interrelation between the various states and the two control inputs, namely the speed (acceleration) and the articulation angle. Small changes in the articulation angle have an immediate effect on the vehicles heading and therefore the acceleration and velocity of the y-direction. Figure 7.20 shows a plot of the trajectory followed by the vehicle for the simulation run. From the plot of the vehicles trajectory the effect of the alterations in steering angle is evident. However the effect these alterations have on the trajectory of the vehicle is negligible and the vehicle follows an approximately straight course in the direction of the x-axis.

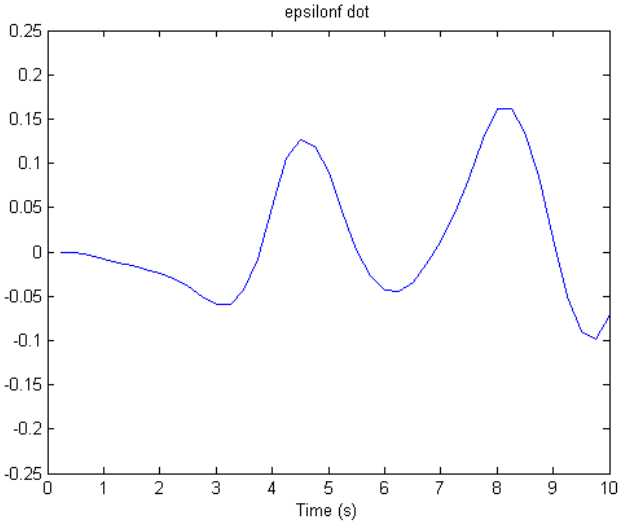

Figure 7.18: Plot of $\dot{\epsilon_f}$ versus time.

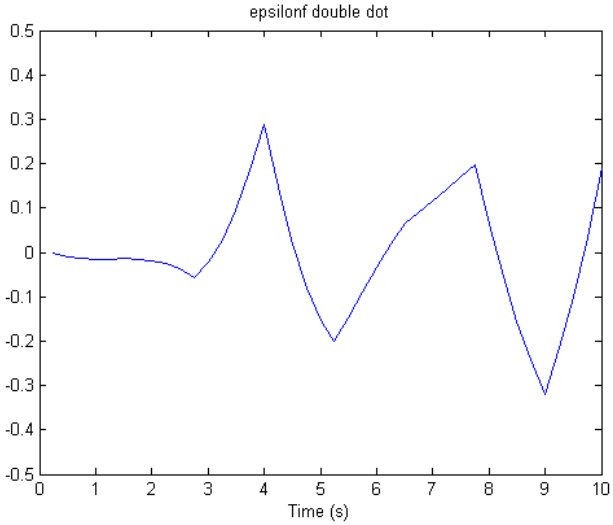

Figure 7.19: Plot of $\ddot{\epsilon_f}$ versus time.

Figure 7.21 shows a plot of the the slip angle for the front (dotted line) and the rear (solid line) slip angles of the tyres. Only one plot is given for each tyre on the individual axle as the results for both tyres on each axle are identical as roll motion is ignored in the model. The slip angle predicted by the model is largest for the initial large variations in the articulation angle, which is to be expected. The slip angle varies between peak values of -0.25 radians and 0.35 radians or between -14 degrees and 20 degrees. As is to be expected the slip angles decrease as the vehicle trajectory straightens out over the simulation period.

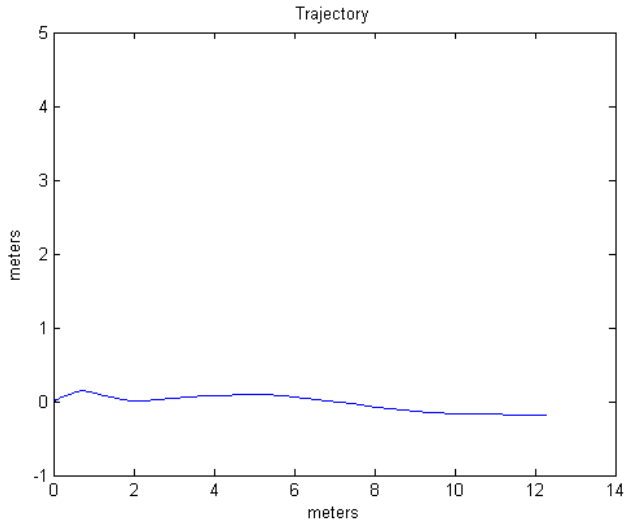

Figure 7.20: Plot of trajectory travelled by vehicle during simulation.

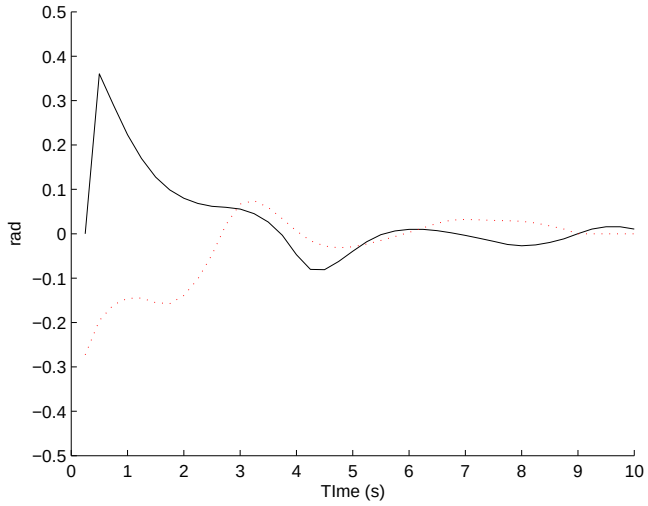

Figure 7.21: Plot of the slip angle predicted by the vehicle model for the trajectory travelled by vehicle. Front tyre slip angle indicated by dotted line, rear tyre slip angle indicated by solid line.

A second vehicle simulation was carried out in which the vehicle model was forced to drive a curved trajectory in order to see the effect on the slip angles generated by the tyre model. The trajectory followed by the vehicle is shown in figure 7.22, and the plots of the various state variables over the ten second simulation period are given in figures 7.23 to 7.30.

Figure 7.23 shows how the velocity of the vehicle increases as the vehicle starts moving in the x-direction and then starts to decrease as the vehicles heading changes and the velocity

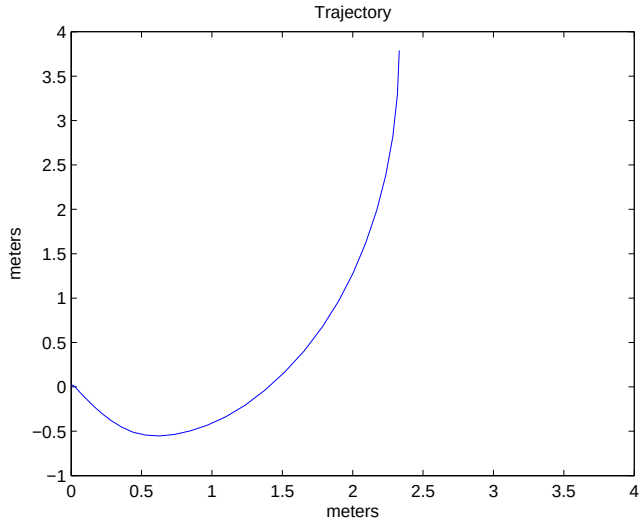

Figure 7.22: Plot of trajectory travelled by vehicle during simulation.

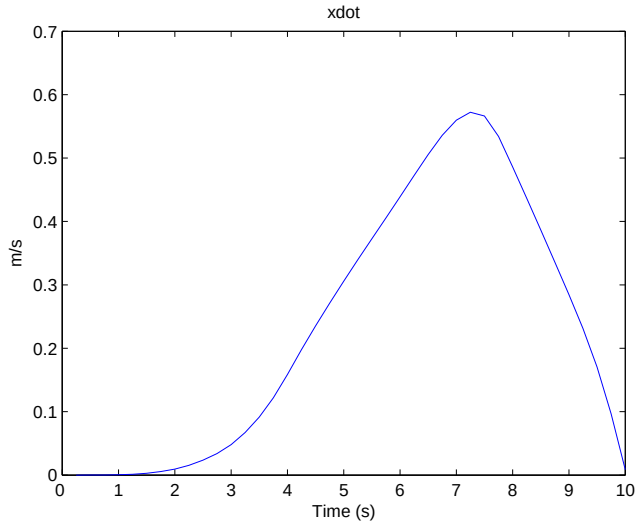

Figure 7.23: Plot of $\dot{x}$ versus time.

increases in the y-direction as shown in figure 7.26. The graphs of the x and y components of the vehicle acceleration also increase and decrease in magnitude corresponding to the vehicle's rate of change of heading as shown in figures 7.25 ,7.26 and 7.29 respectively. Figure 7.29 shows a plot of the rate of change of the vehicle's articulation angle for the motion and figure 7.30 shows the acceleration of the articulation joint.

Figure 7.31 shows a plot of the slip angle predicted by the tyre model for the vehicles motion. The slip angle for the front axle is shown in a solid line while the rear axle's is plotted using the dashed line. As can be seen from the figure for the initial part of the simulation, when the plot of the vehicle's trajectory shows that the vehicle is cornering

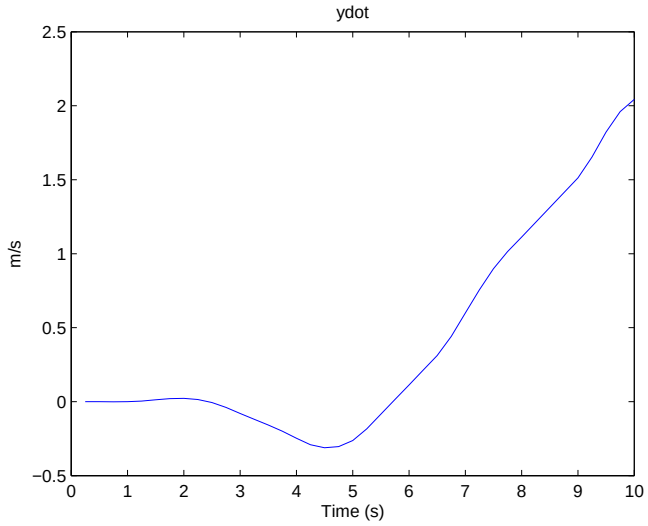

Figure 7.24: Plot of $\dot{y}$ versus time.

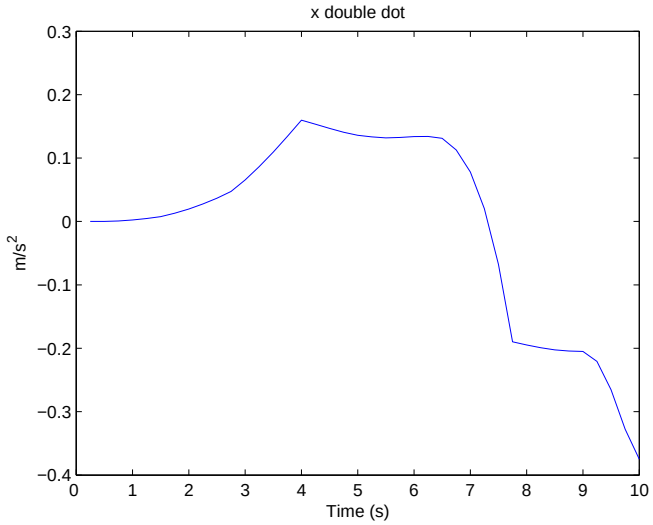

Figure 7.25: Plot of $\ddot{x}$ versus time.

sharply (around a small radius), the tyre model is predicting large slip angles which is intuitively correct. However the magnitude of the slip angle predicted is excessive in that the peak value is approximately $1.5rad$ or 85°. Clearly this is an excessive value. A possible explanation for this is that the tyre data used for the tyre model is based on a smaller and lighter vehicle than the values used for the LHD vehicle in the simulation. Due to the shape of the cornering stiffness versus side force curve, when large side forces are required the tyre is no longer operating in the linear region of the curve and therefore the model predicts excessively large slip angles required to generate the necessary side force during the cornering manoeuvre to maintain the trajectory of the vehicle. The

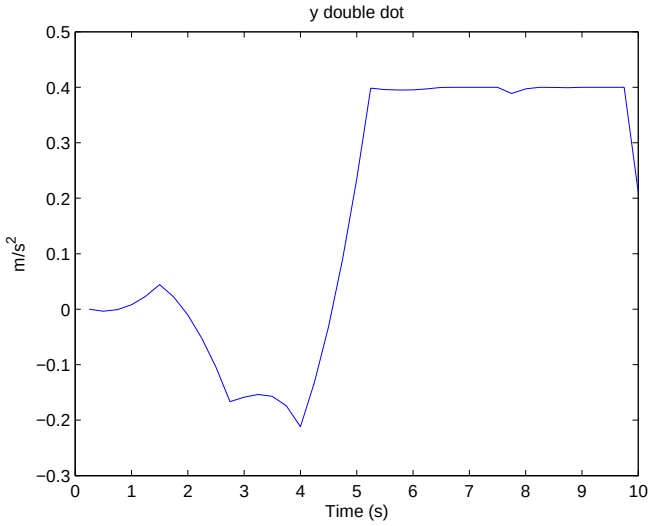

Figure 7.26: Plot of $\ddot{y}$ versus time.

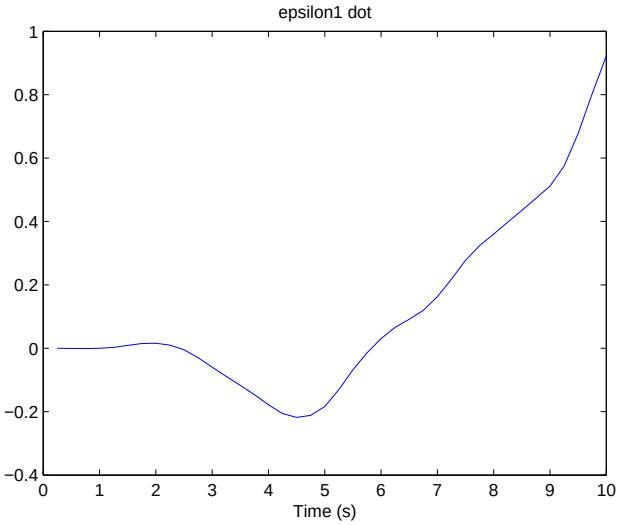

Figure 7.27: Plot of $\dot{\epsilon}$ versus time.

model does however predict a widening in the trajectory being followed by the vehicle due to the slip angle which is correct.

7.4.3 Complex Vehicle Model Discussion

The simulation results show that the open loop non-linear feasible control strategy is able to control the LHD vehicle model successfully within the defined constraints of the model. For a setpoint which is chosen outside the feasible limits of the vehicle model, such as requiring the vehicle to accelerate to a higher speed than is it capable of, the cost

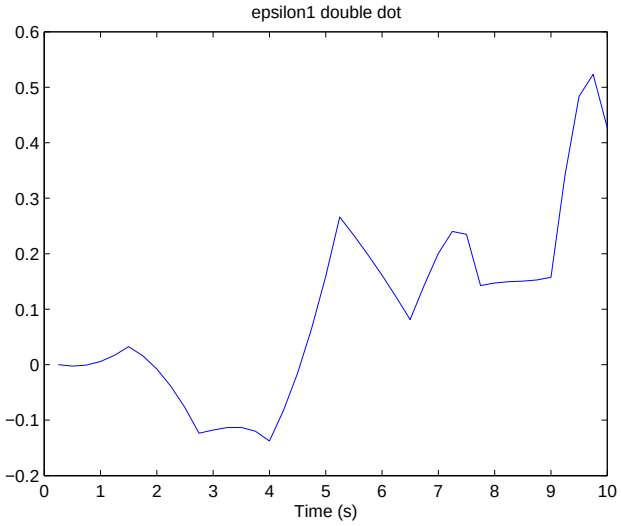

Figure 7.28: Plot of $\ddot{\epsilon}$ versus time.

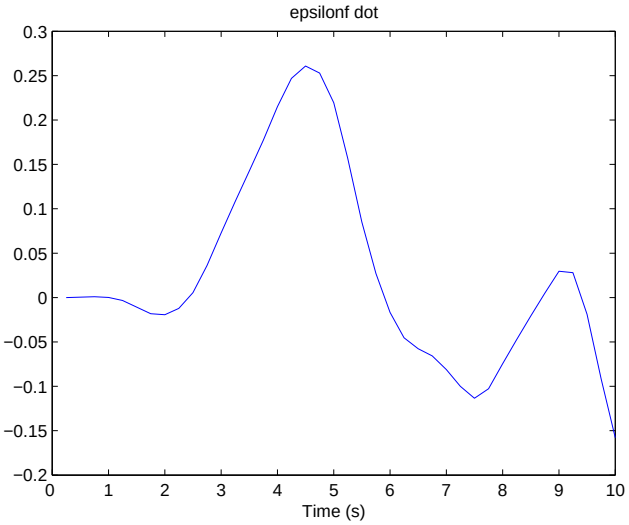

Figure 7.29: Plot of $\dot{\epsilon_f}$ versus time.

function will not be minimised to zero and the setpoint or allowable time would need to be adjusted.

The complex vehicle model appears to perform well and it is possible to find feasible command vectors for most desired vehicle dynamics. This method of control and hence the complex vehicle model does however suffer from a number of drawbacks. Firstly the model is not very intuitive or easy to use and interpret. This is due to the complex manner in which the setpoint needs to be defined as well as the associated time frame for the desired maneuver by the vehicle. Complex maneuvers need to be defined in terms of a number of short simple tasks and an optimisation needs to be carried out for

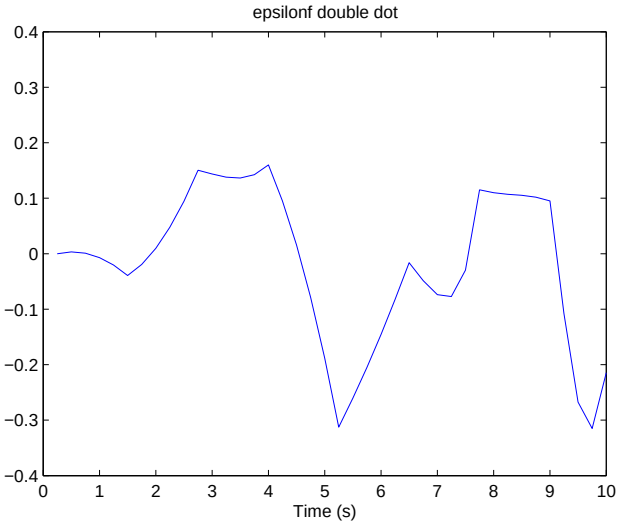

Figure 7.30: Plot of $\ddot{\epsilon_f}$ versus time.

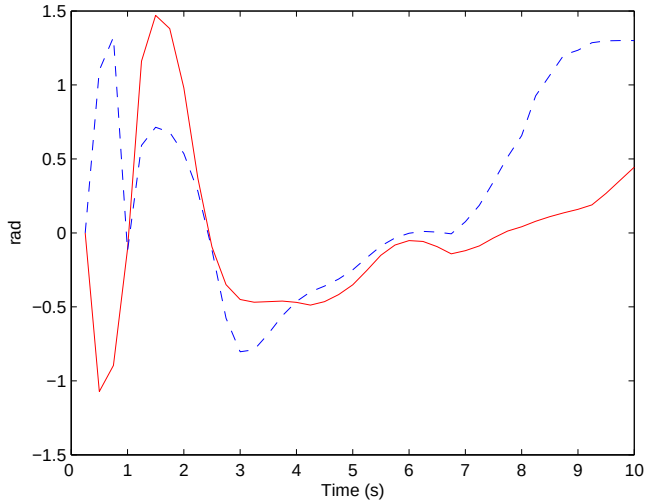

Figure 7.31: Plot of the slip angle predicted by the vehicle model for the trajectory travelled by vehicle. Slip angle for a front tyre is indicated by the solid line and the slip angle for a rear tyre is indicated by a dotted line.

the vehicle to reach each individual task of the complex maneuver. This is extremely time consuming and difficult to do. However once the optimisation has been carried out the optimal command vector can be stored and theoretically can be used to control the vehicle to drive the same trajectory repeatedly. Secondly due to the complexity of the vehicle model the simulation times are excessively long even for a simulation with a relatively low time resolution. This problem could however possibly be addressed by optimising the software implementing the model. A more fundamental flaw of the model

is its impracticality in terms of implementation of a control algorithm on a physical LHD vehicle for a number of reasons, such as the computational power required on board the vehicle and the lack of robustness to external disturbances.
The model does however have a number of improvements over the previous dynamic model as described in [57],[58]. The main improvement being the implementation of a more accurate tyre model which is no longer only a linear approximation valid for small slip angles. The model now makes use of the complete range of cornering stiffness data available based on the data of figure 5.10. Nevertheless, as seen in the second simulation of the previous section, the tyre model still needs improvement especially for large slip angles. This could be addressed by using a more advanced mathematical tyre model as well as obtaining more accurate tyre data for the tyres of the vehicle.
The model does however have a number of benefits. Firstly due to the way in which the Lagrange dynamic model is derived it is relatively easy do adjust the model to the characteristics of other articulated vehicles such as articulated mining trucks for example simply by changing the values of the parameters shown in table 7.1 to match that of the new vehicle. Also although the model does not specifically take into account the effect of change in pitch or in other words elevation of the road surface this can be taken into account using the present model and adjusting the weights on the front and rear wheels using the concept of dynamic axle loads described in chapter 4.

7.5 Chapter Summary

This chapter provides simulation results for the various LHD vehicle models discussed in the previous chapter. The models are simulated using Matlab and the results are presented, discussed and analysed.

Chapter 8

Conclusion

8.1 Summary

A literature study was conducted into the field of autonomous vehicle guidance specifically focusing on the unique challenges posed by the underground mine environment, [57]. Different LHD vehicle models and modelling techniques have been studied and applied in simulation using Matlab,[59],[60],[61]. The results of the various modelling techniques were discussed and analysed. A shortcoming was found to be that most models do not model dynamic effects such as the slip angles of the tyres, which can have a marked influence on the path tracking ability of the autonomous vehicle. An LHD vehicle model was then derived using Lagrangian dynamics which is capable of taking into account the dynamic effect of tyre slip angles.
Due to the highly nonlinear nature of the model it was decided to implement an open loop nonlinear optimal control strategy to control the model for the purposes of simulation. The open loop control strategy was shown to be able to successfully control the vehicle model within the given constraints.

8.2 Conclusions

The aim of this study has been to develop a more accurate vehicle model including dynamic effects for an LHD underground mining vehicle. As discussed in [11] vehicle models have an important role to play in sensor based navigation. By improving the vehicle model and using the same sensors, improved navigation can be achieved. Alternatively with an improved vehicle model and fewer sensors the same level of navigation can be achieved reducing infrastructure and maintenance costs.
The Lagrange dynamic vehicle model derived in this dissertation will, after the necessary tuning during model validation procedure, prove to be a more accurate model for an LHD

vehicle in terms of path tracking, provided the correct tyre data can be obtained. Due to the complex computational intensive nature of the model and the open loop control strategy; the model and open loop controllers do not lend themselves to straightforward physical implementation on an LHD vehicle. While the open loop control strategy can be improved by streamlining and optimisation of the model, as well as increased processing power, the system will always suffer from a lack of robustness to disturbances. The model could however be used in a role similar to that of a Kalman filter where it is used to update and improve the estimate of the vehicles position between samples in a beacon or similar based navigation system and thereby reducing the need for installed infrastructure in the underground mining environment.

8.3 Future Work

While the complex vehicle model presented in this dissertation is controlled successfully by the open loop control strategy, and is able to predict tyre slip angles, the model is only a first step towards the development of an accurate full dynamic model of an LHD, including effects such as slip and tyre deformation. The first priority in future work is to perform the necessary tests, as outlined in chapter 6, to validate the vehicle model as well as obtain the tyre data for the LHD vehicle tyres. The accuracy of the model is highly dependant on these parameters. Additional dynamic effects which need to be added to the model in future work include taking into consideration suspension effects (roll motion) from not only the minimal suspension of the vehicle but also energy absorbtion within the tyre sidewalls. The model also needs to be modified to include the effects of operating on an inclined surface (pitch motion) and not only a flat surface as is the case with the current model.

Using the LHD dynamic model it will then be possible to develop control strategies including necessary safety considerations such as obstacle detection and collision avoidance. This will also necessitate more accurate sensor models and a realistic and efficient tunnel model for the purpose of software simulation.

References

[1] J. Roberts, E. Duff, and P. Corke, "Reactive navigation and opportunistic localization for autonomous underground mining vehicles," *The International Journal of Information Sciences*, vol. 145, pp. 127 –146, 2002.

[2] P. Corke, G. Winstanley, and J.Roberts, "Robotics for the mining industry: Opportunities and current research," in *International Conference on Field and Service Robotics*, Pittsburgh, PA, August 1999.

[3] J. Steele, G. Chidambar, and A. Kleve, "Control and scale model simulation of sensor-guided LHD mining machines," *IEEE Transactions on Industry Applications*, vol. 29, 1993.

[4] G. Baiden, "Autonomation of underground mining using teleremote systems," in *6th International Symposium on Mine Mechanization and Automation, South African Institute of Mining and Metallurgy*, 2001.

[5] R. Hurteau, M. St-Amant, Y. Laperriere, and G. Chevrette, "Optical guidance system for underground mine vehicles," in *Proceedings of the 1992 IEEE International Conference on Robotics and Automation*, Nice, France, May 1992.

[6] "Q-Navigator," *http : //www.mine − automation.com*, last visited: 17 March 2003.

[7] H. Makela, "Overview of LHD navigation without artificial beacons," *Robotics and Autonomous Systems*, vol. 36, pp. 21–35, 2001.

[8] R. Madhavan, M. Dissanayke, and H. Durrant-Whyte, "Autonomous underground navigation of an LHD using a combined ICP-EKF approach," in *Proceedings of the 1998 IEEE International Conference on Robotics & Automation*, Leuven, Belgium, May 1998.

[9] R. King and J. Lane, "Computer assisted guidance of an underground mine truck," in *Proceedings of the 1994 International Conference on Robotics and Automation*, San Diego,California, May 1994.

[10] S. Singh, "State of the art in automation in earth moving," *ASCE Journal of Aerospace Engineering, Vol 10. no.4*, July 1999.

[11] S. J. Julier and H. F. Durrant-Whyte, "On the role of process models in autonomous land vehicle navigation systems," *IEEE Transactions on Robotics and Automation*, February 2003.

[12] "Mining engineers toolbox - block caving," *http* : *//www.mininglife.com/Miner/ugmethods/block_caving_description.htm*, last visited: 4 October 2004.

[13] "Lkab- an international high-tech minerals group," *http* : *//www.lkab.com/frameset*$_2$*.html*, last visited: 4 October 2004.

[14] "Lkab," *http* : *//www.LKAB.com*, last visited: 21 December 2004.

[15] H.-H. Mohle, *Factors Affecting LHD Productivity on Premier Diamond Mine*, August 1995.

[16] P. Saayman, I. Craig, and F. Camisani-Calzolari, "Optimization of an autonomous vehicle dispatch system in an underground mine," in *The 1st African Control Conference (AFCON2003)*, Cape Town, South Africa, December 2003, pp. 151–156.

[17] C. Altafini, "Why to use an articulated vehicle in underground mining operations ?" in *Proceedings of the 1999 IEEE International Conference on Robotics and Automation*, Detroit, May 1999.

[18] O. Richter, *Synchronised LHD Production and Maintenance at Finsch Diamond Mine*, No date.

[19] "St-3.5 6 tonne capacity scooptram LHD technical specifications and performance data," Portland, Oregan, USA.

[20] "Mining technology - volvo articulated hauler with rock load," *http* : *//www.mining−technology.com/contractors/transportation/volvo_artic/volvo_artic*1*.html*, last visited: 5 October 2004.

[21] "Volvo articulated hauler - a25d technical specifications," *http* : *//www.volvoce.com*, last visited: 5 October 2004.

[22] H. Makela, "Outdoor navigation of mobile robots," Ph.D. dissertation, Department of Automation and Systems technology, Helsinki University, 2001.

[23] J. Borenstein, H. Everett, and L. Feng, "Where am I? sensors and methods for mobile robot positioning," *University of Michigan Technical Report*, April 1996.

[24] R. Brown, *Introduction to Random Signal Analysis and Kalman Filtering, Proceedings of the 1st International Colloquim on tyre Models for Vehicle Dynamics Analysis held in Delft, The Netherlands, October 21-22.* New York: John Wiley and Sons, 1983.

[25] J. Guivant and E. Nebot, "Compressed form real time implementation of simultaneous localization and mapping," *Australian Centre for Field Robotics*, No date.

[26] J. Guivant, F. Masson, and E. Nebot, "Simultaneous localization and mapping using natural features and absolute information," *Robotic Autonomous Systems*, vol. 40(2-3), pp. 79–90, 2002.

[27] S. Thrun, W. Burgard, and D. Fox, "Probabilistic approach to concurrent mapping and localization for mobile robots," *Autonomous Robotics*, vol. 5(3-4), pp. 79–90, 1998.

[28] S. Scheding, G. Dissanayake, E. Nebot, and H. Durrant-Whyte, "An experiment in autonomous navigation of an underground mine vehicle," *IEEE Transactions on robotics and Automation*, vol. 15 no.1, pp. 127 –146, 1999.

[29] E. Nebot, T. Bailey, and J. Guivant, "Navigation algorithms for autonomous machines in off-road applications," *Journal of Autonomous Robots*, 2000.

[30] S. Thrun, D. Fox, and W. Bugard, "Probabilistic mapping of an environment by a mobile robot," in *Proceedings of the 1998 IEEE International Conference on Robotics and Automation*, Belgium, May 1998, pp. 1546–1551.

[31] T. Chen, J. Morris, and E. Martin, "Particle filters for the estimation of a state space model," Centre for Process Analytics and Control Technology, School of Chemical Engineering and Advanced Materials, University of Newcastle, Newcastle, UK, Tech. Rep., 2004.

[32] P. Bolzern, R. D. Santis, A. Locatelli, and Masciocchi, "Path tracking of articulated vehicles with off-axle hitching," *IEEE Transactions on Control Systems Technology*, vol. 6 No.4, July 1998.

[33] J. Roberts and P. Corke, "Automation of underground truck haulage," in *Proceedings of the Fourth International Symposium on Mine Mechanisation and Automation*, Brisbane, July 1997.

[34] R. Madhavan, "Terrain aided localization of autonomous vehicles," Intelligent Systems Division, National Institute of Standard and Technology, Gaithersburg, MD 20899-8230, U.S.A, Tech. Rep.

[35] J. Roberts and P. Corke, "Obstacle detection for a mining vehicle using a 2d laser," *CSIRO Mining Publications*, 1999.

[36] G. Winstanely, J. Roberts, and P. Corke, "Issues in obstacle detection for autonomous mining and construction vehicles," in *16th IAARC/IFAC/IEEE International Symposium on Automation and Robotics in Construction*, September 1999.

[37] M. K. Petty, J. Billingsley, and T. Tran-Cong, "Vehicle dynamics terminology, SAE J670e," Society of Automotive Engineers, Inc., Warrendale, PA, Tech. Rep., July 1976.

[38] T. Gillespie, *Fundamentals of Vehicle Dynamics*. Warrendale, PA: Society of Automotive Engineers, Inc., 1992.

[39] G. Genta, *Motor Vehicle Dynamcis, Modeling and Simulation, Series on advances in Mathematics for Applied Sciences - Vol. 43*. London: World Scientific, 1997.

[40] A. Hemami and V. Polotski, "Problem formulation for path tracking automation of low speed articulated vehicles," in *Proceedings of the 1996 IEEE International conference on Control Applications*, Dearborn, MI, September 1996.

[41] V. Polotski and A. Hemami, "Control of articulated vehicle for mining applications: Modeling and laboratory experiments," in *Proceedings of the 1997 IEEE International Conference on Control Applications*, Hartford, Ct, October 1997.

[42] T. Zuvich, "Vehicle dynamics for racing games," *http* : *//www.gdconf.com/archives/*2000/*zuvich.doc*, last visited: 1 October 2004.

[43] C. Chen and M. Tomizuka, "Modelling and control of articulated vehicles," *California PATH research report*, vol. UCB-ITS-PRR-97-42, November 1997.

[44] P. Ramanata, "Optimal vehicle path generator using optimization methods," Master's thesis, Faculty of Engineering, Virginia Polytechnic and State University, 1998.

[45] Z. Baraket and P. Fancher, "Representation of truck tire properties in braking and handling studies: The influence of pavement and tire characteristics." University of Michigan Transport Research Institute., Tech. Rep. Technical Report UMTRI-89-33.

[46] H. Pacejka, *Tyre Models for Vehicle Dynamic Systems.* Amsterdam: Swets and Zeitlinger, 1991.

[47] P. Ridley and P. Corke, "Autonomous control of an underground mine vehicle," in *Proceedings 2001 Australian Conference on Robotics and Automation*, Sydney, November 2001.

[48] "Sandvik tamrock EJC 245 - technical specification," *http : //www.sandvik.com*, last visited: 5 October 2004.

[49] "Global security.org," *http : //www.globalsecurity.org/military/world/rsa/ratel.htm*, last visited: 21 December 2004.

[50] D. Wells, *Schaums's Outline of theory and problems of Lagrangian Dynamics.* New York: McGraw-Hill, 1967.

[51] "Gerotek test facilities Pty Ltd," www.gerotek.co.za, last visited: 2 June 2004.

[52] "Racelogic0 Pty Ltd," http://www.racelogic.co.uk/2003/vbox/vboxii.htm, last visited: 2 June 2004.

[53] D. Seborg, T. Edgar, and D. Mellicamp, *Process dynamics and control.* New York: John Wiley & Sons, 1989.

[54] J. Lotz, "Design of a load, haul and dump mining vehicle automatin controller," Final Year Project Report, University of Pretoria, Pretoria, South Africa, Tech. Rep., November 2004.

[55] M. Norgaard, "Kalmtool - state estimation for nonlinear systems," *Tech. Report. IMM-REP-2000-6, Department of Mathematical Modelling, Technical University of Denmark*, 2000.

[56] Y. Yavin and C. Frangos, "Computation of feasible control trajectores for the navigation of a ship around an obstacle in the presence of a sea current," *Journal of Mathematical and Computer Modelling*, vol. 21, no. 3, pp. 99–117, 1995.

[57] B. Dragt, F. Camisani-Calzolari, and I. Craig, "Modelling the dynamics of a load-haul-dump vehicle," in *Proceedings of the 16th IFAC World Congress*, Prague, Czech Republic, July 2005.

[58] B. Dragt, I. Craig, and F. Camisani-Calzolari, "An overview of the automation of load-haul-dump vehicles in an underground mine environment," in *Proceedings of the 16th IFAC World Congress*, Prague, Czech Republic, July 2005.

[59] B. Dragt, F. Camisani-Calzolari, and I. Craig, "Autonomous underground mine vehicles," in *The 1st African Control Conference (AFCON2003)*, Cape Town, South Africa, December 2003, pp. 369–374.

[60] B. Dragt, I. Craig, and F. Camisani-Calzolari, "Modelling of an autonomous underground mine vehicle," in *The 11th IFAC Symposium on Automation in Mining, Mineral and Metal Processing(MMM2004).Proceedings to appear.*, Nancy, France, September 2004.

[61] B. Dragt, F. Camisani-Calzolari, and I. Craig, "Simplified dynamic model of a load-haul-dump vehicle." in *Accepted for inclusion in the IFAC Worksop on Automation in Mining, Mineral and Metal Industry*, Cracow, Poland, 20 -22 September 2006.

List of Figures

1.1 LHD Tele-operator station at LKAB in Kiruna, Sweden. 2

2.1 Illustration of the block cave mining method. The vehicles in this case move on tracks. However the principle is the same for trackless vehicles.[Figure Courtesy of De Beers Consolidated Mines] 8
2.2 Layout of a typical trackless underground block cave mine, [Figure Courtesy of De Beers Consolidated Mines] 8
2.3 Overview of large scale sub-level caving mining method showing steps 1 to 6. Adapted from [14]. 9
2.4 Comparison of off-tracking error of car-like vehicle and articulated vehicle. 11
2.5 Side view of a typical LHD vehicle indicating the articulation joint. 12
2.6 Photograph of hydraulic actuator on LHD vehicle's articulation joint. . . . 13
2.7 Schematic diagram of LHD vehicle showing the vehicle at maximum steering angle. Adapted from the Atlas Copco ST-3.5 6 Tonne Capacity Scooptram LHD technical specifications and performance data [19] 13
2.8 Illustration of possible range of motion of front bucket of LHD vehicle and drivers seating position. Adapted from the Atlas Copco ST-3.5 6 Tonne Capacity Scooptram LHD technical specifications and performance data [19] 14
2.9 This picture shows an example of two articulated mining trucks. Note that these trucks are articulated vehicles. Adapted from [20] 14
2.10 Schematic diagram of articulated mining truck. Adapted from [21] 15

3.1 General structure of pose estimation using Kalman filter (adapted from [22]). 20

4.1 Vehicle axis system as defined by SAE [37]. 33
4.2 Diagrammatic representation of forces acting on a vehicle on an inclined plane.. 34
4.3 LHD vehicle in a typical mine tunnel, [Anon]. 35
4.4 Illustration of tyre slip angle α. 36

4.5 Normalised Lateral force versus slip angle for bias ply tyre. 37
4.6 Diagram showing sign convention used in defining slip angles. The diagram shows a positive lateral force F_y and therefore the slip angle α is negative. 38
4.7 Diagrammatic illustration of friction circle concept 39
4.8 Tyre Force Model (Adapted from [43]). 40
4.9 Flowchart of comprehensive tyre model (Adapted from [45]). 42
4.10 Schematic diagram illustrating the parameters of a two- and a three-degree-of-freedom bicycle model. 45

5.1 LHD kinematic geometry. 51
5.2 LHD kinematic geometry including slip angles. 52
5.3 Schematic diagram of a single track or bicycle model for a vehicle with articulated steering such as an LHD. 54
5.4 Illustration of parameters used to determine the location of the centre of gravity of the LHD. 55
5.5 Coordinate system used in model derivation. 57
5.6 Schematic Diagram of vehicle parameters used in model derivation. 59
5.7 Definition of tyre forces in Cartesian Coordinates. 64
5.8 Flowchart of simplified comprehensive tyre model. 68
5.9 Plot of side force versus slip angle α for Ratel tyre with 2 tonnes of vertical loading. 69
5.10 Plot of side force versus slip angle α for Ratel tyre with 4 tonnes of vertical loading. 69

7.1 Loop diagram of sensor based control system. 77
7.2 Plot of simulation results showing tunnel walls and the trajectory followed by the vehicle 77
7.3 Photograph of scale model of LHD vehicle with ultrasonic and infrared range sensors. 78
7.4 Plot of simulation results for EKF model 79
7.5 Plot of predicted slip angle α 79
7.6 Plot of predicted slip angle β 80
7.7 Plot of predicted wheel radius R 80
7.8 Plot of trajectory predicted by kinematic vehicle model (dashed line) and Unloaded single-track vehicle model (solid line) for a curvature of constant radius. 82

7.9 Plot of trajectory predicted by kinematic vehicle model (dashed line) and loaded single-track vehicle model (solid line) for a curvature of constant radius. . . . 83
7.10 Plot of $\dot{x}$ versus time. . . . 87
7.11 Plot of $\ddot{x}$ versus time. . . . 87
7.12 Plot of $\dot{x}$ versus time. . . . 89
7.13 Plot of $\ddot{x}$ versus time. . . . 89
7.14 Plot of $\dot{y}$ versus time. . . . 90
7.15 Plot of $\ddot{y}$ versus time. . . . 90
7.16 Plot of $\dot{\epsilon}$ versus time. . . . 91
7.17 Plot of $\ddot{\epsilon}$ versus time. . . . 91
7.18 Plot of $\dot{\epsilon_f}$ versus time. . . . 92
7.19 Plot of $\ddot{\epsilon_f}$ versus time. . . . 92
7.20 Plot of trajectory travelled by vehicle during simulation. . . . 93
7.21 Plot of the slip angle predicted by the vehicle model for the trajectory travelled by vehicle. Front tyre slip angle indicated by dotted line, rear tyre slip angle indicated by solid line. . . . 93
7.22 Plot of trajectory travelled by vehicle during simulation. . . . 94
7.23 Plot of $\dot{x}$ versus time. . . . 94
7.24 Plot of $\dot{y}$ versus time. . . . 95
7.25 Plot of $\ddot{x}$ versus time. . . . 95
7.26 Plot of $\ddot{y}$ versus time. . . . 96
7.27 Plot of $\dot{\epsilon}$ versus time. . . . 96
7.28 Plot of $\ddot{\epsilon}$ versus time. . . . 97
7.29 Plot of $\dot{\epsilon_f}$ versus time. . . . 97
7.30 Plot of $\ddot{\epsilon_f}$ versus time. . . . 98
7.31 Plot of the slip angle predicted by the vehicle model for the trajectory travelled by vehicle. Slip angle for a front tyre is indicated by the solid line and the slip angle for a rear tyre is indicated by a dotted line. . . . 98

List of Tables

4.1 Parameters of Segel tyre model. 41
4.2 Parameters of single-track dynamic vehicle models. 46

5.1 Parameters of single-track dynamic vehicle model for an articulated steering vehicle such as an LHD. 54
5.2 Unloaded LHD Vehicle Model Parameters. 56
5.3 Loaded LHD Vehicle Model Parameters. 56
5.4 Parameters of vehicle model. 60

6.1 Estimated Model Parameters. 75

7.1 LHD vehicle parameters used for simulations Parameters. 88